

AD-A173 888

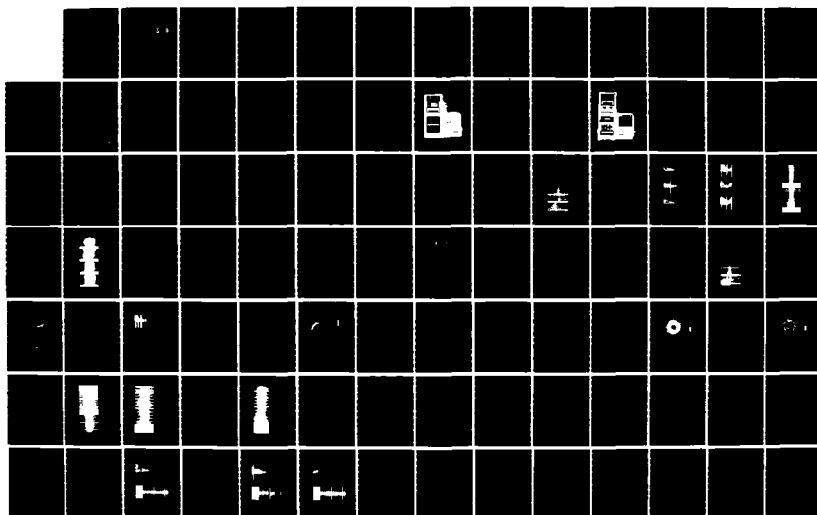
HF (HIGH-FREQUENCY) CHANNEL PROBE(U) SRI INTERNATIONAL
 MENLO PARK CA R P BASLER ET AL. 31 MAY 85
 DNA-TR-85-247 DNA001-83-C-0325

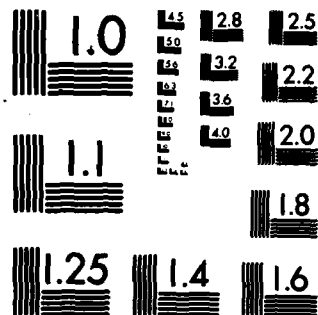
1/2

UNCLASSIFIED

F/G 20/14

NL





AD-A173 088

12

DNA-TR-85-247

HF CHANNEL PROBE

**Roy P. Basler
Philip B. Bentley
Gary H. Price
SRI International
333 Ravenswood Avenue
Menlo Park, CA 94025-3434**

**Charles L. Rino
Denise K. Rust**

31 May 1985

**DTIC
ELECTE
OCT 17 1986
S D**

Technical Report

CONTRACT No. DNA 001-83-C-0325

**Approved for public release;
distribution is unlimited.**

**THIS WORK WAS SPONSORED BY THE DEFENSE NUCLEAR AGENCY
UNDER RDT&E RMSS CODE B322084466 S99QMXBB00031 H2590D.**

**Prepared for
Director
DEFENSE NUCLEAR AGENCY
Washington, DC 20305-1000**

DTIC FILE COPY

DISTRIBUTION LIST UPDATE

This mailer is provided to enable DNA to maintain current distribution lists for reports. We would appreciate your providing the requested information.

- ☐ Add the individual listed to your distribution list.
- ☐ Delete the cited organization/individual
- ☐ Change of address.

NAME: _____

ORGANIZATION: _____

OLD ADDRESS

CURRENT ADDRESS

TELEPHONE NUMBER: () _____

SUBJECT AREA(s) OF INTEREST:

DNA OR OTHER GOVERNMENT CONTRACT NUMBER: _____

CERTIFICATION OF NEED-TO-KNOW BY GOVERNMENT SPONSOR (if other than DNA):

SPONSORING ORGANIZATION: _____

CONTRACTING OFFICER OR REPRESENTATIVE: _____

SIGNATURE: _____

Director
Defense Nuclear Agency
ATTN: STTI
Washington, DC 20305-1000

Director
Defense Nuclear Agency
ATTN: STTI
Washington, DC 20305-1000

UNCLASSIFIED

SECURITY CLASSIFICATION OF THIS PAGE

ADA173088

REPORT DOCUMENTATION PAGE

1a. REPORT SECURITY CLASSIFICATION UNCLASSIFIED			1b. RESTRICTIVE MARKINGS		
2a. SECURITY CLASSIFICATION AUTHORITY N/A since Unclassified			3. DISTRIBUTION/AVAILABILITY OF REPORT Approved for public release; distribution is unlimited.		
2b. DECLASSIFICATION/DOWNGRADING SCHEDULE N/A since Unclassified					
4. PERFORMING ORGANIZATION REPORT NUMBER(S) SRI International Project 6185			5. MONITORING ORGANIZATION REPORT NUMBER(S) DNA-TR-85-247		
6a. NAME OF PERFORMING ORGANIZATION SRI International		6b. OFFICE SYMBOL (if applicable)	7a. NAME OF MONITORING ORGANIZATION Director Defense Nuclear Agency		
6c. ADDRESS (City, State, and ZIP Code) 333 Ravenswood Avenue Menlo Park, CA 94025-3434			7b. ADDRESS (City, State, and ZIP Code) Washington, DC 20305-1000		
8a. NAME OF FUNDING/SPONSORING ORGANIZATION		8b. OFFICE SYMBOL (if applicable)	9. PROCUREMENT INSTRUMENT IDENTIFICATION NUMBER DNA 001-83-C-0325		
8c. ADDRESS (City, State, and ZIP Code)			10. SOURCE OF FUNDING NUMBERS		
			PROGRAM ELEMENT NO. 62715H	PROJECT NO. S99QMXB	TASK NO. B
			WORK UNIT ACCESSION NO. DH008363		
11. TITLE (Include Security Classification) HF CHANNEL PROBE					
12. PERSONAL AUTHOR(S) Basler, Roy P.; Bentley, Philip B.; Price, Gary H.; Rino, Charles L.; Rust, Denise K.					
13a. TYPE OF REPORT Technical Report		13b. TIME COVERED FROM 830701 TO 850531		14. DATE OF REPORT (Year, Month, Day) 850531	
				15. PAGE COUNT 128	
16. SUPPLEMENTARY NOTATION This work was sponsored by the Defense Nuclear Agency under RDT&E RMSS Code B322084466 S99QMXBB00031 H2590D.					
17. COSATI CODES			18. SUBJECT TERMS (Continue on reverse if necessary and identify by block number)		
FIELD	GROUP	SUB-GROUP	Ionosphere Polar Spread F		
17	2	.1	HF propagation Scattering Irregularities		
20	14		Striations Doppler Sounding		
19. ABSTRACT (Continue on reverse if necessary and identify by block number) An experiment in Greenland has measured the transfer characteristics for HF signals propagating through disturbed regions of the ionosphere. Transmissions over the 1-hop path from Narssarssuaq to Thule have suffered distortions in the range (propagation time) and Doppler domains on the order of hundreds of microseconds and tens of Hertz, respectively. A frequency-modulated continuous wave (FMCW) waveform was used for oblique sounding purposes, and a pseudorandom noise modulation with a 20-kHz bandwidth was used to measure range and Doppler spreads. Spaced receivers were used to measure azimuthal angle of arrival, and independent ionospheric diagnostic data for points along the path were provided by the incoherent-scatter radar at Sondre Stromfjord. The results were interpreted generally in terms of geophysical plasma dynamics, and also, in particular, in terms of scatter effects produced by high-velocity plasma irregularities encountered along the mean ray paths.					
20. DISTRIBUTION/AVAILABILITY OF ABSTRACT <input type="checkbox"/> UNCLASSIFIED/UNLIMITED <input checked="" type="checkbox"/> SAME AS RPT. <input type="checkbox"/> DTIC USERS			21. ABSTRACT SECURITY CLASSIFICATION UNCLASSIFIED		
22a. NAME OF RESPONSIBLE INDIVIDUAL Betty L. Fox			22b. TELEPHONE (Include Area Code) (202) 325-7042		22c. OFFICE SYMBOL DNA/STTI

DD FORM 1473, 84 MAR

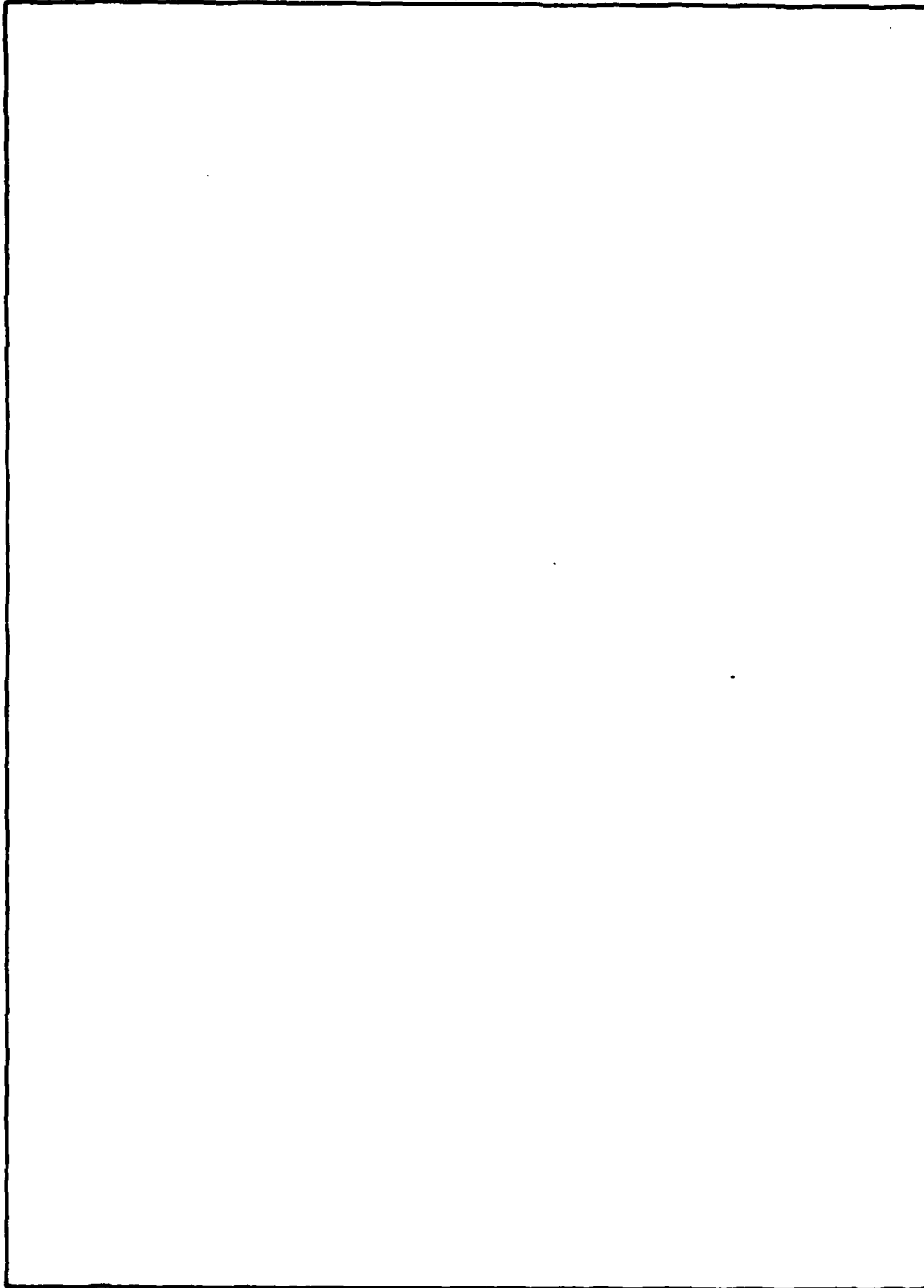
83 APR edition may be used until exhausted.
All other editions are obsolete.

SECURITY CLASSIFICATION OF THIS PAGE

UNCLASSIFIED

UNCLASSIFIED

SECURITY CLASSIFICATION OF THIS PAGE(When Data Entered)



UNCLASSIFIED

SECURITY CLASSIFICATION OF THIS PAGE(When Data Entered)

CONVERSION TABLE

Conversion factors for U.S. Customary to metric (SI) units of measurement

MULTIPLY → BY → TO GET
TO GET ← BY ← DIVIDE

angstrom	1.000 000 X E -10	meters (m)
atmosphere (normal)	1.013 25 X E +2	kilo pascal (kPa)
bar	1.000 000 X E +2	kilo pascal (kPa)
barn	1.000 000 X E -28	meter ² (m ²)
British thermal unit (thermochemical)	1.054 350 X E +3	joule (J)
calorie (thermochemical)	4.184 000	joule (J)
cal (thermochemical)/cm ²	4.184 000 X E -2	mega joule/m ² (MJ/m ²)
curie	3.700 000 X E +1	*giga becquerel (GBq)
degree (angle)	1.745 329 X E -2	radian (rad)
degree Fahrenheit	$t_F = (t_C + 459.67)/1.8$	degree kelvin (K)
electron volt	1.602 19 X E -19	joule (J)
erg	1.000 000 X E -7	joule (J)
erg/second	1.000 000 X E -7	watt (W)
foot	3.048 000 X E -1	meter (m)
foot-pound-force	1.355 818	joule (J)
gallon (U. S. liquid)	3.785 412 X E -3	meter ³ (m ³)
inch	2.540 000 X E -2	meter (m)
jerk	1.000 000 X E +9	joule (J)
joule/kilogram (J/kg) (radiation dose absorbed)	1.000 000	Gray (Gy)
kilotons	4.183	terajoules
kip (1000 lbf)	4.448 222 X E +3	newton (N)
kip/inch ² (ksi)	6.894 757 X E +3	kilo pascal (kPa)
ktop	1.000 000 X E +2	newton-second/m ² (N-s/m ²)
micon	1.000 000 X E -6	meter (m)
mil	2.540 000 X E -5	meter (m)
mile (international)	1.609 344 X E +3	meter (m)
ounce	2.834 952 X E -2	kilogram (kg)
pound-force (lbf avoirdupois)	4.448 222	newton (N)
pound-force inch	1.129 848 X E -1	newton-meter (N-m)
pound-force/inch	1.751 268 X E +2	newton/meter (N/m)
pound-force/foot ²	4.788 026 X E -2	kilo pascal (kPa)
pound-force/inch ² (psi)	6.894 757	kilo pascal (kPa)
pound-mass (lbm avoirdupois)	4.535 924 X E -1	kilogram (kg)
pound-mass-foot ² (moment of inertia)	4.214 011 X E -2	kilogram-meter ² (kg-m ²)
pound-mass/foot ³	1.601 846 X E +1	kilogram/meter ³ (kg/m ³)
rad (radiation dose absorbed)	1.000 000 X E -2	**Gray (Gy)
roentgen	2.579 760 X E -4	coulomb/kilogram (C/kg)
shake	1.000 000 X E -8	second (s)
slug	1.459 390 X E +1	kilogram (kg)
torr (mm Hg, 0° C)	1.333 22 X E -1	kilo pascal (kPa)

*The becquerel (Bq) is the SI unit of radioactivity; 1 Bq = 1 event/s.

**The Gray (Gy) is the SI unit of absorbed radiation.



For	
&l	<input checked="" type="checkbox"/>
ed	<input type="checkbox"/>

Distribution/	
Availability Codes	
Dist	Avail and/or Special
A-1	

TABLE OF CONTENTS

<u>Section</u>	<u>Page</u>
CONVERSION TABLE	iii
LIST OF ILLUSTRATIONS	3
LIST OF TABLES	7
1 INTRODUCTION	9
2 EQUIPMENT DESCRIPTION	12
2.1 Transmitter System	12
2.2 Receiver System	14
2.3 Operations	17
2.3 Displays	21
3 POLAR EXPERIMENT	25
4 DATA DESCRIPTION	30
4.1 Ionogram Data	30
4.2 CW Data	32
4.3 Range-Resolved Doppler Data	36
4.4 Phase Data	41
5 IONOSPHERIC STRUCTURE AND PROPAGATION ANALYSIS	46
5.1 Virtual Geometry	46
5.2 True-Height Profile	47
5.3 Quasi-Parabolic Layer Model	49
5.4 Ionogram Synthesis	51
6 INTERPRETATION IN TERMS OF GEOPHYSICAL PLASMA DYNAMICS	54
6.1 Background	54
6.2 Ionospheric Structure Models	59
6.3 HILAT Results	60

TABLE OF CONTENTS (Concluded)

<u>Section</u>		<u>Page</u>
	6.4 Effects of Moving Blobs	64
	6.5 Acoustic Gravity Waves	67
	6.6 Time and Height Variations of Doppler Data . . .	70
	6.7 Substorms	78
7	INTERPRETATION IN TERMS OF SCATTER EFFECTS	86
	7.1 Theory	86
	7.2 Comparison of Theory and Data	93
	7.3 Sensitivity to Parameter Variations	107
8	CONCLUSIONS	112
9	LIST OF REFERENCES	113

LIST OF ILLUSTRATIONS

<u>Figure</u>	<u>Page</u>
1 Concept for Experimental Definition of the Transfer Characteristics of the HF Propagation Channel for Disturbed Ionospheric Conditions	11
2 Block Diagram of the HF Channel Probe Transmitter System	13
3 Photograph of the HF Channel Probe Transmitter System	15
4 Block Diagram of the HF Channel Probe Receiver System	16
5 Photograph of the HF Channel Probe Receiver System	18
6 HF Channel Probe 15-min Data-Collection Sequence	19
7 An Example of the Online Display for the 13.056-s PRN Dwell	23
8 An Example of the Online Display for the 3.264-s PRN Dwell	24
9 Site Locations for the Polar-Cap Experiment	27
10 The Path from Narssarssuaq to Thule at 0000 GMT in a Coordinate System of Invariant Magnetic Latitude and Corrected Magnetic Local Time	28
11 An Example of an Oblique Ionogram Showing E-Layer and F-Layer and One-Hop and Two-Hop Propagation for Relatively Undisturbed Conditions on 17 October 1984 at 1716 GMT	31
12 A Sequence of Ionograms Recorded at 15-min Intervals Showing Quiet and Moderately Disturbed Conditions on 3 October 1984	33
13 A Continuation of the Ionogram Sequence in Figure 12 Showing More Severely Disturbed Conditions	34
14 An Example of CW Data Recorded at 10.120 MHz over a 30-min Period Starting at 1900 GMT on 8 October 1984	35
15 An Example of CW Data at 10.610 MHz Under Relatively Disturbed Conditions for One Hour Starting at 1515 GMT on 3 October 1984	37
16 The Appearance of the Spectrum in Range Cell 8 of the PRN Dwell Data Shown in Figure 7	38

LIST OF ILLUSTRATIONS (Continued)

<u>Figure</u>		<u>Page</u>
17	A Perspective Display of SNR Versus Range and Doppler Frequency for the PRN Dwell Data Shown in Figure 7	39
18	An Example of the Doppler Spectrum Recorded in California for Benign Ionospheric Conditions	40
19	Phase Difference Between the Same Spectral Components on the Two Receiver Channels for the Same Data Set for Which the Power Spectrum was Shown in Figure 16	43
20	The Phase of the Cross Spectrum (the Phase Counterpart of the Power-Spectrum Data Shown in Figure 17)	44
21	Phase Difference for Benign Ionospheric Conditions for the Same Data Set for Which the Power Spectrum was Shown in Figure 18	45
22	Narssarssuaq-to-Thule Oblique Ionogram Recorded on 8 October 1984 at 1901 GMT	48
23	Vertical Ionograms Recorded on 8 October 1984 at 1859 GMT	50
24	Comparison of a Synthesized Ionogram with the Experimental Ionogram Shown in Figure 22	52
25	Electron Density (el/cm^3) at a Height of 250 km as a Function of Invariant Magnetic Latitude and Corrected Magnetic Local Time as Observed by the Incoherent-Scatter Radar at Sondre Stromfjord Over a 24-Hour Period on 18 May 1985	55
26	Plasma Velocities Corresponding to the Electron-Density Data Given in Figure 25	56
27	Irregularity Strength Parameter T in Decibels Averaged Over More than a Year at Sondre Stromfjord	61
28	Distribution Functions of the Spectral Index Values Corresponding to Data Shown in Figure 27	62
29	Clock-Dial Plot of C_s Corrected for a 10:1 Anisotropy and a 100-km Layer Thickness	63
30	Signatures of Moving Blobs as They Appear in CW Data Recorded at 10.120 MHz on 8 October 1984 Starting at 1930 GMT	65
31	Signature of a Moving Blob with a Negative Doppler Frequency as it Appears in CW Data Recorded at 10.240 MHz on 11 October 1984 Starting at 1900 GMT	66

LIST OF ILLUSTRATIONS (Continued)

<u>Figure</u>		<u>Page</u>
32	An Example of a CW Record for 8.990 MHz Starting at 2015 GMT on 10 October 1984 Showing Quasi-Periodic Variations that are Interpreted as an Effect of Acoustic-Gravity Waves in the Ionosphere	68
33	Variations of Spectral Width (20 dB Down From Peak) and Spectral Spread (Second Moment) with GMT on 3 October 1984 for F-Layer Low-Ray Propagation (7.1-ms Delay Time)	72
34	Doppler Frequency of Peak SNR and Centroid (First Moment) Versus GMT on 3 October 1984 at 7.1-ms Delay Time	74
35	Mean and Standard Deviation of Spectral Width (20 dB Down From Peak) and Spectral Spread (Second Moment) Versus GMT	75
36	Average Shape of the Spectrum in the 7.1-ms Range Cell as Defined by the Mean and Standard Deviation of the Spectral Widths for all Data	76
37	The Dependence of Spectral Width on Delay Time	77
38	Ionogram and CW Data Recorded at 10.765 MHz in a 15-min Sequence Starting at 2145 GMT on 26 March 1985	80
39	PRN Dwell Recorded at 10.765 MHz on 26 March 1985	81
40	Ionogram and CW Data Recorded at 10.765 MHz in a 15-min Sequence Starting at 2200 GMT on 26 March 1985	82
41	Ionogram and CW Data Recorded at 8.960 MHz in a 15-min Sequence Starting at 2215 GMT on 26 March 1985	83
42	Narssarssuaq Magnetogram for 26 March 1985	85
43	360° Velocity Measurements in Six Range Cells Made by the Incoherent-Scatter Radar at Sondre Stromfjord on 8 October 1984 from 1901:29 to 1911:29 GMT.	95
44	PRN Dwell Data Recorded in the two HF Channel Probe Receivers at 1903 GMT on 8 October 1984 at a Frequency of 10.120 MHz	97
45	Contour Plot of the Receiver 1 Data from Figure 44	102
46	SNR Versus Delay Time at a Doppler Frequency of 2 Hz for the Data Shown in Figure 45	103

LIST OF ILLUSTRATIONS (Concluded)

<u>Figure</u>		<u>Page</u>
47	Comparison of Theoretical and Experimental SDF for Two Range Cells from the PRN Dwell Data Shown in Figure 44 for Receiver 1	106
48	Frequency Variation of Spectral Width (10 dB Down from the Peak)	109
49	Variation of Ray Apex Height with Frequency	111

LIST OF TABLES

<u>Table</u>	<u>Page</u>
1 Scatter-Environment Parameters	94
2 Spatial Correlation Characteristics	99

SECTION 1

INTRODUCTION

Both naturally occurring and nuclear-induced propagation disturbances are important considerations for military high-frequency (HF) radio systems. Techniques for modeling the gross HF path structure and absorption have been available for many years; however, a more detailed HF channel characterization is needed to optimize the design and to predict the performance of sophisticated systems being proposed for a variety of missions. In particular, a channel characterization is needed to take full account of the deleterious effects of plasma density striations on HF signals propagating in the ionosphere.

For transionospheric satellite links, a comparatively simple but accurate SATCOM model [Wittwer, 1980]^{*} exists for predicting the correlation time and coherence bandwidth in disturbed nuclear environments. Similar models exist for predicting naturally occurring propagation disturbances [Secan and Fremouw, 1983]. Such information is crucial for designing mitigation techniques or for predicting the usability of existing satellite communication links. Unfortunately, no similar capability exists at HF, but the work described in this report represents a substantial first step in the development of an appropriate HF channel model.

* References are listed at the end of this report.

PREVIOUS PAGE
IS BLANK

The results of a number of carefully planned experiments (Wideband, STRESS, PLACES) to measure the propagation effects of both naturally occurring and artificially produced striations significantly affected the development of the SATCOM model. In the case of SATCOM, both the propagation theory and the essential characteristics of the striations are known. However, although the same structure will affect HF propagation, the extension of the propagation theory to such low frequencies has only recently been developed and had not been tested before the experiment reported here.

Because nuclear disturbances cannot be tested directly, the program described in this report was undertaken to measure the effects of natural ionospheric disturbances on HF propagation. By making these measurements in conjunction with other independent experiments that provide the necessary ionospheric diagnostic data (irregularity strengths and drift velocities), all important features of HF propagation in structured environments can be tested. Extrapolation to the conditions expected in the nuclear environment can then be done with more confidence than would otherwise be justified.

Figure 1 illustrates the basic experimental concept. An HF transmitting and receiving system, referred to here as the HF Channel Probe, has been built to measure the transfer characteristics of the HF propagation channel. These transfer characteristics are the distortions in the range (propagation delay time) and Doppler domains induced by structured plasma along the ray path in the ionosphere. The transmitter and receiver systems are placed at appropriate sites so that a one-hop propagation path traverses a region in which natural ionospheric disturbances are known to occur. As an historical reference, it is noted that a somewhat similar experiment was carried out at SRI more than twenty years ago by Shepherd and Lomax (1967). A survey of previous work on polar- and auroral-region effects on HF propagation has been presented by Hunsucker and Bates, (1969).

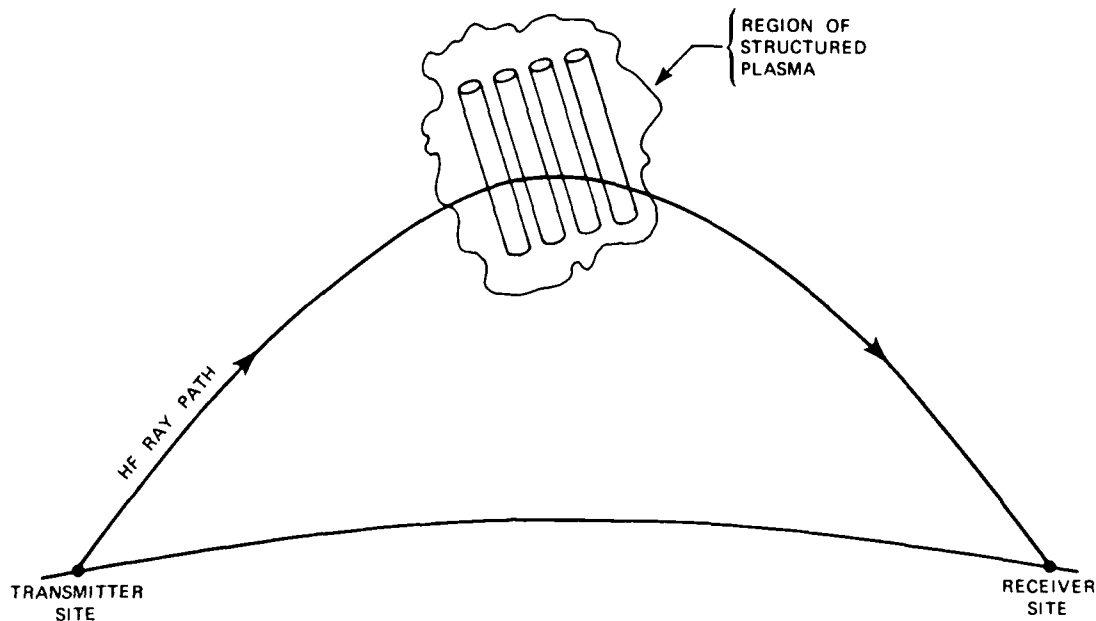


Figure 1. Concept for experimental definition of the transfer characteristics of the HF propagation channel for disturbed ionospheric conditions.

Although this report is the Final Report for Contract DNA001-83-C-0325 with the Defense Nuclear Agency, it should be considered only a preliminary report on an ongoing program. A substantial part of the effort on this contract was devoted to the design and fabrication of the HF Channel Probe beginning in July of 1983. It was then deployed for an experimental campaign in October 1984, and another campaign was conducted in March and April 1985. At the time of this writing, the data collected during these campaigns have been only partially analyzed. Additional analysis of the experiment data described here, as well as the collection of new data on three different propagation paths, will be supported under a new contract during the coming two years.

SECTION 2

EQUIPMENT DESCRIPTION

The HF Channel Probe consists of equipment at a transmitting site and at a receiving site at the two ends of an over-the-horizon propagation path. It uses a frequency-modulated continuous-wave (FMCW) signal for sounding purposes and pseudo-random noise (PRN) biphase modulation for the range-resolved coherent dwells that allow measurement of delay and Doppler spreads. It uses Transit satellite receivers at each site to give an absolute timing accuracy of about 10 μ s. All systems are computer controlled (with only limited keyboard input required from the operators), and online data displays permit selection of operating parameters on the basis of the results obtained in the field. Telephones are used for voice communication between the sites to adjust the operating parameters.

2.1 Transmitter System

The configuration of components that make up the transmitter system is shown in Figure 2. For the experiments conducted to date, a horizontally polarized log-periodic antenna (TCI Model 532) with a 60-ft tower was used as the HF antenna. Although the nominal lower frequency limit of this antenna is 6 MHz, it was not used below 6.5 MHz for these experiments because of the high VSWR (voltage standing wave ratio) that was encountered at lower frequencies. The final amplifier is a broadband solid-state device with an average output power rating of 1 kW, although for these experiments it was typically run at only 300 to 400 W.

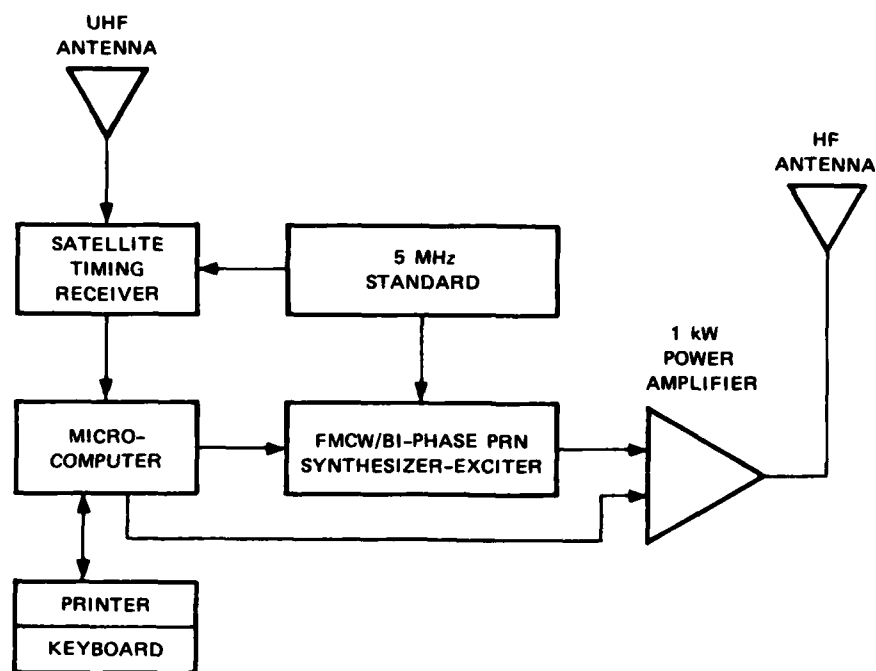


Figure 2. Block diagram of the HF channel probe transmitter system.

A special purpose microcomputer controls the operation of the system and the generation of the various waveforms required. For the PRN dwell, the CW transmission is biphase modulated with a maximal-length binary sequence. The code chip rate is 20 kHz with a code length of 255 (or 12.75 ms) corresponding to a code repetition rate of 78.43 Hz. This modulation provides an effective range resolution of 50 μ s (15 km) and an unambiguous Doppler window of about ± 40 Hz (actually 39.22 Hz). The biphase modulator is operated at 455 kHz (a convenient low frequency), filtered to remove extraneous sideband and harmonic energy, and then translated to the ultimate radio frequency for radiation.

The signal up-conversion hardware includes a high-stability frequency reference source driving a digitally controlled frequency

synthesizer. The 455-kHz biphase modulated signal is upconverted to 40.455 MHz, filtered again, and amplified before down-conversion through a mixer driven by a programmable synthesizer. The desired output then is at a frequency that can be specified anywhere in the HF band. The output is then amplified to 50 W in a driver amplifier and applied to the 1-kW final amplifier. If necessary, the final amplifier can be bypassed, and the 50-W driver amplifier can be connected directly to the antenna.

When the FMCW waveform is transmitted (for sounding purposes), the biphase modulation input is disabled, and the phase-continuous, programmable synthesizer (Wavetech Model 5130A) is driven by the system controller at the selected sweep rate (usually 250 kHz/s).

As shown in Figure 3, the transmitter system is installed in standard 19-in. racks that are shock-mounted inside special cases with front and back covers that are used during shipping but removed during operation. These cases are especially convenient for field experiments.

2.2 Receiver System

The block diagram of the receiver system is shown in Figure 4. Two separate receiver channels are used, each connected to a magnetic dipole (loop) antenna (TCI Model 612). The heart of the system is a special purpose microcomputer that controls the two receivers (Racal Model RA6790/GM), the high-speed processor, the tape recorder, and the displays.

The signal is taken from the receiver at the 455-kHz IF output, applied to a special-purpose in-phase and quadrature (I & Q) down convertor with baseband filters and amplifiers. The final output from each receiver is then in the form of a pair of folded-spectrum baseband audio signals that are presented to the processor analog-to-digital convertors (ADC).



Figure 3. Photograph of the HF channel probe transmitter system.

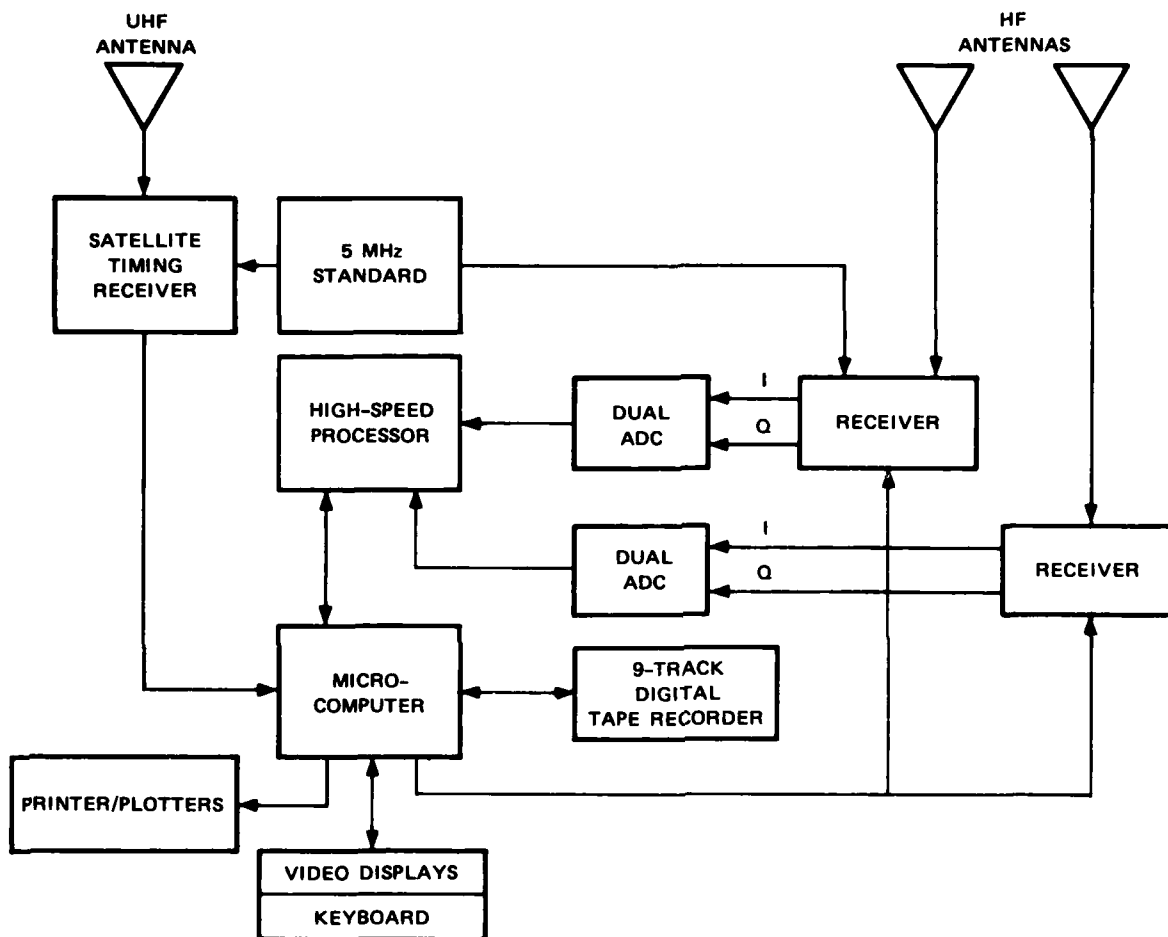


Figure 4. Block diagram of the HF channel probe receiver system.

The high-speed processor performs both the correlation and fast Fourier transform (FFT) spectral analysis for the PRN dwells and also the FFT analysis for the ionograms. For the PRN dwells, the system controller switches the receiver bandwidth to 20 kHz and the synthesizer to the receiver's internal tuning synthesizer. For the ionograms, the controller switches the receiver to the external chirp synthesizer, changes the bandwidth from 20 kHz to 1 kHz and sets the beat frequency oscillator (BFO) to an offset of 0.65 kHz. The signal then appears at

the baseband output to the processor ADC as an offset audio signal ranging from 0.15 kHz to 1.15 kHz. For the sample rate of 2.5 kHz, a 256-point transform is computed every 102.4 ms, which corresponds to a frequency increment of about 25 kHz when the sweep rate is 250 kHz/s. The corresponding range resolution is about 40 μ s, slightly better than the 50- μ s resolution for the PRN dwell data.

As shown in Figure 5, the receiver system is installed in standard 19-in. racks that are shock-mounted inside special cases in the same manner as the transmitter system. One case contains the Transit satellite time receiver, the plotter, and the video display terminals. Another contains the keyboard, the two receivers, and the synthesizer, and the third contains the processor, controller, and tape recorder.

2.3 Operations

The HF Channel Probe can be operated in a number of different modes, including continuous soundings, continuous PRN dwells, and continuous CW dwells, but the mode used for most of the data collection described in this report combines the recording of all of these different types of data in a standard 15-min sequence of activities. This sequence is shown in Figure 6.

All of the first minute and most of the third minute of the sequence are devoted to parameter changes. For the ionogram, the parameters to be specified are: the sweep rate (typically 250 kHz/s); the sweep width (typically 15 MHz); and delay time (typically 7.0 ms for the polar path) at which the 5-ms range gate is to be centered for recording and display of the ionogram data. For the CW and PRN dwells, the parameters to be specified are the frequency and the delay time (applicable to the PRN dwell only) for the start of the 1-ms range gate in which data are processed, recorded, and displayed. Furthermore, when the system is first turned on at the beginning of an experiment, it is necessary to set the day, hour, minute, and second on the internal clock. The internal clock is driven by pulses at a rate of one pulse



Figure 5. Photograph of the HF channel probe receiver system.

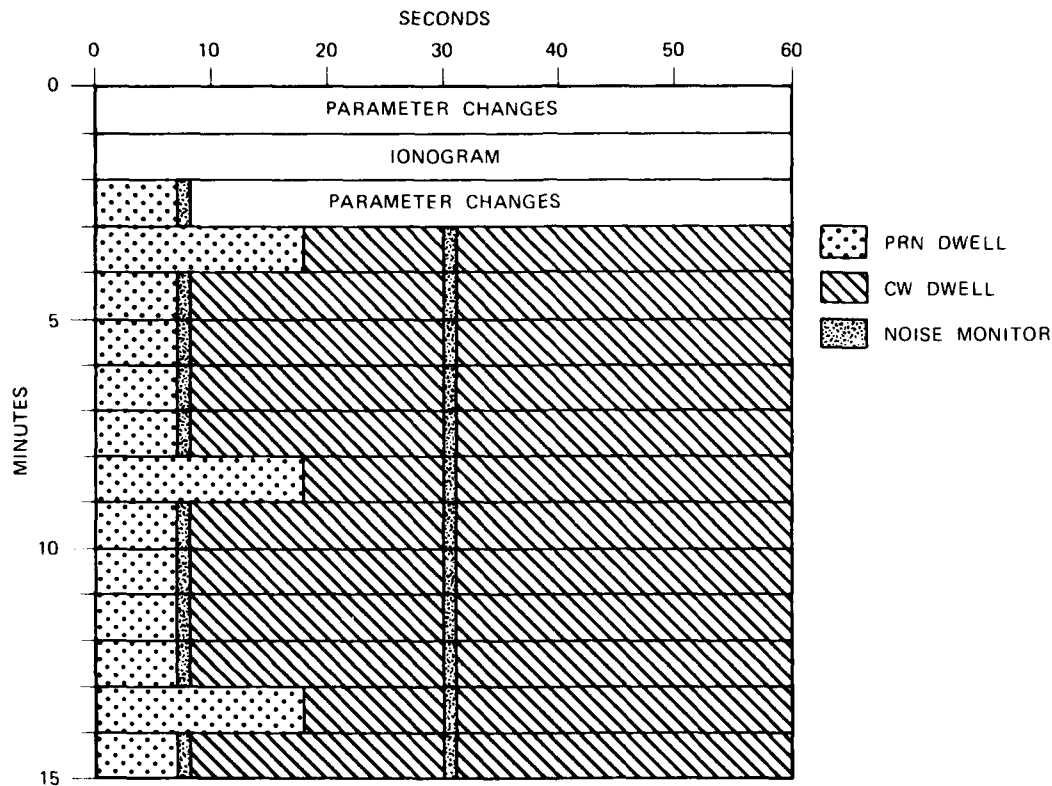


Figure 6. HF channel probe 15-min data-collection sequence.

per second (PPS) from the Transit satellite receiver time system. This 1-PPS time base is accurate to $\pm 10 \mu\text{s}$ relative to coordinated universal time (UTC).

During these parameter change periods, it is also possible to search for clear frequency channels by moving a cursor and obtaining an instantaneous readout of the noise and interference level on a particular channel. At times outside of these parameter change periods, it is possible to move the cursor to a new frequency, but the noise (interference) level readout is not given until the 1-s noise monitoring period that occurs once or twice per minute as shown in Figure 6. In practice, parameters can be set tentatively during the first minute,

then after an ionogram and PRN dwell, the parameter values can be adjusted slightly during the third minute if desired to optimize the appearance of the data. For a given experiment, parameters are generally set at the beginning of the operation, and the only changes required during the course of the experiment are the frequency and range-gate position for the CW and PRN dwells.

It can be seen in Figure 6 that there are three long PRN dwells and ten short dwells during each 15-min sequence. The coherent integration time for the long dwell is 13.056 s, and for the short dwell it is 3.26 s, although 18 s and 7 s, respectively, are allowed in the sequence to allow time for online FFT processing and display. These PRN dwells are the primary data recorded during the experiment, because they define the range spread and Doppler spread that result from propagation through the structured plasma along the ray path in the ionosphere. The balance of the time during the 15-min sequence, representing 84 percent of the total time, is devoted to CW dwells.

Thus, the HF Channel Probe system is programmed to collect four different types of data during each 15-min interval. First, an oblique ionogram is recorded and displayed to guide the selection of the frequency for the subsequent fixed-frequency dwells, and for later ray-tracing analysis of the propagation profile. Second, fixed-frequency coherent PRN dwells of either approximately 13-s or 3-s duration are recorded at a rate of one per minute to define the Doppler spread on range-resolved signals. Third, the spectrum of a CW signal transmitted between PRN dwells is recorded and displayed in an intensity-modulated, spectrum-versus-time format as an indication of the general level of disturbance and the presence of moving irregularities along the propagation path. Fourth, azimuthal angle-of-arrival measurements are made continuously during the PRN and CW dwells for the signal component received in each Doppler cell. (Actually, angle of arrival has to be determined by comparing phases of the signal in a given range and Doppler cell on the two receiver channels.)

The features of the HF Channel Probe that are described here are those that have been programmed into the system for its present applications. If desired, the system could be reprogrammed to add different features for other experimental purposes.

A total of 327,831 24-bit words are recorded on tape for a single 15-min sequence. The ionogram accounts for 36,927 words, the PRN dwells 108,408 words, the CW dwells 104,544 words, and a trailer record 1,952 words. A 1,200-ft reel of tape can record about five hours of data in the 15-min sequence mode.

During the operation of the system, the parameters are selected at the receiver site and passed to the transmitter site by telephone. After the initial setup, routine operations generally require only the new frequency and the start time for the new frequency to be communicated to the transmitter site.

2.4 Displays

Two video display terminals are incorporated into the receiver system to provide online displays of all data for the system operator. Hard copies of some of these displays are made in the field to keep a log of the operations for convenient reference, but for purposes of actual data analysis, new displays in a variety of different formats are generated offline from the data recorded on magnetic tape.

The online ionogram display is essential for showing the operator the mode structure and the frequencies that propagate at a given time. This display permits the selection of an operating frequency that propagates in the manner desired for a particular measurement, perhaps near the maximum-usable frequency (MUF), or well below the MUF where the F-layer high-ray and low-ray signals are well separated in delay time, or perhaps at a frequency for which both E-layer and F-layer signals are present. The digital readout of the noise/interference monitor is also included in the ionogram display to facilitate the selection of a

frequency channel that is quiet as well as in a region of the spectrum with the desired mode structure. Finally, the online ionogram display is essential for placing the 1-ms range gate at the proper delay time to record the signals of interest during the PRN dwells. The ionogram display can be called from memory at any time during the 15-min sequence until it is overwritten by the new ionogram during the next sequence.

The CW display shows the intensity-modulated power spectrum versus time in both receiver channels (separately) over a Doppler extent of ± 50 Hz. The CW display of Doppler spread and shift as a function of time is a good indicator of the general level of disturbance in the ionosphere. Also, as will be illustrated in Sections 4 and 6 of this report, the CW displays are well suited to showing the effects of acoustic gravity waves in the ionosphere and the effects of large blobs of enhanced plasma moving across the propagation path in response to electric fields in the ionosphere.

An example of the online display for the long PRN dwell is shown in Figure 7. The numbers at the bottom of the display show that the data were recorded on Day 277 (3 October 1984) at 1908:03 GMT at a frequency of 10.750 MHz, and that the delay time of the first range gate is 7.0 ms. (Delay times need to be corrected by subtracting 200 μ s from the recorded value to account for internal delays in the transmitter and receiving systems.) The display shows Doppler frequency from -40 Hz on the left to +40 Hz on the right (with 0 Hz in the center) in each of twenty, 50- μ s range cells that make up the 1-ms range gate in which data are processed. The power spectrum in each range gate is plotted on a scale that is 60 dB over the distance between the threshold levels for adjacent range cells. This particular example shows a maximum Doppler spread of ± 20 Hz or more in Range Cell 9, corresponding to a delay time of 7.4 ms (uncorrected, or 7.2 ms corrected).

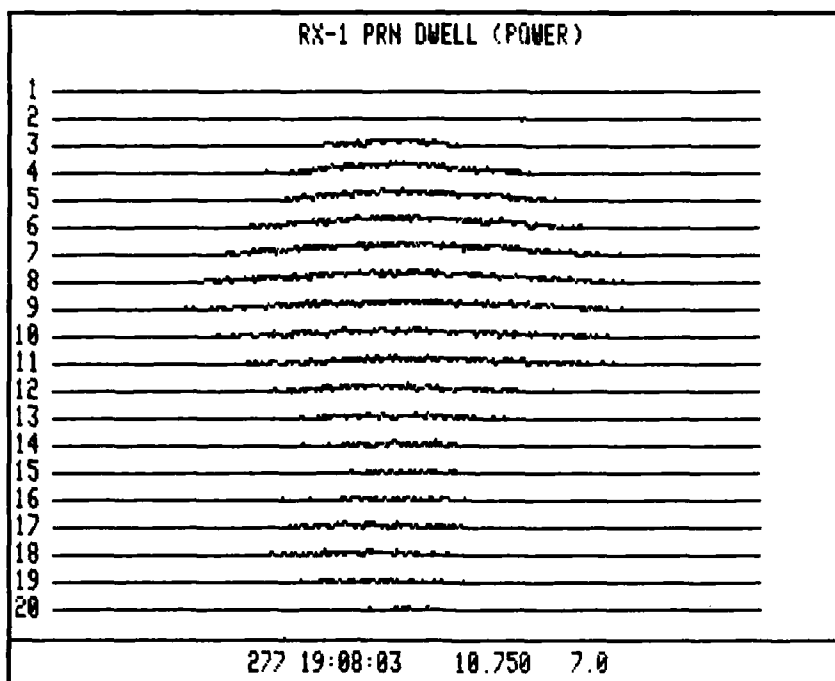


Figure 7. An example of the online display for the 13.056-s PRN dwell.

An example of the online display for the short dwell is shown in Figure 8. The format is the same as for the long dwell, except that in this case data are shown for both receivers. It is useful to have an online display for both receivers to verify the integrity of the entire system and thus to reveal problems such as loose cable connectors or other faulty system components. Also, the tape recorder can be used in the playback mode to verify the quality of the tape-recorded data while the experiment is still in progress in the field (although simultaneous playback and record is not possible).

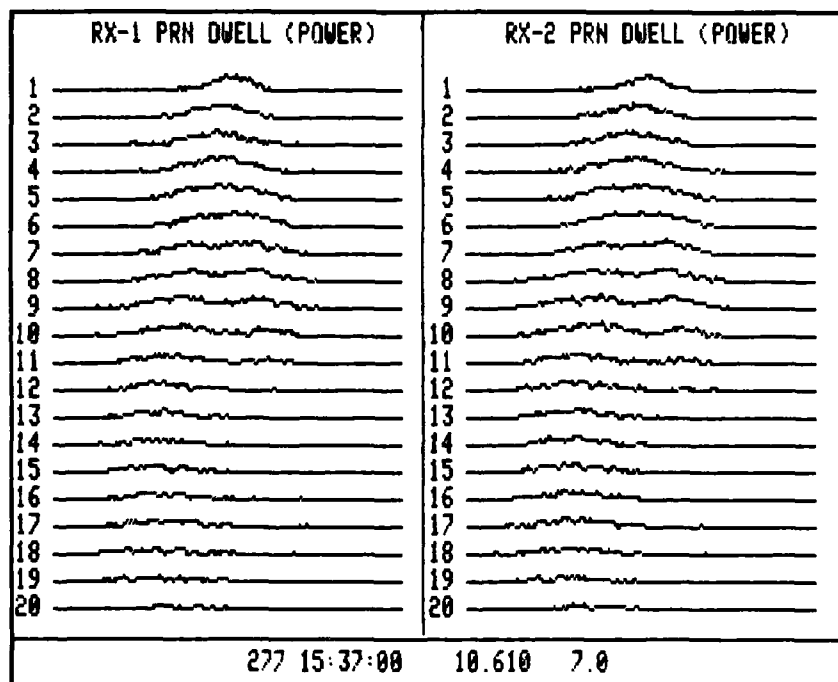


Figure 8. An example of the online display for the 3.264-s PRN dwell.

SECTION 3

POLAR EXPERIMENT

Natural ionospheric disturbances only occur in three regions of the world with an intensity and dependability sufficient for the purposes of the HF Channel Probe measurements. These are the polar, auroral, and equatorial regions. The initial experimental campaigns described in this report were conducted in the polar region, but auroral and equatorial campaigns are planned as part of the continuing program.

The high-latitude ionosphere, from the plasma pause through the polar cap, is a highly structured plasma containing irregularities (plasma-density fluctuations) with scale sizes ranging from meters to many tens of kilometers. The manifestations of these irregularities have been known for decades. They include blurring of ionogram records (spread F), strong radar backscatter echoes at normal incidence to the magnetic field, fading of transionospheric radio waves (scintillation), and the stochastic variation of virtually all measured ionospheric plasma parameters.

By making observations using multiple techniques, particularly using incoherent-scatter radar and scintillation measurements, an understanding has been established of the conditions that lead to the formation of intermediate-scale irregularities that are principally responsible for radio-wave scintillation. Thus, the high-latitude ionosphere can be used effectively as a plasma laboratory for studying the generation, dynamic evolution, and decay of these irregularities.

HF radio waves are refracted by the ionosphere and, in the presence of the irregularities, can develop delay and Doppler spreading about the normal propagation modes. To measure these signal distortions, a one-hop propagation path was established in Greenland with the transmitter

in Narssarssuaq and the receiver system 1918 km to the north in Thule as shown in Figure 9. The midpoint of this path is very near Godhavn (within about 24 km), where the Danish Meteorological Institute (DMI) operates a vertical incident (VI) sounder. The path also passes directly overhead at Sondre Stromfjord, where SRI operates an incoherent-scatter radar facility and a HILAT satellite ground station, and DMI operates a VI sounder. As we discuss in later sections of this report, these other ongoing experiments at Sondre Stromfjord and Godhavn provide valuable diagnostic data on ionospheric conditions along the HF propagation path.

The path from Narssarssuaq to Thule as it appears in a coordinate system of invariant magnetic latitude and corrected magnetic local time (CMLT) for the midpoint of the path is shown in Figure 10. The invariant latitude of the midpoint is 75.5° at a height of 300 km, and the measurements made in the experiment represent ionospheric effects that are produced near this location. The path appears curved in this figure because for a given Greenwich Meridian Time (GMT), the CMLT varies along the path. However, the transformation from GMT to CMLT as shown by the tic marks inside and outside the 60° invariant latitude circle is defined for the path midpoint. It is conventional in this type of display for noon (1200 CMLT) to be at the top of the circle to represent the sunward direction. The general features of the plasma convection pattern discussed in Section 6 remain fixed in this coordinate system, so, during the course of the experiment for a given day, the path shown in Figure 10 rotates counterclockwise, and measurements are made in different parts of the plasma convection system.

The HF Channel Probe experiment in the polar cap was conducted under the auspices of The Danish Commission for Scientific Research in

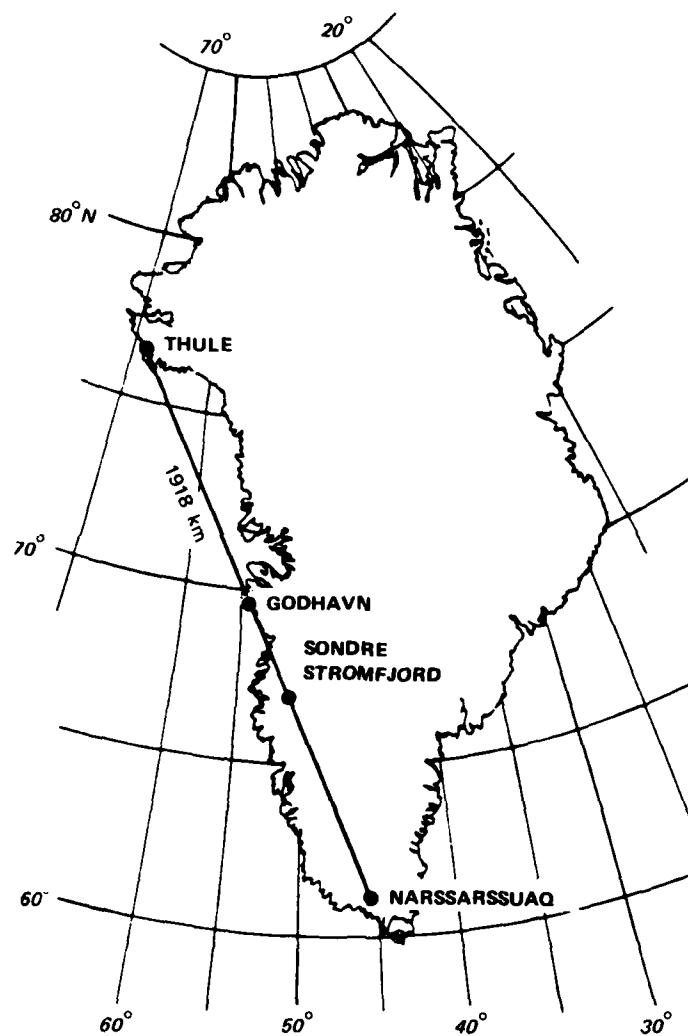


Figure 9. Site locations for the polar-cap experiment.

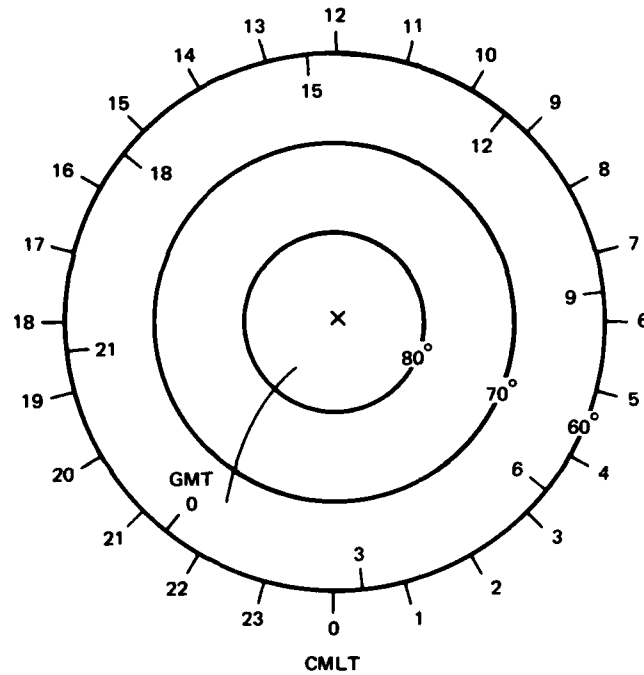


Figure 10. The path from Narssarssuaq to Thule at 0000 GMT in a coordinate system of invariant magnetic latitude and corrected magnetic local time.

Greenland, and valuable support was provided by the Greenland Technical Organization (GTO) and DMI. Copies of the VI sounder data from Sondre Stromfjord and from Godhavn were provided by Dr. Jens K. Olesen from DMI.

At the receiver site in Thule, the two loop antennas were separated by a distance of 61.3 m (201 ft) on a baseline perpendicular to the path from Narssarssuaq. Phase comparisons of signals received on these two antennas are thus unambiguous in defining off-path angles that deviate from the great circle by as much as 29° (at a nominal frequency of 10 MHz).

The initial experimental campaign was carried out in Greenland in the fall of 1984. Data were recorded for about 100 hrs on 13 days

between 2 October and 17 October 1984. The second campaign was conducted in the spring of 1985 to collect about 120 hrs of data during 16 days from 16 March through 1 April 1985. Most of these operations were in the mode with the standard 15-min sequence, but about 7 hrs of data were recorded on 1 April 1985 in the continuous sounding mode, giving a complete ionogram once each minute.

The last polar cap campaign in this series is planned for July and August 1985.

SECTION 4

DATA DESCRIPTION

Examples of the various types of data collected during this experiment are given in this section to illustrate the range of effects that were observed on different occasions. This presentation is primarily descriptive, but it provides a useful background for the analysis and interpretation of the data that are the subjects of Sections 5, 6, and 7.

4.1 Ionogram Data

Figure 11 is an illustration of the standard appearance of the oblique sounding data. Although this display was generated offline, the appearance of the data is the same as for the online display. The dark vertical lines in the data are a result of interference from other users of the HF spectrum, especially in the international short-wave broadcast bands. The signal that propagates from Narssarssuaq to Thule via a one-hop E-layer path appears at a delay time of 6.5 ms at frequencies between about 10 and 13 MHz. The one-hop F-layer signal trace is at slightly greater ranges and shows the characteristic shape produced by low-ray and high-ray signals that come together at the MUF for the path, in this case at about 14.5 MHz. The two-hop signal trace appears at appropriately lower frequencies and longer delay times in the upper left corner of the display. This ionogram was recorded under relatively quiet conditions, and it is shown here to illustrate the standard form that underlies the distorted features that appear under more disturbed conditions.

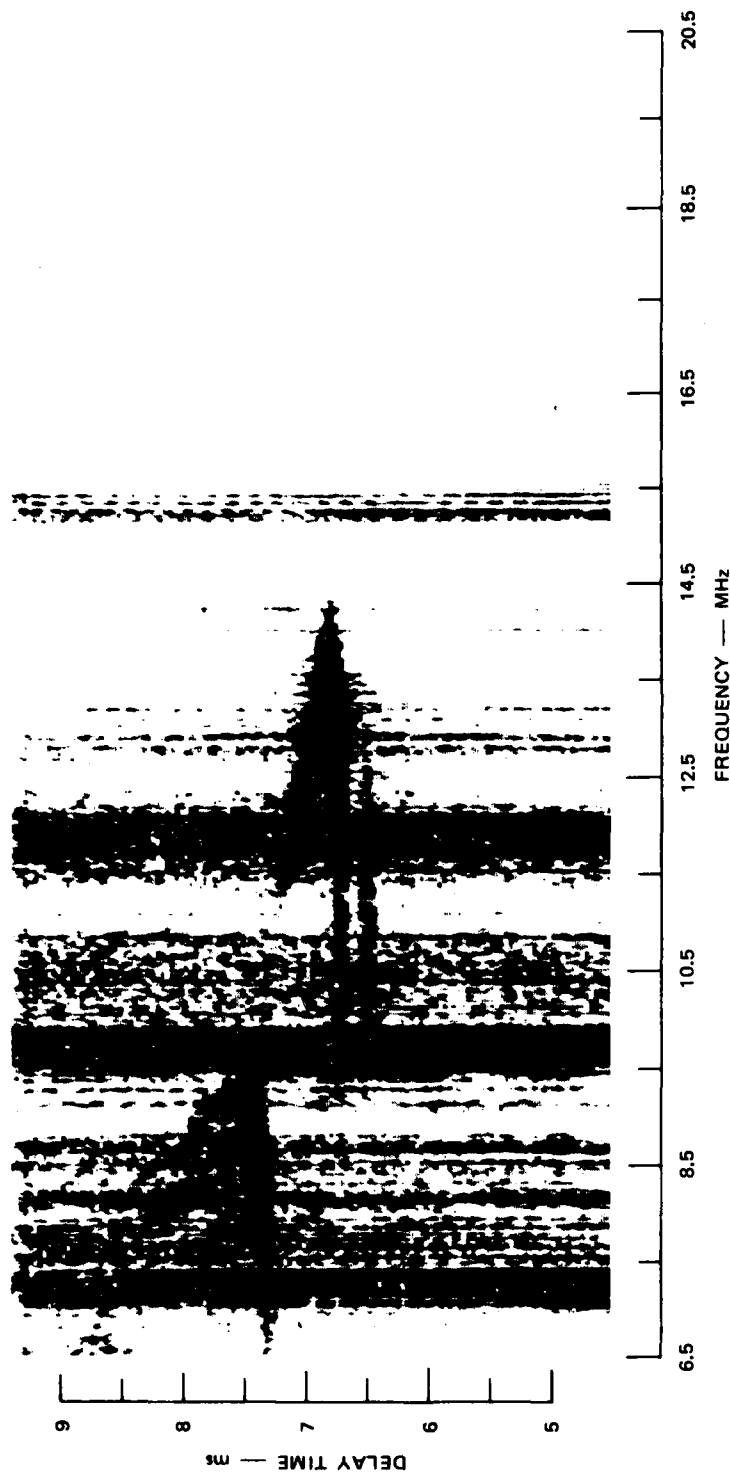


Figure 11. An example of an oblique ionogram showing E-layer and F-layer and one-hop and two-hop propagation for relatively undisturbed conditions on 17 October 1984 at 1716 GMT.

To illustrate the variety in appearance of the data, and also the time variability that is frequently observed, Figures 12 and 13 show a sequence of ionograms recorded at 15-min intervals over a period of an hour and a half. These ionograms, especially those shown in Figure 13, are the oblique counterparts of the traditional vertical ionograms that would be described as exhibiting spread-F echoes. It can be seen in Figure 13, especially on the ionogram for 2016 GMT, that range spreads on the order of a millisecond are observed, and these are not uncommon. Another feature that should be noted on these ionograms, on the three in Figure 13 in particular, are the sporadic-E traces that sometimes extend all the way to about 21 MHz.

As will be discussed in later sections of this report, the spread echoes that appear in Figures 12 and 13 can be interpreted in terms of the effects of scatter about the mean ray path and the effects of reflections from blobs of ionization located off the great circle path.

Another feature that should be noted, especially on the 1916 GMT ionogram in Figure 12 and all three ionograms in Figure 13, is the extension of the nose to frequencies higher than the junction frequency where the high-ray and low-ray traces come together. Nose extensions are also an effect of the scattering of energy by the structured plasma along the ionospheric raypaths.

4.2 CW Data

Figure 14 is an example of CW data recorded under moderately disturbed conditions. This record of the intensity modulated power spectrum data as a function of time shows gaps in the data that result from the various activities programmed into the standard 15-min sequence described in Section 2.3. In particular, no CW data are recorded during the first three minutes of each 15-min interval because this time is used for parameter changes, sounding, and the first long PRN dwell. At the beginning of subsequent minutes, gaps of either 7 s or 18 s occur

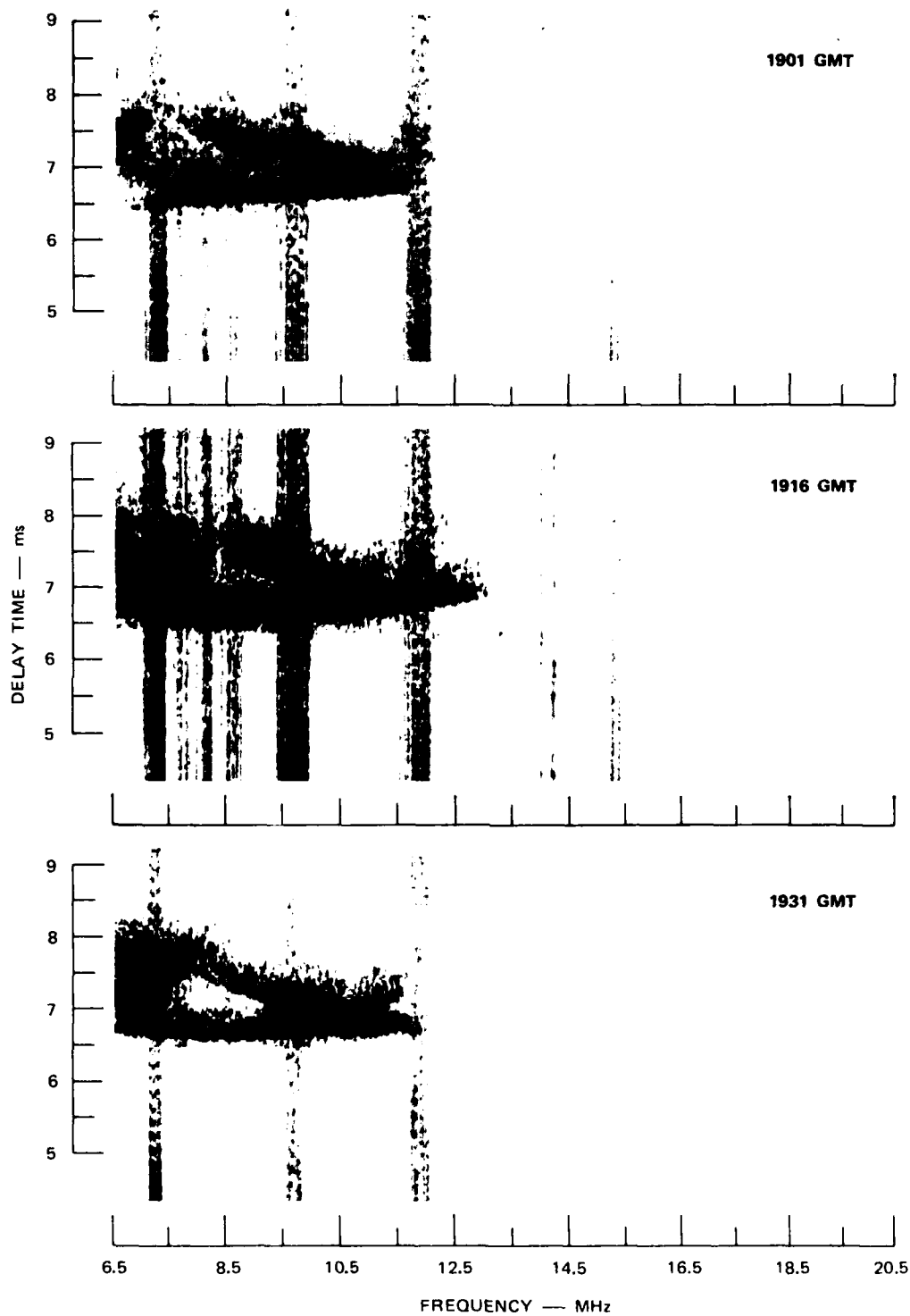


Figure 12. A sequence of ionograms recorded at 15-min intervals showing quiet and moderately disturbed conditions on 3 October 1984.

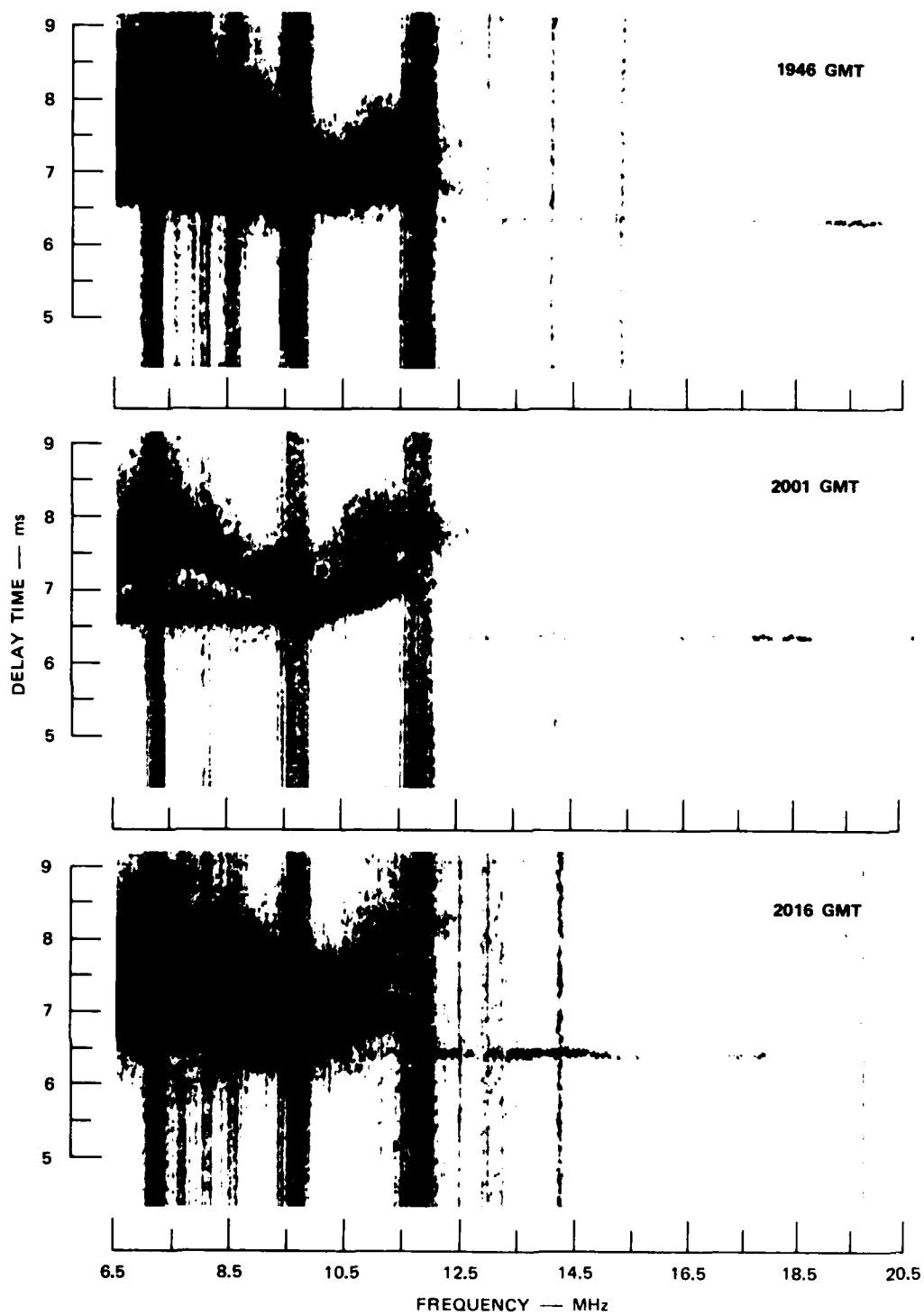


Figure 13. A continuation of the ionogram sequence in Figure 12 showing more severely disturbed conditions.

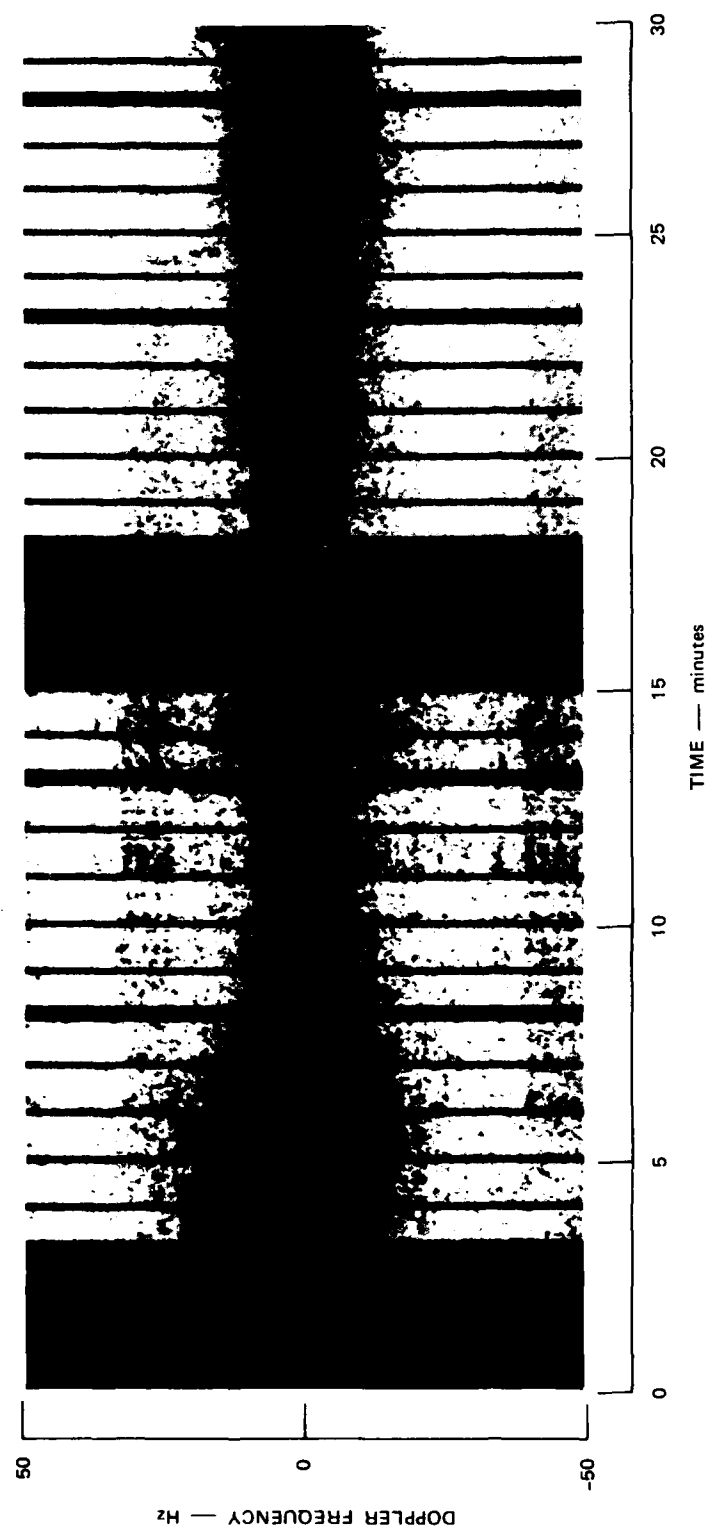


Figure 14. An example of CW data recorded at 10.120 MHz over a 30-min period starting at 1900 GMT on 8 October 1984.

during the time devoted to the short and long PRN dwells. In spite of these gaps, the CW data provide a good summary overview of the general disturbance conditions along the path, and particularly of the time variation of these conditions as reflected by the width of the Doppler spectrum.

For the sample of data shown in Figure 14, conditions were mostly quiet to moderately disturbed. The increase in the width of the spectrum during the first five minutes can be considered an indication that a patch of ionization somewhat more strongly structured than the ambient background has drifted across the propagation path.

Figure 15 is an example of the appearance of the CW data for a period of an hour under more disturbed conditions. The width of the Doppler spectrum at any given time is a result of the scattering of energy about the mean ray path as discussed in detail in Section 7. Of course, for the CW data, the received spectrum corresponds to the summation of the spectra of the signals received on all the individual raypaths (such as E-layer and high- and low-ray F-layer modes) that propagate at the particular frequency of the CW transmission.

4.3 Range-Resolved Doppler Data

Although a power spectrum analysis is performed online to generate the displays of the PRN dwell data shown in Section 2.4, the raw data from the ADCs are recorded on magnetic tape to permit flexibility in the methods used in offline processing and analysis of these data. Figure 16 is an example of the spectrum in a single 50- μ s range gate in receiver 1 as computed offline. This example is selected from the PRN-dwell data for which the online display was shown in Figure 7. It can be seen in this example that the spectrum is spread over nearly the full unambiguous Doppler extent of ± 40 Hz at a level of about 35 dB down from the peak at 0 Hz. For cosmetic purposes, the data are smoothed by calculating a 12-point running average, which for the 13.056 s coherent integration time corresponds to averaging over slightly less than 1 Hz.

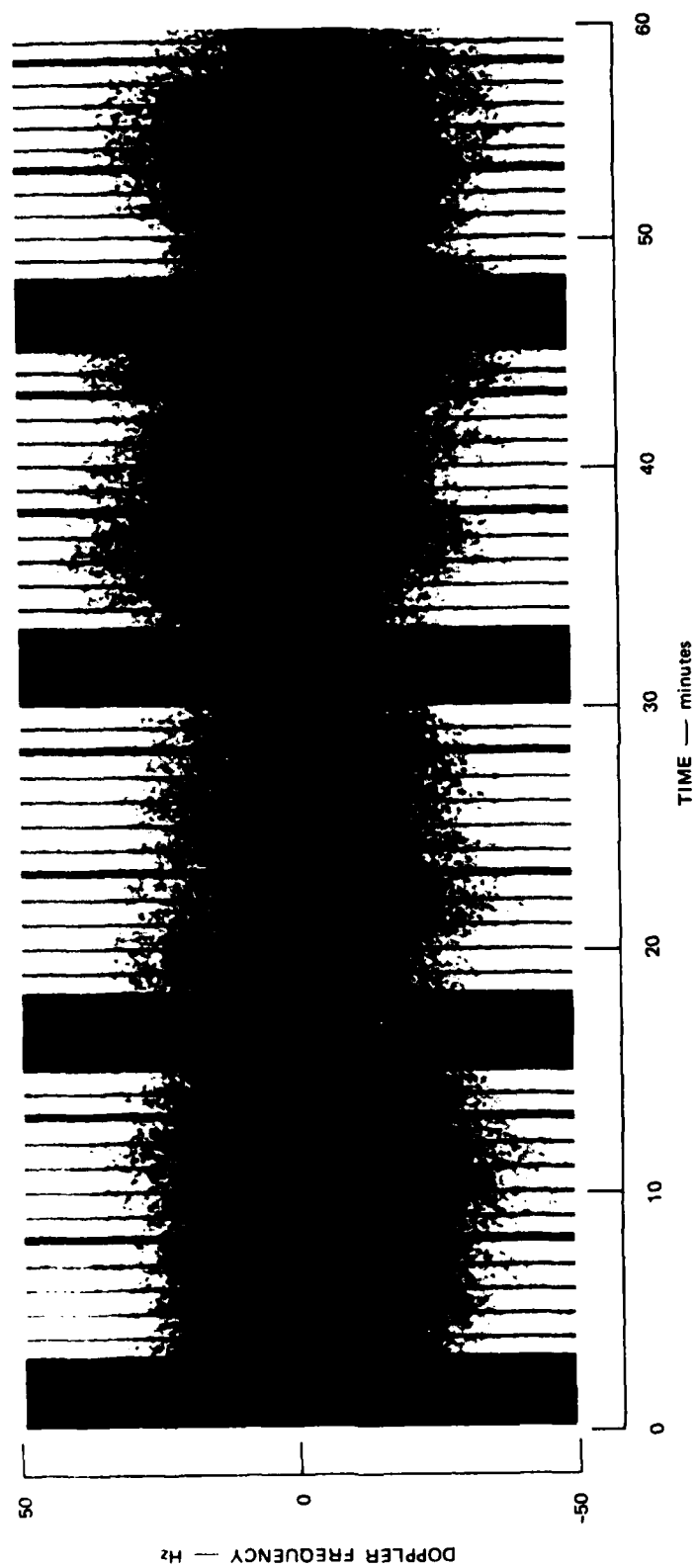


Figure 15. An example of CW data at 10.610 MHz under relatively disturbed conditions for one hour starting at 1515 GMT on 3 October 1984.

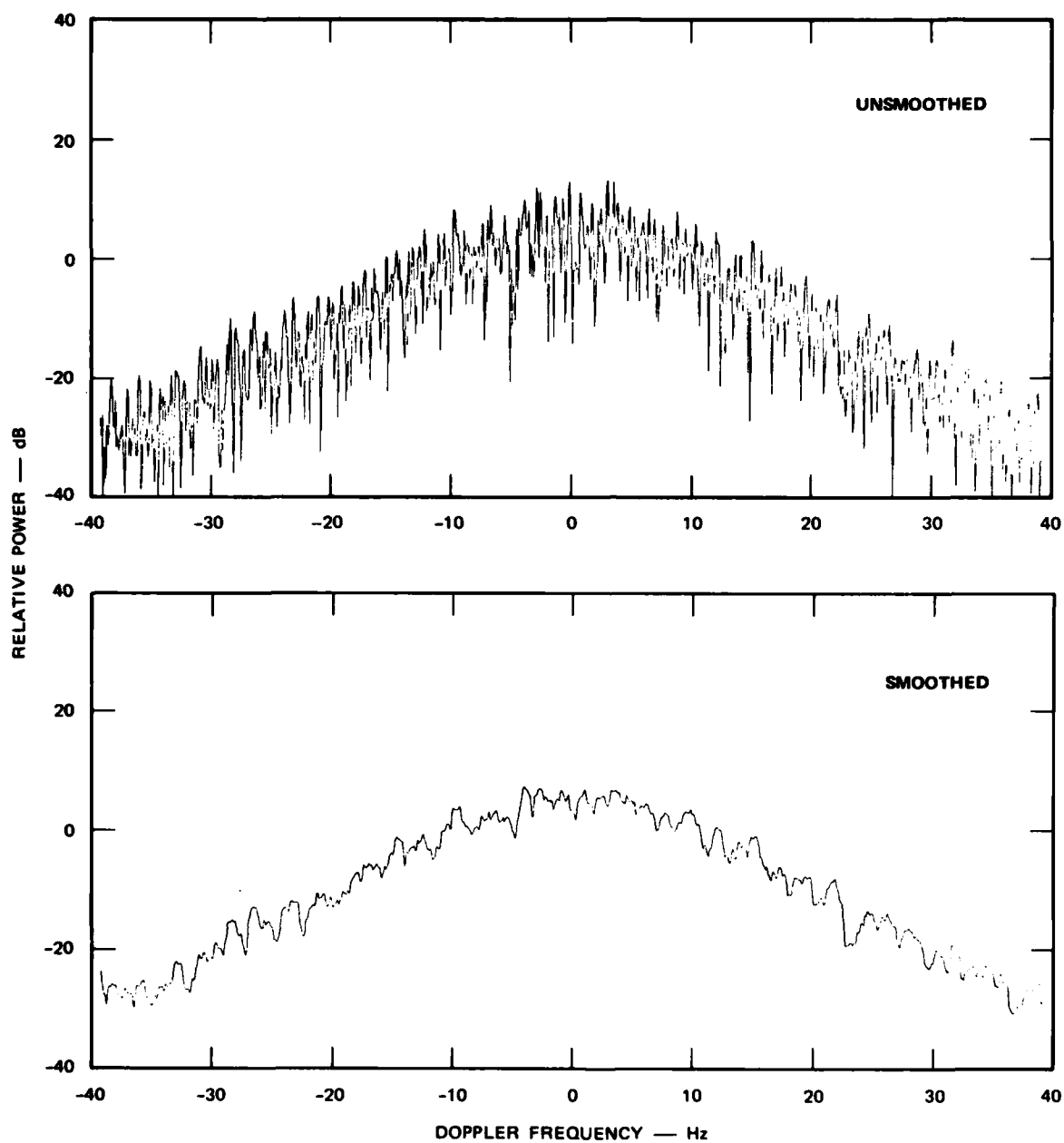


Figure 16. The appearance of the spectrum in range cell 8 of the PRN dwell data shown in Figure 7.

In some cases, it is desirable to display the results in terms of signal-to-noise ratio (SNR). Figure 17 is an example of a perspective

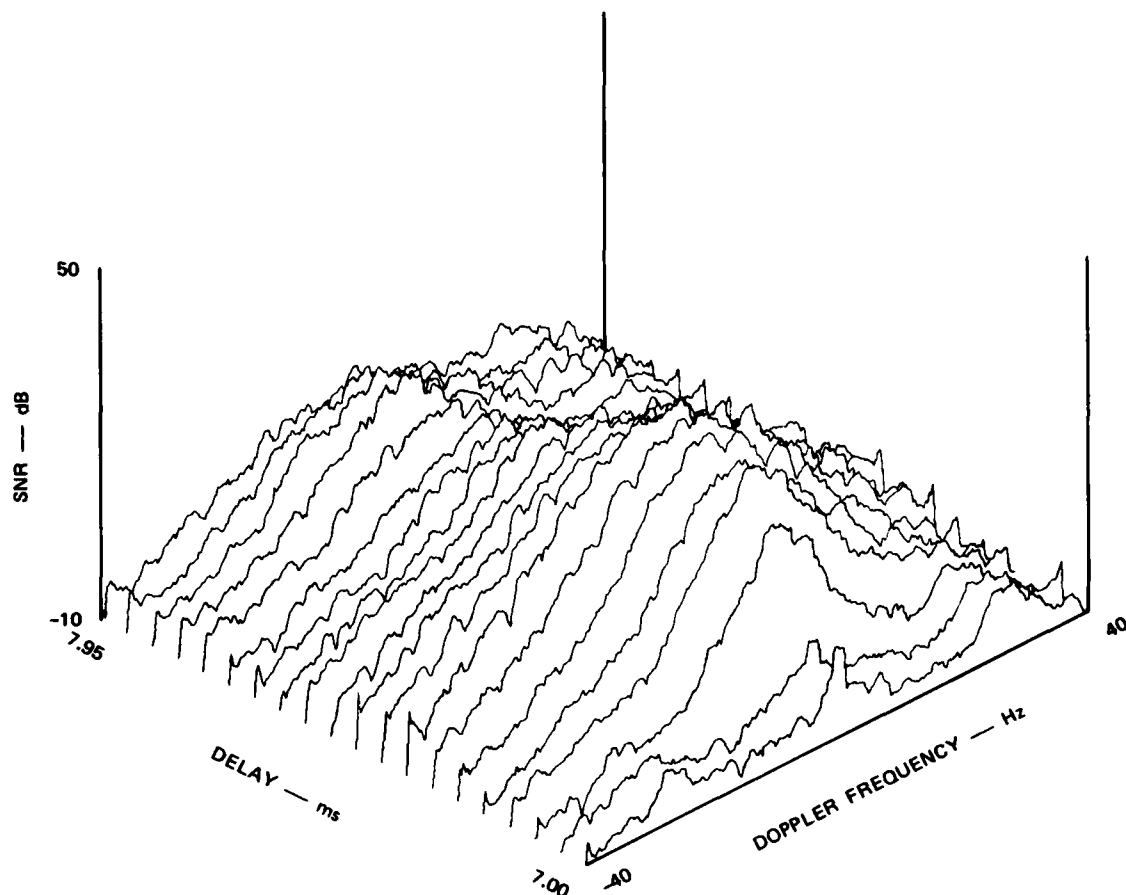


Figure 17. A perspective display of SNR versus range and Doppler frequency for the PRN dwell data shown in Figure 7.

display of the same PRN dwell shown in Figure 7, except in this case the data have been smoothed and the noise level defined as the average of the fifty lowest values of power contained in the $512 \times 20 = 10,240$ range-Doppler cells.

As a standard for comparison of the wide Doppler spreads recorded in the polar cap, Figure 18 shows an example of the spectrum recorded

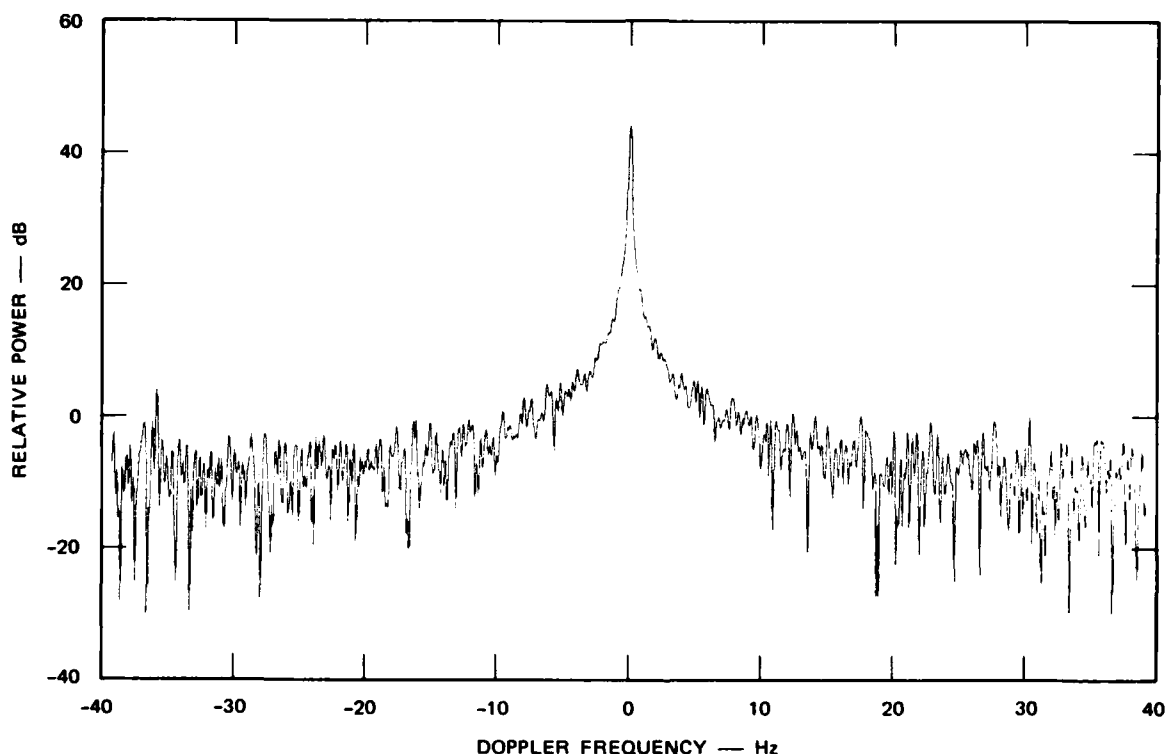


Figure 18. An example of the Doppler spectrum recorded in California for benign ionospheric conditions.

under benign ionospheric conditions in California during a system test in August 1984 before the HF Channel Probe was deployed in Greenland. For this test, the transmitter was in Lost Hills, California, and the receiver was 276 km away on the Stanford University campus. Although received over a short one-hop path, the very narrow spectrum shown in Figure 18 with an SNR of about 60 dB can be considered typical of signals that propagate via ionospheric paths in temperate latitudes where structured plasma does not occur as it does in polar, auroral, and equatorial latitudes.

4.4 Phase Data

By measuring the phase difference $\Delta\phi$ between the signals received on the two antennas separated by a distance D of 61.3 m, the angle θ between the antenna baseline and the incident rays is given by

$$\cos \theta = \frac{\lambda \Delta\phi}{360^\circ D} \quad (4.1)$$

where λ is the wavelength of the HF signal. To find the bearing error β , which is the angle in the horizontal plane by which the rays deviate from the great circle path (which at Thule was perpendicular to the antenna baseline), it is necessary to know the elevation angle ϵ of the rays. The bearing error β is then defined by the relation

$$\beta = \arcsin \left[\frac{\lambda \Delta\phi}{360^\circ D \cos \epsilon} \right] \quad (4.2)$$

As will be discussed in Section 5, ϵ can be defined simply from the measured delay time of the received signal. For a nominal delay time of 7.0 ms, ϵ is 16° , and for a nominal frequency of 10 MHz, λ is 30 m. In this case, β varies from 0° to 30.6° as $\Delta\phi$ varies from 0° to 360° .

Because the two receivers in the HF Channel Probe are not phase-matched, their phase difference may vary from one dwell to another. However, it can generally be assumed that the component of the signal received at a Doppler frequency of 0 Hz arrives along the great circle path, for which β is 0° and $\Delta\phi$ would be 0° if the receivers were phase-matched. Then β can be calculated by using in place of $\Delta\phi$ an effective value, $\Delta\phi$ (effective), defined as

$$\Delta\phi(\text{effective}) = \Delta\phi(0) - \Delta\phi \quad (4.3)$$

where $\Delta\phi(0)$ is the value of $\Delta\phi$ at the 0-Hz Doppler frequency.

In practice, the phase difference is computed by performing a cross-spectral analysis of the two signals. The FFT computation for each signal gives a real and imaginary component in each range and Doppler cell. The cross spectrum is then defined as the product of one set of values times the complex conjugate of the other, which yields the phase difference as the argument of the resulting complex product.

An example of the phase difference is shown in Figure 19 for the same PRN dwell and range cell for which the power spectrum was shown in Figure 16. As before, the smoothed data represent a 12-point running average of the raw data. Some of the scatter in the unsmoothed data is due to noise, but most of it is interpreted as an effect of scattering about the mean ray path.

Figure 20 shows the phase difference data for all twenty range cells recorded for this PRN dwell. It is the phase counterpart of the power-spectrum data shown in Figure 17. In this case, data for which the SNR is less than 10 dB are plotted as having a phase difference of 0° to reduce the distractions caused by noise.

Finally, Figure 21 shows the phase difference for benign ionospheric conditions in California. This figure is the phase counterpart of the power-spectrum data shown in Figure 18. The large variations caused by noise are clearly apparent outside of the region around 0 Hz where the peak of the power spectrum occurs.

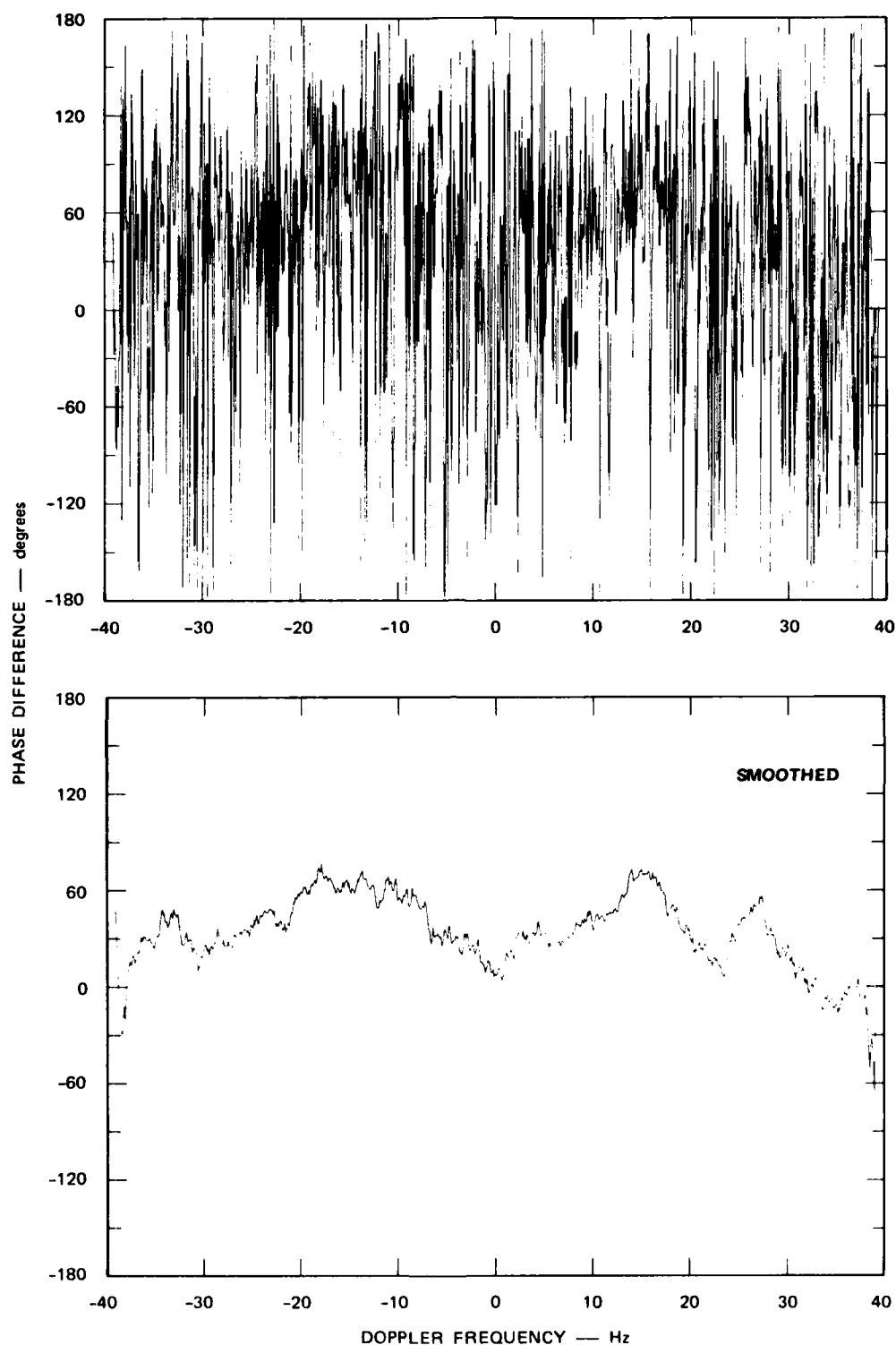


Figure 19. Phase difference between the same spectral components on the two receiver channels for the same data set for which the power spectrum was shown in Figure 16.

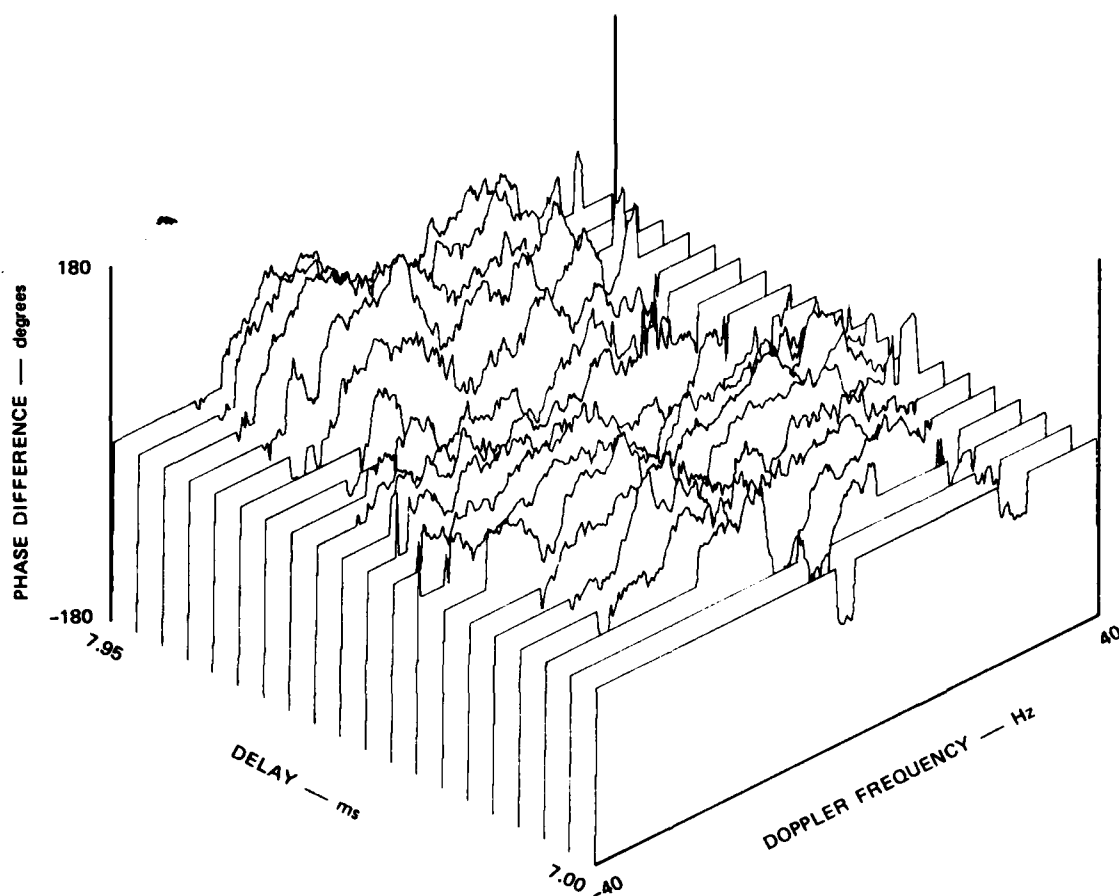


Figure 20. The phase of the cross spectrum (the phase counterpart of the power-spectrum data shown in Figure 17).

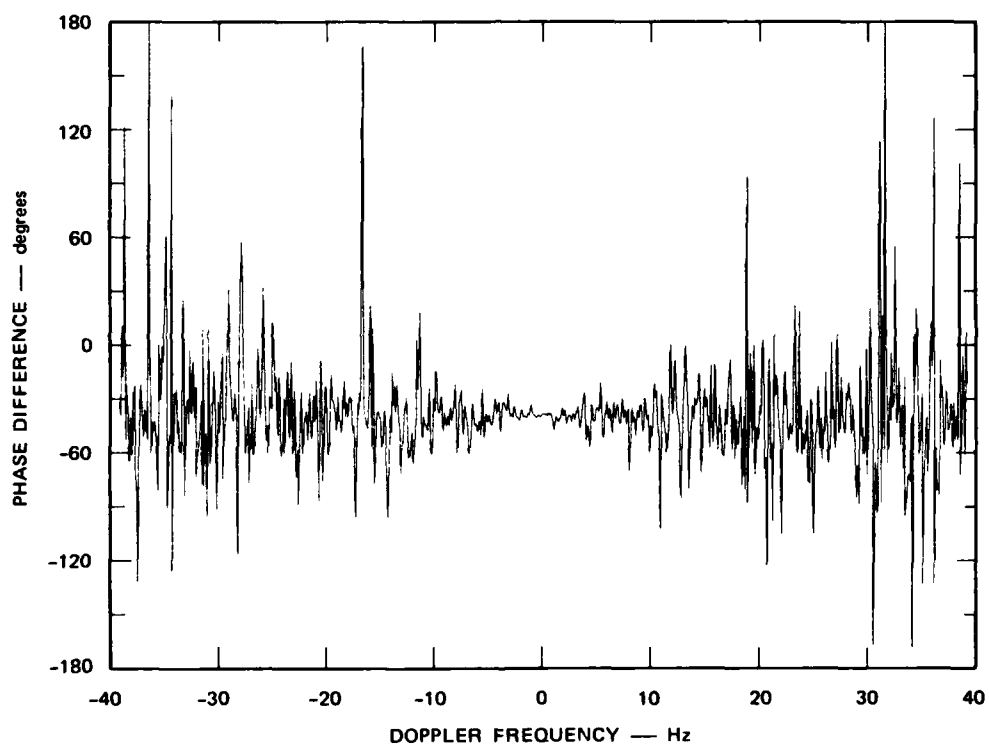


Figure 21. Phase difference for benign ionospheric conditions for the same data set for which the power spectrum was shown in Figure 18.

SECTION 5

IONOSPHERIC STRUCTURE AND PROPAGATION ANALYSIS

Although oblique ionograms show many interesting features that are produced by structured ionization along the sounding path (as illustrated in Section 4.1), the primary purpose served by the ionogram data for this experiment is to define the ionospheric profile and propagation modes that exist along the path at a given time. The ionization profile is the electron density as a function of height, and the propagation modes (such as E layer, or F-layer low ray, or F-layer high ray) are specified by the elevation (takeoff) angle and reflection height of the ray that is received at a given frequency and delay time.

5.1 Virtual Geometry

For a signal that arrives at the receiver with a delay time τ after propagating over the one-hop path from the transmitter, the virtual height h' at which the signal was reflected in the ionosphere can be calculated from the relation [Basler and Scott, 1973]

$$\left(\frac{c\tau}{2}\right)^2 = 2R(R + h') \left[1 - \cos\left(\frac{D}{2R}\right)\right] + h'^2 \quad (5.1)$$

where R is the radius of the earth (6359 km for the latitude of Greenland), D is the great circle ground range from the transmitter to the receiver (1918 km for the Narssarssuaq to Thule path), and c is the velocity of light (300 km/ms). The elevation angle ϵ at which the signal leaves the transmitter and arrives at the receiver can then be calculated from the expression

$$\cos \epsilon = \frac{2(R + h')}{c\tau} \sin\left(\frac{D}{2R}\right) \quad (5.2)$$

In many cases, it is sufficient to know only h' and ϵ . However, in other cases for which it is necessary to take the effects of refraction fully into account, virtual geometry calculations are not sufficient, and ray-tracing solutions are required.

5.2 True-Height Profile

To perform ray-tracing calculations, it is necessary to know the true-height profile, otherwise known as the $N(h)$ profile, that is, the electron density as a function of height in the ionosphere. True-height profiles can be determined from oblique ionograms in a two-step process that involves first the transformation of the oblique ionogram into the equivalent vertical incidence ionogram recorded at the midpoint of the oblique path [Basler and Scott, 1973] and second the true-height reduction of the vertical ionogram data to the $N(h)$ profile [Thomas, 1959; Titheridge, 1967]. A one-step process for the determination of $N(h)$ profiles directly from oblique ionograms also has been presented recently [Reilly, 1985].

The oblique ionogram shown in Figure 22 has been selected to illustrate this procedure. Although there is a slight nose extension from about 12 MHz to 12.3 MHz, this ionogram is mostly free of scatter effects and shows a relatively clear mode structure with high- and low-ray F-layer traces and an underlying E-layer trace. After transformation to the equivalent vertical incidence ionogram and performance of the true-height analysis, the true-height profile calculated from this ionogram had a critical frequency of $4.421 \text{ MHz} \pm 0.201 \text{ MHz}$, a height of maximum ionization of $258.9 \text{ km} \pm 9.7 \text{ km}$, and a scale height, or semithickness, of $45.1 \text{ km} \pm 11.2 \text{ km}$. In addition to these three parameter values, the true-height analysis yields a profile made up of specific values of electron density at specific heights, but for present purposes, only the three parameter values are used.

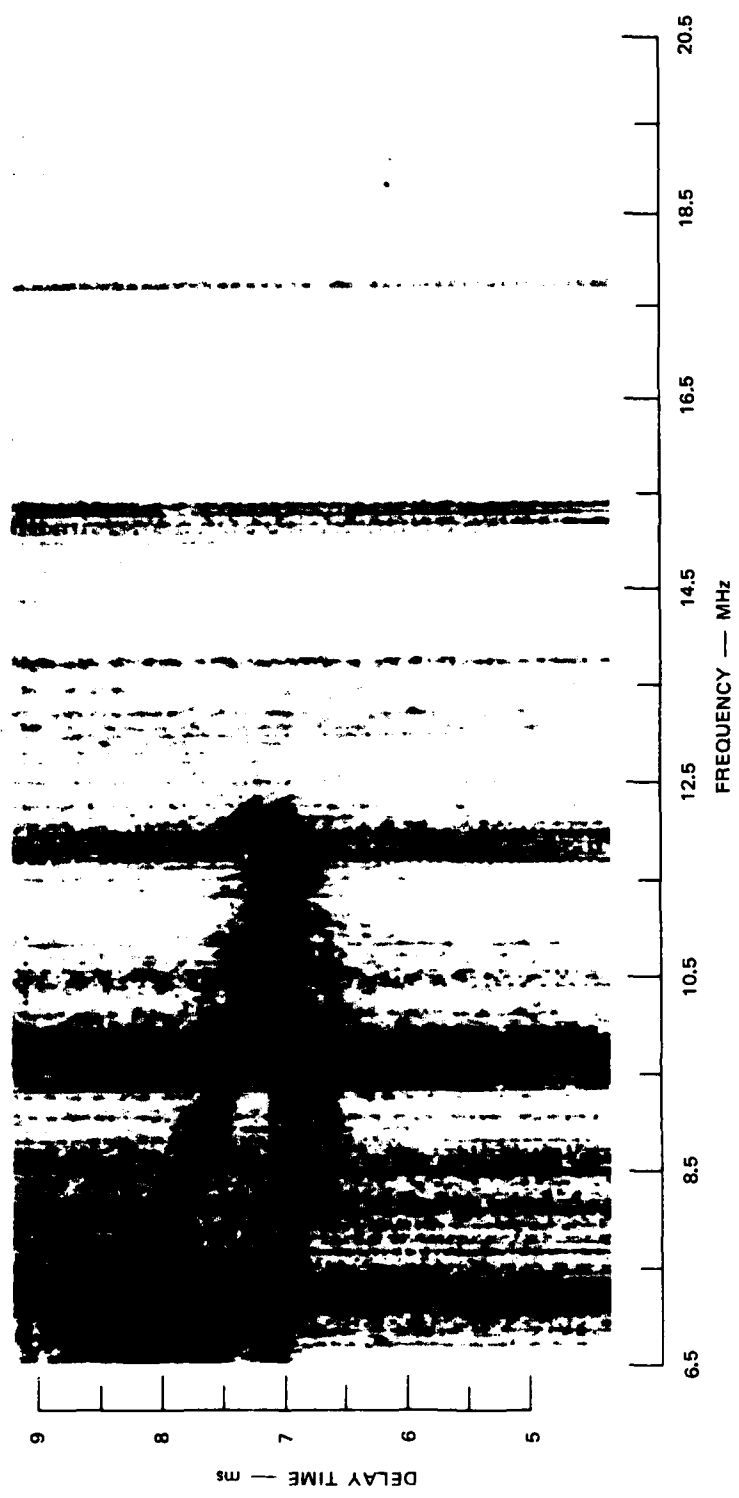


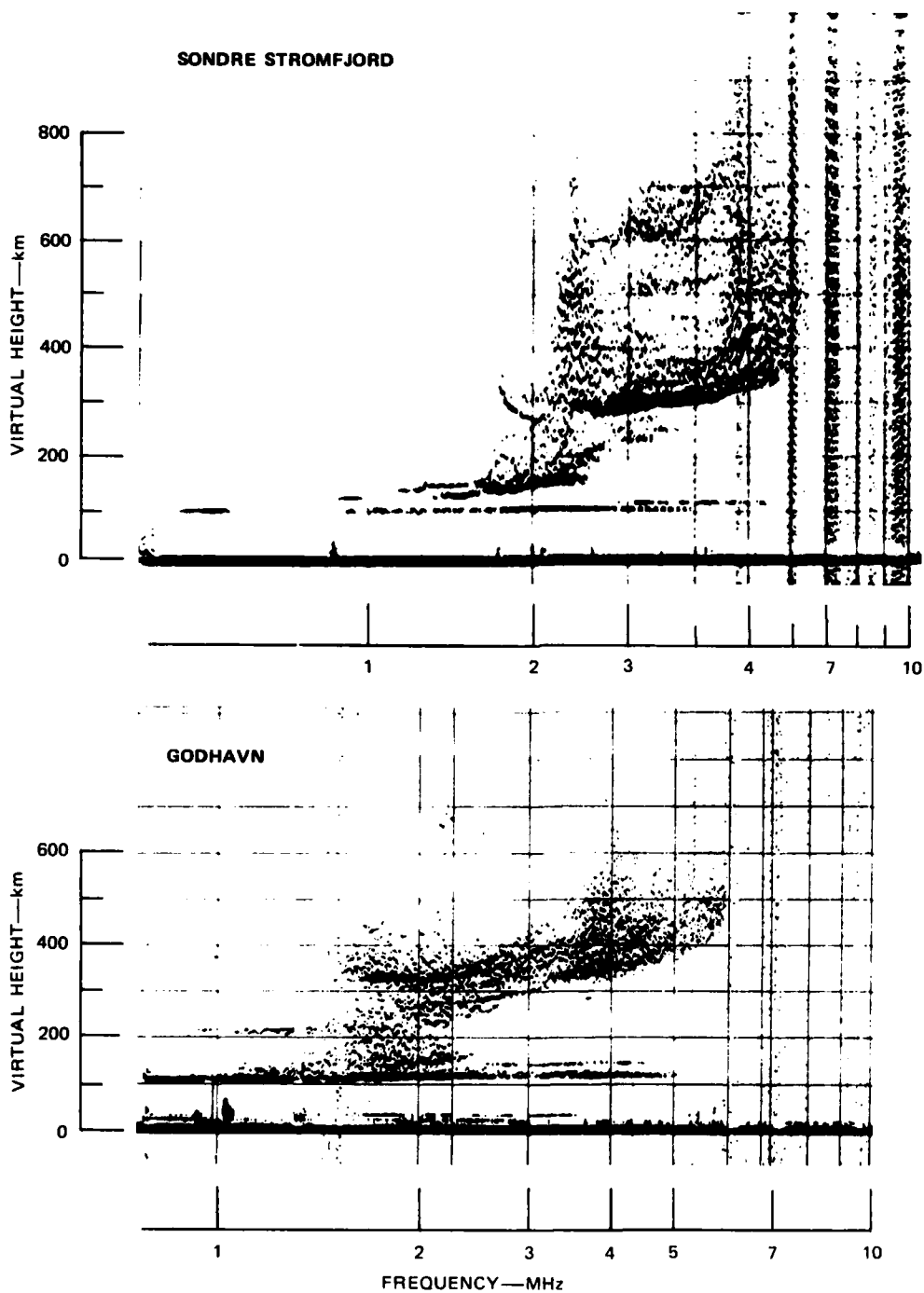
Figure 22. Narsarsuaq-to-Thule oblique ionogram recorded on 8 October 1984 at 1901 GMT.

As a check on the validity of these results, Figure 23 shows that the critical frequency ($f_o F_2$) is about 4.5 MHz on the vertical sounder records from Godhavn and Sondre Stromfjord. Godhavn is at the midpoint of the oblique path, so its vertical sounding data should be identical to the transformed oblique ionogram that was the basis of the true-height analysis. It should be noted that it is the ordinary ray trace that is mostly seen on oblique ionograms, and it is possible to discern the ordinary trace on the Godhavn and Sondre Stromfjord ionograms to scale $f_o F_2$ as about 4.5 MHz in spite of the spread-F conditions.

5.3 Quasi-Parabolic Layer Model

When we want to define the refracted ray path through the ionosphere by ray tracing, it is convenient to approximate the true-height profile by a model layer in which the electron density varies as a quasi-parabolic (QP) function of height. The QP-layer model is chosen because it yields analytic expressions in closed form for all of the important ray-tracing results, including group delay time and ground range as a function of operating frequency, take-off angle, and the layer parameters [Croft and Hoogasian, 1968]. Quasi-parabolic layers are specified by only three parameters: the critical frequency (FC) of the layer; the height of maximum electron density (HM); and the semithickness (YM).

Because exact expressions for all ray-path parameters are available, QP-layer models are especially useful in cases (such as those described in Section 7) for which we want to investigate the effects of small differences between rays that are nearly identical. In these cases, the results can be accepted with confidence, because they are not influenced by approximations inherent in the ray-tracing calculations. Also, the analytic expressions can be evaluated quickly (and thus cheaply) using even a small digital computer.



[Courtesy of J. K. Olesen of the Danish Meteorological Institute]

Figure 23. Vertical ionograms recorded on 8 October 1984 at 1859 GMT.

For the calculations presented in this report, ionospheric structure is approximated using a single QP layer to represent the F layer. As part of the continuing effort on this program, we plan to expand this model to include three QP layers to represent the underlying E-layer and F_1 -layer ionization as well as the F_2 -layer ionization.

5.4 Ionogram Synthesis

When a QP layer is chosen to approximate the true-height profile, delay time as a function of frequency is calculated for both high and low rays to synthesize an oblique ionogram that can be compared with the real ionogram recorded during the experiment. In this manner, the accuracy and consistency of the results can be checked for a series of steps that lead from the experimental oblique ionogram, to the transformed equivalent vertical incidence ionogram, to the true-height profile, to the quasi-parabolic layer model, and, finally, to the synthesized oblique ionogram. All of these steps involve approximations and simplifying assumptions, so it is important to establish that this loop closes properly before using the QP ray tracings for other data analysis applications.

In practice, the three parameters of the model QP-layer are set equal to those given by the true-height analysis. These parameter values are then adjusted slightly until the synthesized ionogram is in sufficiently good agreement with the experimental ionogram.

Figure 24 shows the result of this process for the ionogram shown previously in Figure 22. In this case, the synthesized ionogram agrees with the leading edge of the experimental ionogram to within about 10 μ s at frequencies above about 8.5 MHz and the QP layer parameters are all well within the bounds of uncertainty defined by the true height calculation. At frequencies lower than about 8.5 MHz, the experimental low-ray F-layer trace shows increasing retardation that results from underlying ionization that is not represented by the synthesized

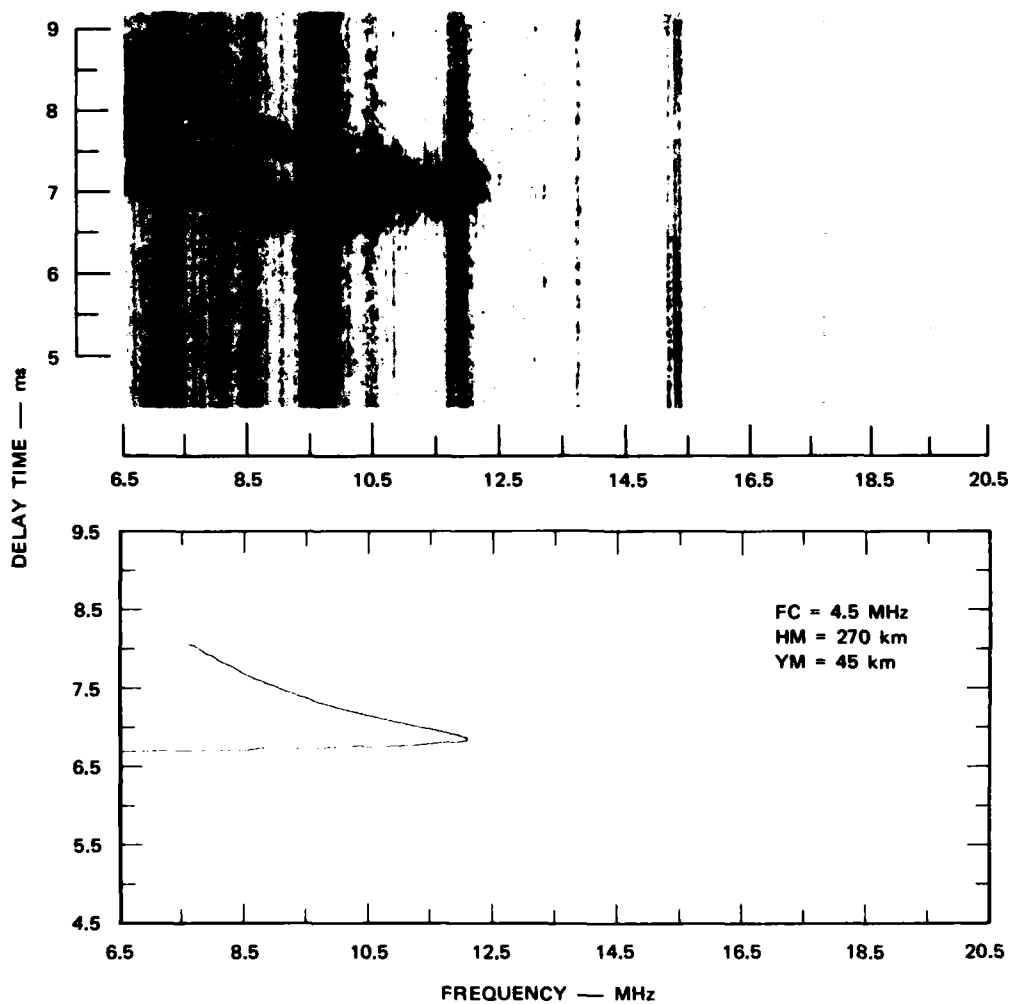


Figure 24. Comparison of a synthesized ionogram with the experimental ionogram shown in Figure 22.

ionogram for the present model with a single QP layer. However, the shape of the synthesized ionogram will accurately reflect this retardation at low frequencies when the model ionosphere is extended to include three QP layers.

Also, note that the high ray is not shown in the synthesized ionogram at frequencies below about 7.5 MHz. High rays could not be calculated for lower frequencies because the computer was not able, even in double precision, to calculate accurate ray paths for angles that deviated from the penetration angle by less than about 10^{-13} radians. However, this limitation is of no practical consequence for present applications.

In any event, for purposes of this report, the single layer model is adequate, because the synthesized and experimental ionograms show very good agreement in the vicinity of 10.120 MHz, the frequency of the PRN dwell for which QP ray tracing is used in Section 7 to compute the effects of small angle scatter about the mean ray path.

SECTION 6

INTERPRETATION IN TERMS OF GEOPHYSICAL PLASMA DYNAMICS

6.1 Background

HF radio propagation is affected by a variety of high-latitude phenomena associated with the visual aurora and other less prominent manifestations of ionospheric coupling with the outer magnetosphere. Magnetic field lines emanating from the earth at high latitudes are convected sunward on the dawn- and dusk-sides of the auroral zones. When they reach the noon sector, the field lines disconnect and merge with the solar interplanetary magnetic field. These open field lines then follow a complex trajectory antisunward across the polar cap that depends on the configuration of the interplanetary magnetic field. In the midnight sector, the field lines are drawn deep into the magnetosphere where they reconnect with field lines from the opposite hemisphere, and the process is repeated. The associated convection velocity in the ionosphere varies considerably in both time and space, sometimes exceeding 2 km/s. In the ionospheric F region, which is primarily responsible for refracting HF radio waves back to the earth, the plasma is essentially swept along with the flux tubes delineated by the magnetic field lines.

The merging and reconnection processes also create energetic charged particle reservoirs that cause the visual and subvisual aurora as well as large ionization enhancements in the E region where the particles encounter the dense atmosphere; however, E-region ionization recombines rapidly, so that the enhancements are found at this altitude only in the vicinity of the source. In the F region, ionization persists for many hours after it is created. Thus, F-region enhancements can move substantial distances from their sources, giving

rise to complex and rapidly changing ionization distributions. Figure 25 shows a typical ionization distribution measured over a

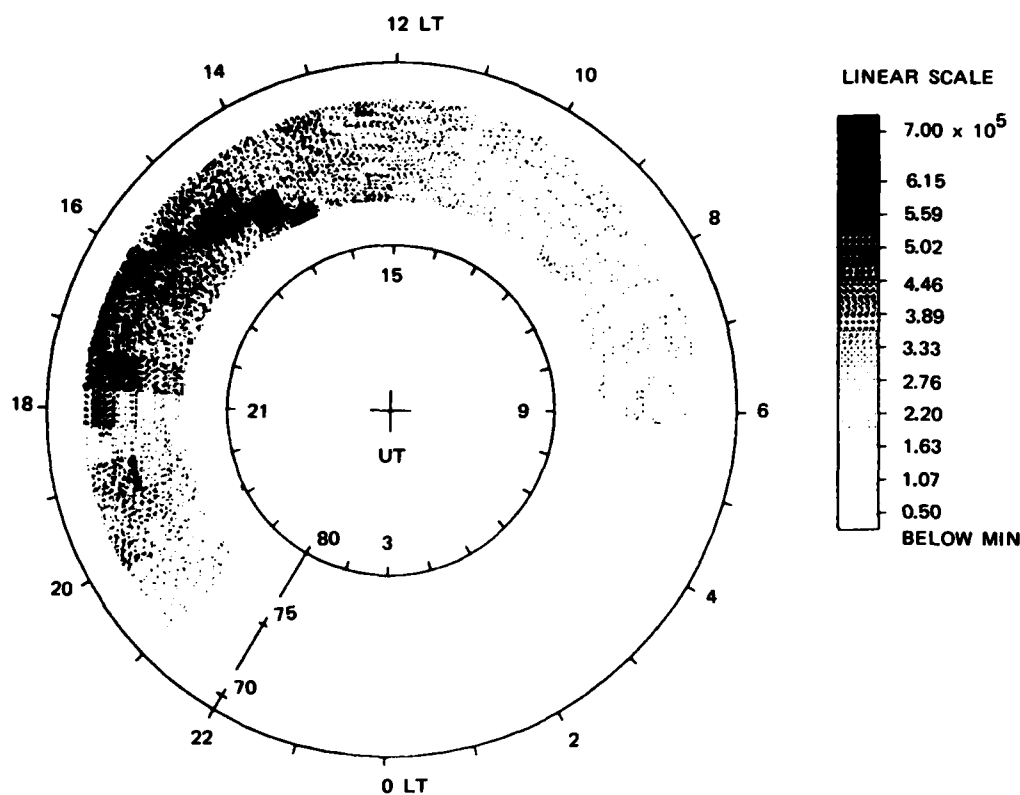


Figure 25. Electron density (el/cm³) at a height of 250 km as a function of invariant magnetic latitude and corrected magnetic local time as observed by the incoherent-scatter radar at Sondre Stromfjord over a 24-hour period on 18 May 1985.

24-hour period by the Sondre Stromfjord incoherent-scatter radar located along the path between Narssarssuaq and Thule as shown in Figure 9. The corresponding convection velocities are shown in Figure 26. The duskside ionization enhancement near the convection reversal from sunward to antisunward is the most prominent feature for this equinoctial day.

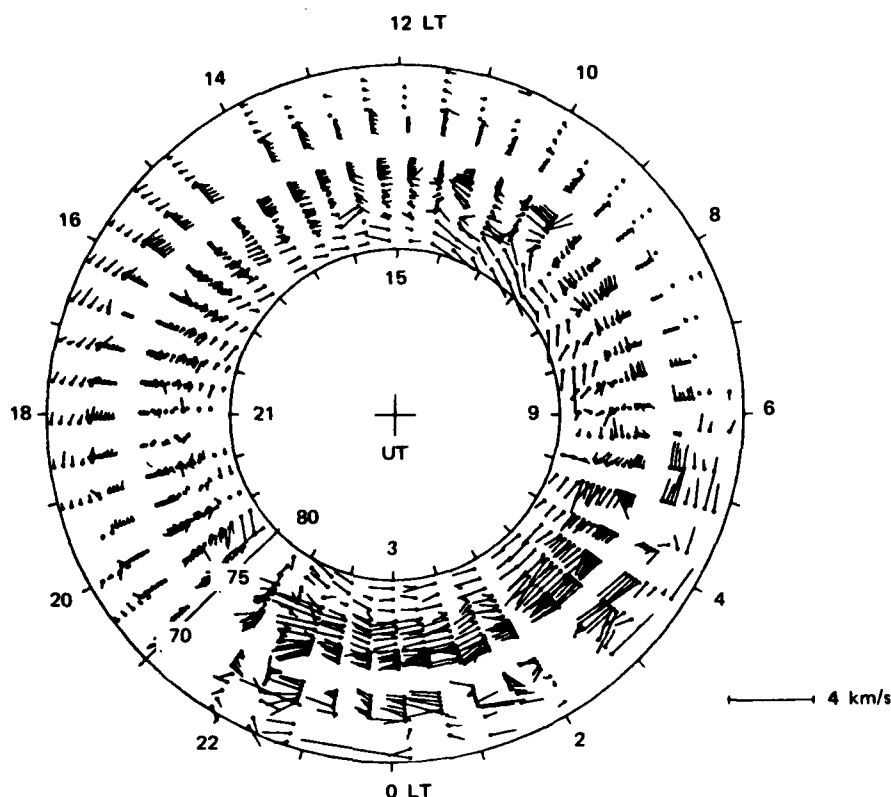


Figure 26. Plasma velocities corresponding to the electron-density data given in Figure 25.

For a typical propagation path in the polar cap such as that shown in Figure 10, it is clear that even in the absence of transient high-latitude phenomena such as substorms, HF propagation through the high-latitude regions can be extremely complicated. The HF Channel Probe is ideally suited for studying propagation in such environments; however, the primary objective of the experiments performed on this program has been to understand the effects of the intermediate-scale irregularities imbedded in the ionospheric layers, particularly in the F region. Early observations of radio-wave scintillation at high latitudes established the occurrence of such ionospheric irregularities as a regular auroral

phenomenon [Basler and De Witt, 1962; Aarons et al., 1969; Aarons and Allen, 1971, 1973; Basu, 1975]. Studies over the past two decades have refined and extended these observations.

On the dayside, an F-layer irregularity zone (FLIZ) in the region of the polar cusp where dayside merging takes place was first identified from aircraft HF sounder measurements [Pike, 1971; Snyder et al., 1973] and later in satellite HF sounder measurements [Dyson and Winningham, 1974]. On the nightside, our own analysis of spaced-receiver scintillation measurements showed that irregularities in the pre- and post-midnight sectors of the auroral zone have a high degree of spatial coherence along the L shell, which diminishes through the region of the Huring discontinuity where the nighttime convection reversal is observed [Fremouw et al., 1977; Rino et al., 1978; Rino and Matthews, 1980; Livingston et al., 1982]. In the polar cap, aircraft HF sounder, 6300 Å airglow, and scintillation measurements have isolated patches (under disturbed conditions) and sun-aligned bands (under quiet conditions) of enhanced irregularities in the polar cap F region [Weber et al., 1978; Buchau et al., 1978; Weber et al., 1984].

By combining incoherent-scatter radar and scintillation measurements, Vickrey et al. [1980] showed that a localized F-region electron-density enhancement was the source of a prominent nighttime auroral-zone scintillation feature. Basu et al. [1983] presented a case study of coordinated particle precipitation and scintillation measurements that showed coincident enhancements of low-energy particle fluxes and similar scintillation features. The F-region ionization enhancements, which are evidently the primary source regions for scintillation producing irregularities throughout the polar regions, are prominent high-latitude features, and they are actively being studied [Moshupí et al., 1979; Foster and Doupnik, 1984; Kelley et al., 1982; Robinson et al., 1984]. Precipitating low-energy electrons are believed to be the primary source of the nighttime enhancements [Tsunoda et al., 1985; Robinson et al., 1985; Foster and Doupnik, 1984]. As we noted above, in all cases convection plays an important role in the evolution of the ionization.

Kelley et al. [1982] proposed a unified irregularity model in which large-scale structure is produced in the major regions of particle precipitation in the daytime auroral zone and then convected into the polar cap and the nighttime auroral zone. Convection plays the dual role of transporting the large-scale structure away from the source region and providing a driving force that can generate small-scale structure, which is removed at sufficiently small scale sizes by diffusion. The diffusion mechanism and other aspects of structure formation are strongly affected by coupling of the F region to a highly conducting E layer [Vickrey and Kelley, 1982]. Kelley et al., [1982] also noted that structure can be imparted to the plasma directly via a structured ionization source or a structured velocity field mapped into the ionosphere and the magnetosphere.

The primary mechanism by which intermediate-scale structure is generated is believed to be a convective instability of which the gradient-drift and Rayleigh-Taylor instabilities are examples [Ossakow, 1979]. Linear theory shows that a uniform gradient along the convection direction is highly unstable; moreover, parallel currents act to further destabilize the plasma [Ossakow and Chaturvedi, 1979]. Thus, we expect to find the most intense structuring in such regions. As yet, however, the theory has not evolved to the point where we can predict the detailed shape and intensity of the spectral density function (SDF), which is the most commonly used measure of the structure characteristics.

From extensive radio-wave scintillation measurements, we have found that the one-dimensional SDF of the phase scintillation admits the multicomponent power-law representation

$$\Phi(f) = T_k f^{-p_k} \quad f_{k-1} < f < f_k \quad (6.1)$$

where T_k is the spectral strength for the power-law segment and p_k is the power-law index. The phase variance is obtained by integrating Eq. (6.1) over all temporal frequencies f . To relate these measurements

to in situ structure levels and ultimately the HF propagation effects of interest, we must use propagation theory and an appropriate structure model. The principal results are reviewed in the next subsection.

6.2 Ionospheric Structure Models

Because of the long lifetime of F-region ionospheric irregularities, we can assume that the irregularities are "frozen" during the measurement interval. Thus, it is only necessary to specify the average spatial characteristics of the irregularities. We assume that the structure is statistically homogeneous, at least locally, and the structure can be characterized by a three-dimensional spectral density function. For computations, we use the single power-law form

$$\phi(K, k_z) = \frac{abC_s}{[q_o^2 + q^2]^{\nu+1/2}} \quad (6.2)$$

In Eq. (6.2), q^2 is a quadratic form in the transverse, K , and vertical, k_z , wavenumbers as described in [Rino, 1982]. The parameters a and b are elongation ratios along and transverse to the magnetic field respectively, and q_o is the outer-scale wave number. It can be shown that the corresponding one-dimensional phase SDF for $f \gg q_o v_{eff}/2\pi$ has the form

$$\phi(f) = T f^{-p} \quad f \gg v_{eff} q_o / 2\pi \quad (6.3)$$

where

$$p = 2\nu \quad (6.4)$$

$$T = C_p G \frac{\pi^{1/2} \Gamma(\nu)}{\Gamma(\nu+1/2)} (2\pi v_{eff})^{2\nu-1} \quad (6.5)$$

and

$$C_p = r_e \lambda \mathcal{L}_s \quad . \quad (6.6)$$

Definitions of the geometry-dependent factors G and v_{eff} can be found in Rino [1982]. The effective scan velocity, v_{eff} , converts spatial wavenumbers to temporal frequencies as measured on a propagation path that moves relative to the structure. To evaluate v_{eff} , we must specify the relative drift rate and the anisotropy parameters.

This structure model as used in the HF propagation theory is summarized in Section 7. Computation of the phase structure at HF is more complicated primarily because of the continually varying propagation path. In effect, results such as Eq. (6.5) apply only locally. Nonetheless, the structure that causes scintillation and spread-F is the same. Thus, it is important to maintain a consistent characterization. The DNA HILAT [Fremouw et al., 1983] satellite is continually monitored from Sondre Stromfjord. Phase-scintillation data from HILAT have been processed to extract measures of the absolute structure levels and their morphology. To guide the interpretation of our HF data, we have summarized the principal results to date in the next subsection.

6.3 HILAT Results

Figure 27 is a clock-dial plot of the intermediate-scale spectral-strength parameter, T , in decibels averaged over more than one year's data from the Sondre Stromfjord station. The coordinates are invariant magnetic latitude and corrected magnetic local time, as in Figures 25 and 26. The phase structure shows a pronounced increase near 70° invariant latitude. The boundary is circular rather than oval. The most intense enhancements are observed between 70° and 75° , primarily on the duskside. Indeed, between midnight and 0600 CMLT almost no localized enhancements survive the averaging. The overall distribution of the spectral index values corresponding to data shown in Figure 27 is

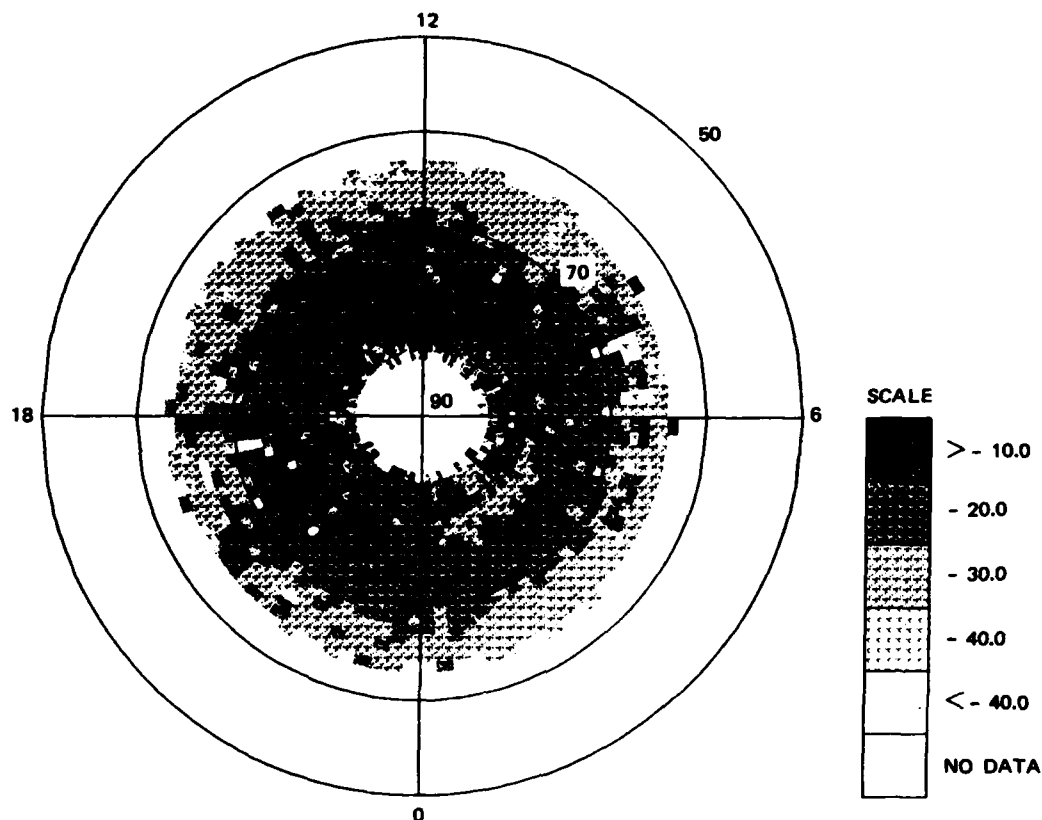


Figure 27. Irregularity strength parameter T in decibels averaged over more than a year at Sondre Stromfjord.

shown in Figure 28. The spectral index in the intermediate-scale regime undergoes subtle changes, but for our preliminary modeling work a fixed value between 2.5 and 3.0 is adequate.

As discussed in Section 6.2, we can use Eq. (6.5) to make a first-order correction for the geometrical dependence of the phase scintillation. Figure 29 shows the C_s values corrected for a 10:1 anisotropy and a 100-km layer thickness. The same general features are present in the C_s distribution, but the pattern is not nearly so uniform. This is due principally to the large variations in v_{eff} that occur for the different pass geometries. The fact that random localized

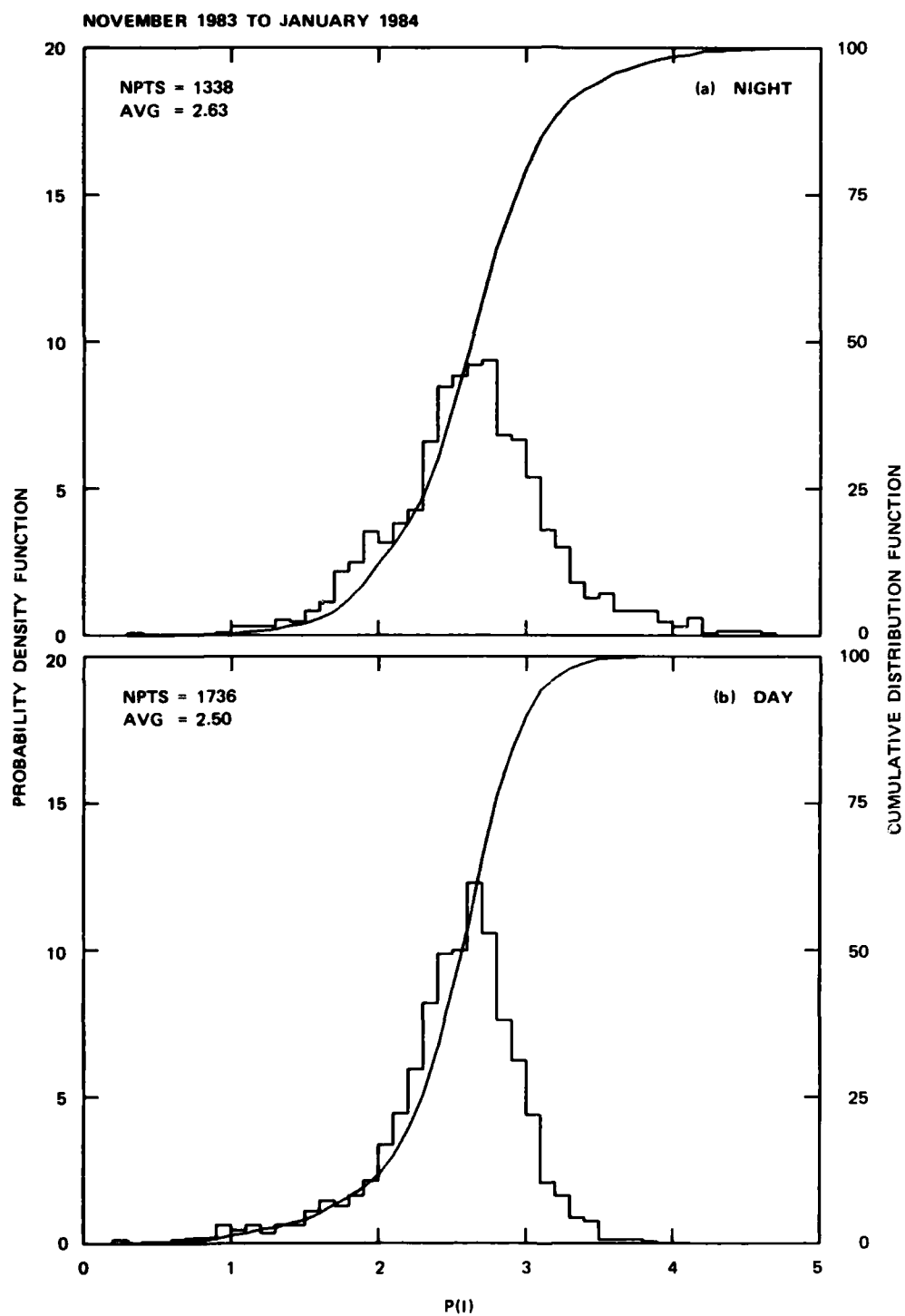


Figure 28. Distribution functions of the spectral index values corresponding to data shown in Figure 27.

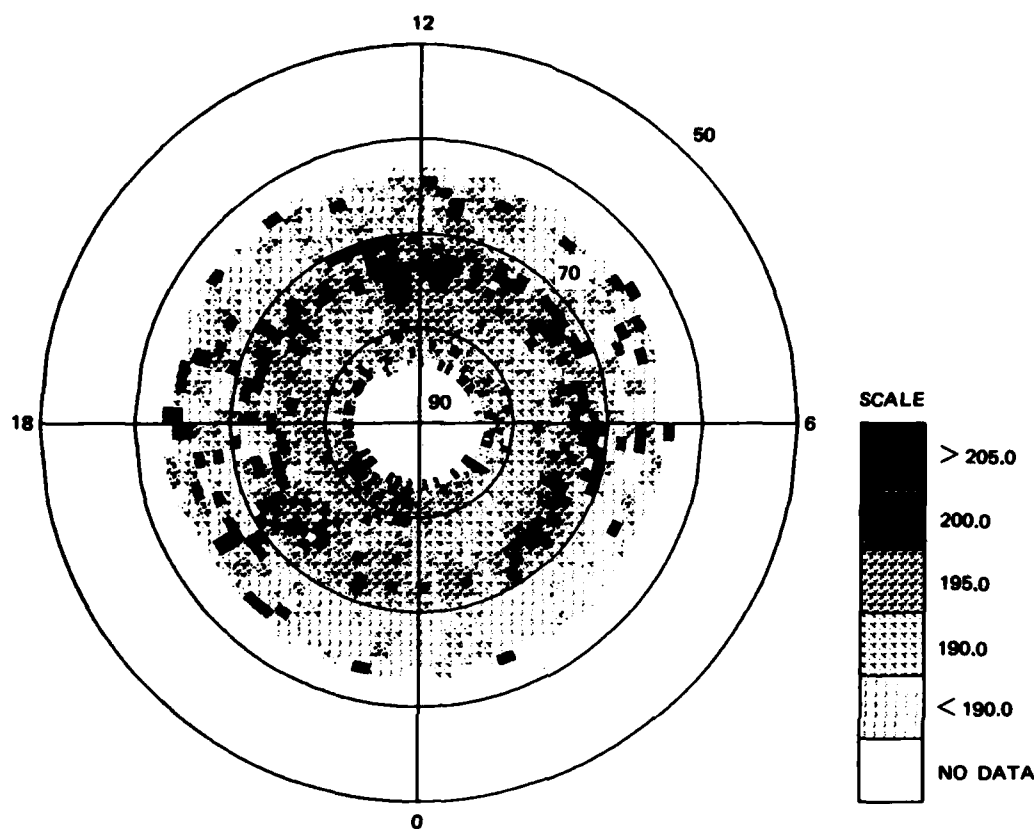


Figure 29. Clock-dial plot of C_s corrected for a 10:1 anisotropy and a 100-km layer thickness.

enhancements survive the geometry correction indicates that they are mainly source variations, although sheetlike structures could account for some of the enhancements at the extremes of the data set. In any case, the 10:1 anisotropy assumption is useful for evaluating the gross morphological features that we are interested in here. Typical structure levels are 10 to 20 percent of the background F-region density.

We now turn to the preliminary interpretation of some of the more interesting structure characteristics we have observed in the data obtained from our first two Greenland campaigns.

6.4 Effects of Moving Blobs

As discussed in Section 6.1, F-region ionization enhancements or "blobs" are presently receiving a considerable amount of attention from physicists. Theories about their formation are emerging, and we have established that blobs are the primary source regions for scintillation and, evidently, spread F as well. Insofar as HF effects are concerned, two different types of signal distortion are observed in the Doppler domain, namely, spreads and shifts of the received power spectrum. These effects are produced by two entirely different physical mechanisms. Doppler spreads are a result of the scattering process described in detail in Section 7, and shifts are caused by off-path reflections from moving blobs of ionization [Basler et al., 1973].

Figure 30 is an example of the standard signatures of these moving blobs as they appear in the CW data. The signals that appear in this figure separated from the direct path signal at 0 Hz and showing a positive Doppler shift that decreases with time are caused by reflections from blobs that are approaching the great-circle propagation path. The Doppler shift is positive when the out-of-plane path length grows shorter as the blob approaches the great circle. It is zero when the blob reaches the great circle and becomes negative as the path begins to lengthen after it crosses the great circle. Figure 31 is an example of one of these blob signatures with negative Doppler frequencies.

These blob signatures are themselves spread in Doppler frequency as well as shifted because they are subject to the same scattering effects that spread the direct path signals. Also, at times of severe spreading, it is likely that the combined spreads of the direct and off-path signals are often greater than the shift of the off-path signal, thus obscuring the fact that two separate signals are actually present.

The intensity and the frequency of occurrence of these blob signatures were reduced substantially (by more than an order of

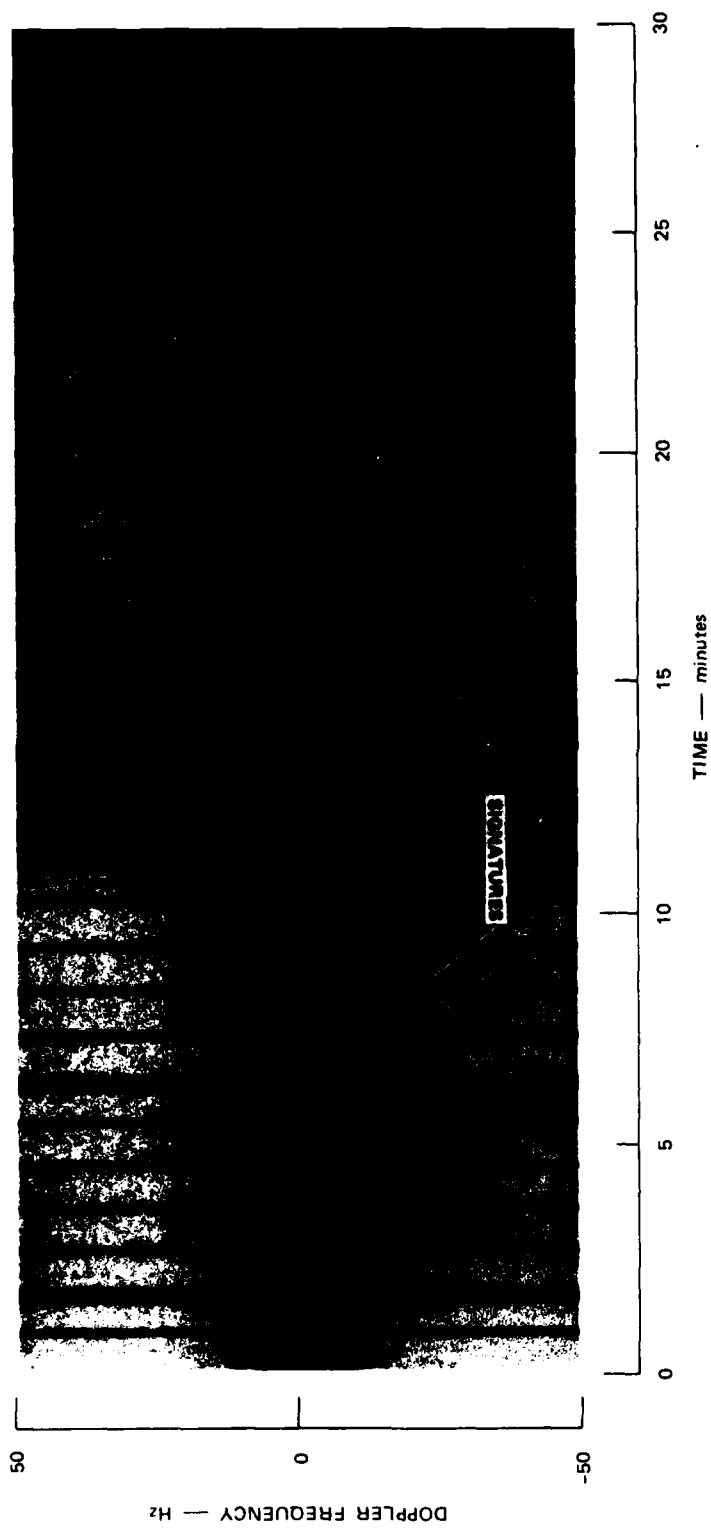


Figure 30. Signatures of moving blobs as they appear in CW data recorded at 10.120 MHz on 8 October 1984 starting at 1930 GMT.

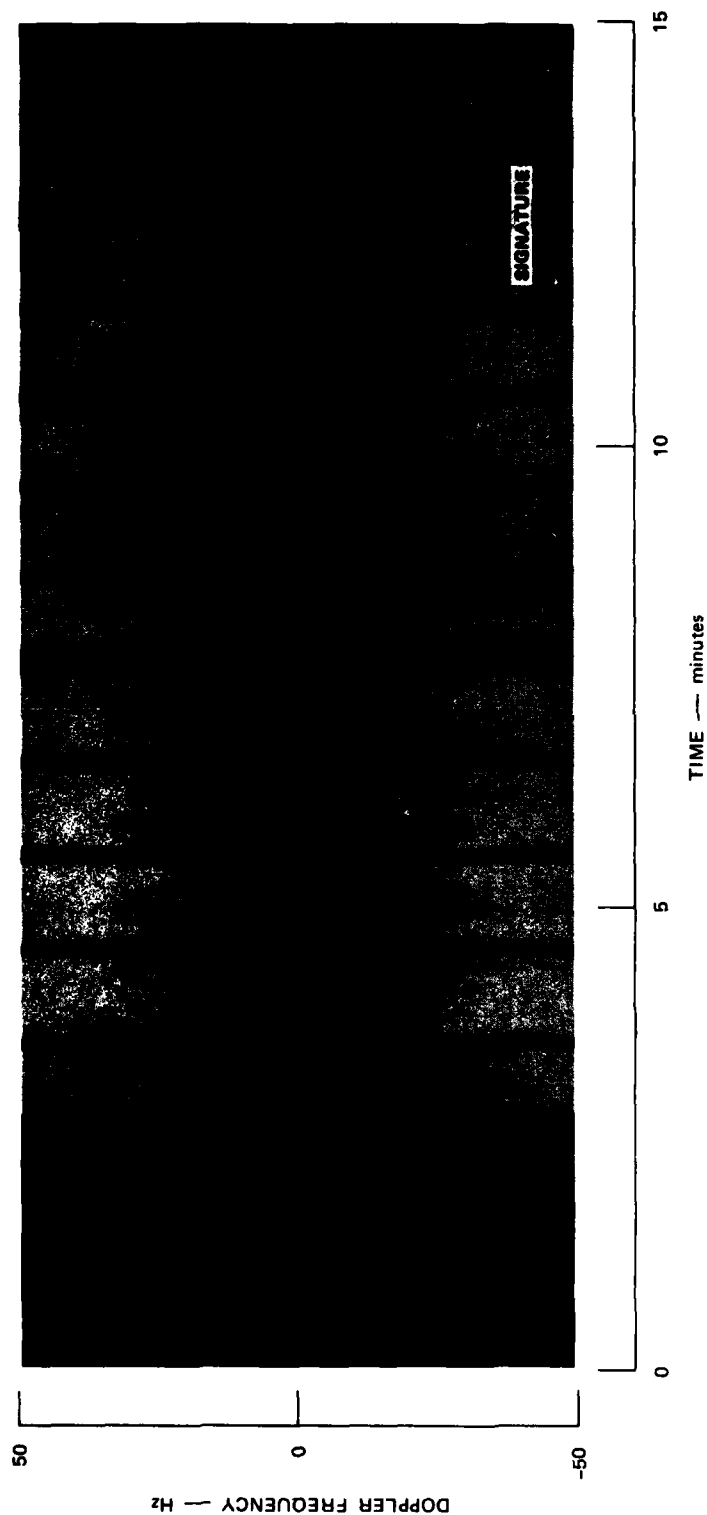


Figure 31. Signature of a moving blob with a negative Doppler frequency as it appears in CW data recorded at 10.240 MHz on 11 October 1984 starting at 1900 GMT.

magnitude) for the HF Channel Probe measurements compared to similar measurements made in the polar cap during August 1967 [Basler et al., 1973]. This reduction is interpreted as a solar-cycle effect because the 1967 measurements were made near the maximum of the sunspot cycle, whereas the present experiment is being carried out near solar minimum.

For a blob in a given location and traveling with a known speed and direction so that it crosses the great-circle propagation path between the transmitter and receiver, it is straightforward to calculate the signature that this blob would produce on the CW record [Basler et al., 1973]. However, it is not possible to invert this calculation to determine the blob location and vector velocity from the CW data alone. For this reason, the HF Channel Probe operating format was arranged so that the CW data are interrupted once each minute to obtain the PRN-dwell data. The PRN-dwell data define the range, virtual height of reflection, and azimuthal angle of arrival of each Doppler component of the signal.

In particular, simple equations have been derived to express the path length (range) and the bearing of the blob signal in terms of the latitude and longitude of the blob. Setting these expressions equal to the measured values of range and bearing permits them to be solved for the two unknowns (blob latitude and longitude) at the time of the PRN dwell. The validity of the position as a function of time as determined in this manner from the PRN dwell data can then be confirmed by calculating the CW signature that would be caused by this particular blob trajectory and comparing it to the observed signature.

Calculations of this type are planned as part of the continuing analysis of the Channel Probe data.

6.5 Acoustic Gravity Waves

On a few occasions, the CW data had a rippled appearance in which the Doppler frequency of the received signal varied quasi-periodically. Figure 32 is an example of one of these records. The Doppler frequency

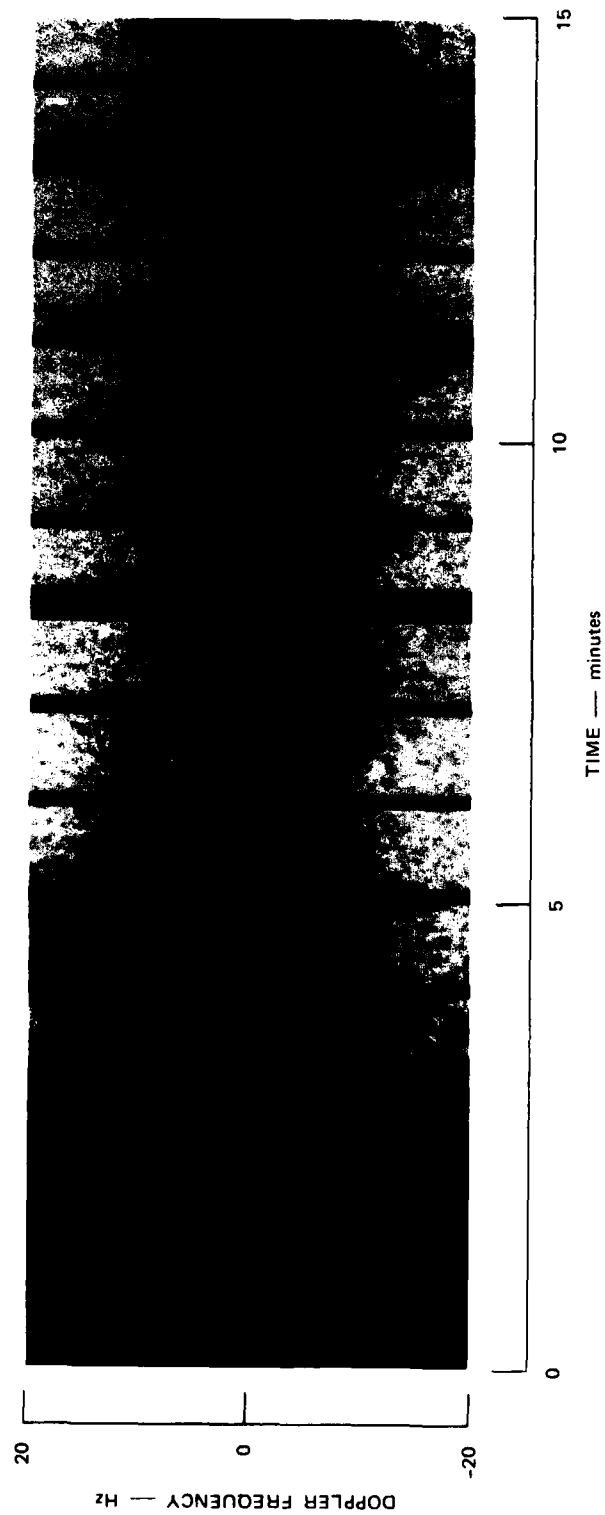


Figure 32. An example of a CW record for 8.990 MHz starting at 2015 GMT on 10 October 1984 showing quasi-periodic variations that are interpreted as an effect of acoustic-gravity waves in the ionosphere.

scale for this figure has been expanded to show only ± 20 Hz instead of ± 50 Hz as has been the case for CW data shown in other figures. The Doppler frequency excursions in this case are about ± 5 Hz with a period of about a minute or two.

By comparing the spread of the spectrum in this figure with the spreads shown previously in Figures 14 and 15, it can be seen that the data in Figure 32 were recorded under relatively quiet conditions. It was typically quiet also when the other cases with a rippled appearance were observed, probably because any effect that may have been present would be obscured by the wide Doppler spreads that are present under more disturbed conditions. Conditions were generally quiet enough to be able to recognize these events for about a third of the operating time during this experiment, but even during these quiet conditions, events were observed at a rate of only about one per four or five hours of data.

Events of this type are interpreted as an indication of the passage of acoustic-gravity waves in the ionosphere across the midpoint of the propagation path. Periods on the order of a minute as observed here would be classified as acoustic in nature because their periods are too short to be considered as gravity waves. However, it is unlikely that gravity waves, for which periods would be 15 min or longer, could be easily detectable in the midst of the other disturbances that appear in the data.

The variation in Doppler frequency with time for these events can be interpreted simply in terms of the horizontal passage of acoustic-gravity waves through the ionospheric reflection region at the midpoint of the propagation path. The acoustic-gravity-wave train consists of alternating regions of compression and rarefaction. When the ambient plasma is compressed, the electron density increases at each altitude, causing the height of reflection of the radio waves to decrease and the path length to shorten, which in turn causes the Doppler frequency to

shift from zero to a positive value. In the same manner, rarefactions produce negative Doppler shifts.

No attempt has been made here to identify the sources of these acoustic-gravity waves, but it is noted that a variety of sources, including supersonic aircraft, earthquakes, explosions, and severe weather, have been reported previously [Marcos, 1966; Wolcott et al., 1984; Barry et al., 1966; and Georges, 1968].

6.6 Time and Height Variations of Doppler Data

It is apparent from the examples of CW data shown in previous sections (Figures 14 and 15, for example) that the spectral width of the received signal changes with time in response to large-scale changes in the structured-plasma environment along the propagation path. Of course, the CW data have no range resolution and, thus, represent the summation of all different modes of propagation that may exist at a given time. However, the PRN dwell data can be used to define the spectral response to the plasma environment and its changes with time in individual range cells, each corresponding to a specific ionospheric path with its associated virtual height of reflection.

Two different analysis techniques have been used to characterize the spectral data for the PRN dwells. First, Doppler moments were calculated for the SDF in each 50- μ s range cell. The first moment gives the centroid and the second moment the spread of the SDF. Unfortunately, because of the large number of other users of the HF spectrum, interfering signals were present along with the HF Channel Probe signal for most of the PRN dwells. The interfering signals were usually much weaker than the Channel Probe signals. They typically appeared at a constant Doppler frequency with a uniform amplitude in all range cells, so they can be readily distinguished from the desired signal in a display of the data. In an attempt to reduce the effect of these interfering signals on the computerized data analysis and to exclude cases for which the desired signal was absent in a given range cell because of the particular propagation modes that were present for a

given measurement, data were considered in a given range cell only when the peak SNR in that range cell was greater than or equal to 20 dB. Although this technique eliminated much of the effect of the interfering signals, some effect remained, and it is not known to what extent it contaminates the moment calculations.

The second analysis technique was devised specifically to eliminate almost all effects caused by interference and to give a more complete characterization of the spectral density function. In this case, data were considered not only when the peak SNR in a given range cell was greater than or equal to 20 dB, but also only when the peak occurred at a Doppler frequency between plus and minus 10 Hz. Very few legitimate HF Channel Probe signals were eliminated by these criteria, but cases with strong interfering signals at large Doppler shifts were excluded from the analysis. For data that satisfied these criteria, the spectral density function was characterized by noting the position (Doppler frequency) of the peak and the width of the spectrum in 1-dB steps below the peak down to a level at which the signal was 5 dB above the noise. For the results to be presented here, only the long PRN dwells were considered. As mentioned previously, these long dwells were recorded at 5-min intervals.

Figure 33 shows an example of the time variation of the received signal over the course of one day's operation as defined by these two analysis techniques. For this example, the range gate at 7.1 ms, corresponding to F-layer low-ray propagation with a virtual height of reflection of 400 km, was selected, although, of course, the results are also available at other range gates. Discrete points are plotted in this figure to emphasize the fact that data are generally available every five minutes, but sometimes they are not available either because the mode structure did not give a signal in the 7.1-ms range cell in a particular case, or the criterion of a 20 dB or greater peak SNR within ± 10 Hz was not satisfied. The spectral width data are shown in this figure only for 20 dB down from the peak although data are available at other levels, down to 40 or even 50 dB in some cases.

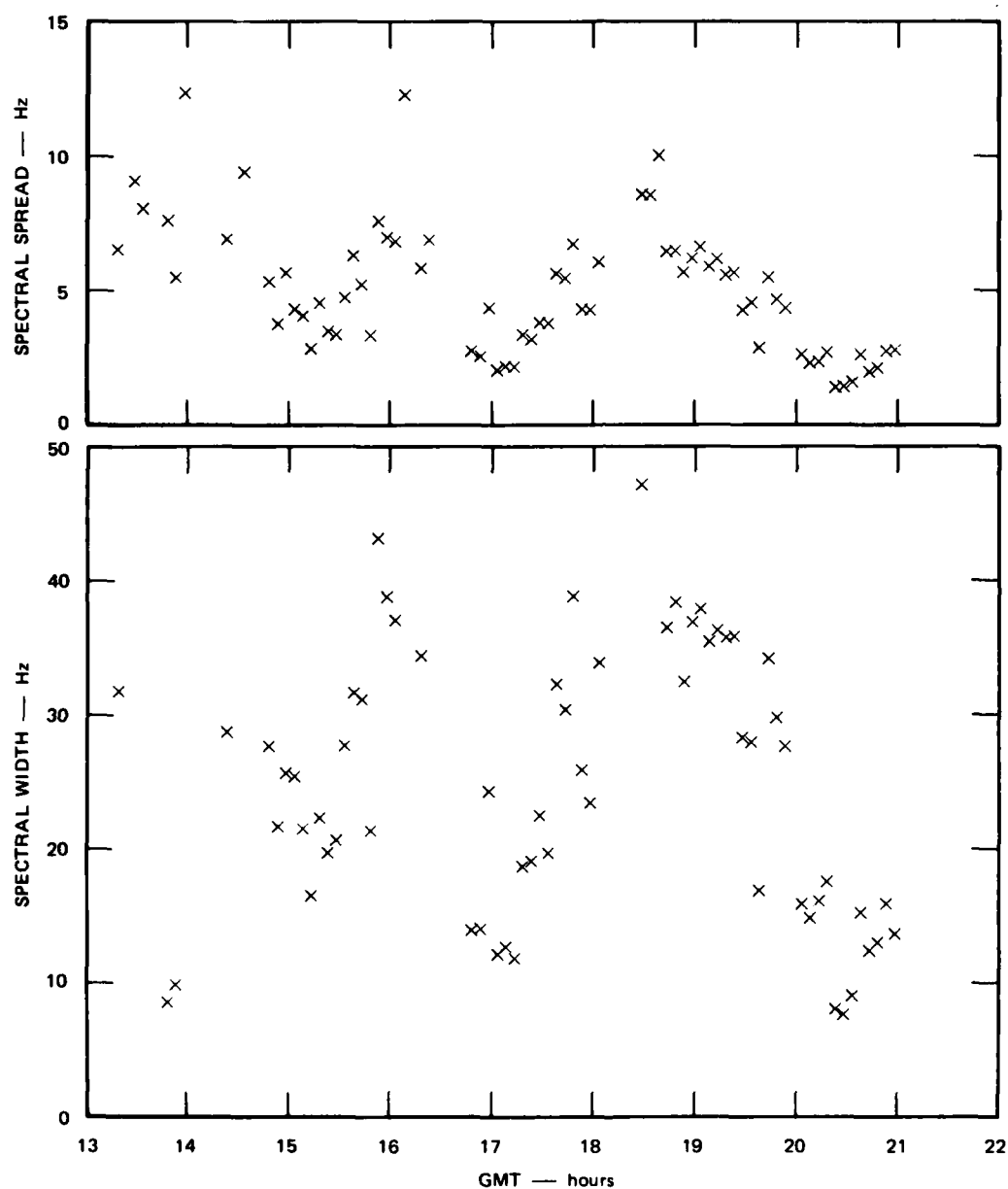


Figure 33. Variations of spectral width (20 dB down from peak) and spectral spread (second moment) with GMT on 3 October 1984 for F-layer low-ray propagation (7.1-ms delay time).

It can be seen in Figure 33 that there were large variations in the width and spread of the spectrum over the course of the operation. In particular, relatively quiet and disturbed periods, each with a duration of an hour or two, alternated throughout the operation. These variations evidently are the effect of large patches of structured ionization, with dimensions on the order of a thousand kilometers, drifting across the propagation path. These patches of structured ionization presumably break off from the daytime auroral zone and are swept up into the polar convection pattern as discussed in Section 6.1.

Similar presentations of the variations of Doppler shift with time for this same day are given in Figure 34. Doppler shift is shown both as the Doppler frequency at which the maximum SNR occurs and as the centroid (first moment) of the spectral density function. Somewhat surprisingly, no obvious pattern is present in this example or in others that have been examined.

To examine the question of whether or not the time variations of the spectral data exhibited any consistent diurnal pattern, the PRN dwell data were combined for all the days of operation during both the fall and spring campaigns. Figure 35 shows the results in terms of the means (solid lines) and standard deviations (dotted lines) of the spread and width of the spectral density functions in the 7.1-ms range cell. For this figure, means and standard deviations are not plotted for a given GMT if there were not at least five data points available for computing these quantities. The maximum number of data points at any particular GMT was sixteen (representing measurements on sixteen different days). It can be seen in this figure that there is a general tendency for spectral width to decrease over the period from 1400 GMT to 2300 GMT, but there are also large variations that mask this trend. The trend is not apparent in the data for the spectral spread (second moment), but this can be attributed to contamination by interference as discussed previously. Nevertheless, the trend for the spectral width is significant, and it is consistent with the concept of patches of

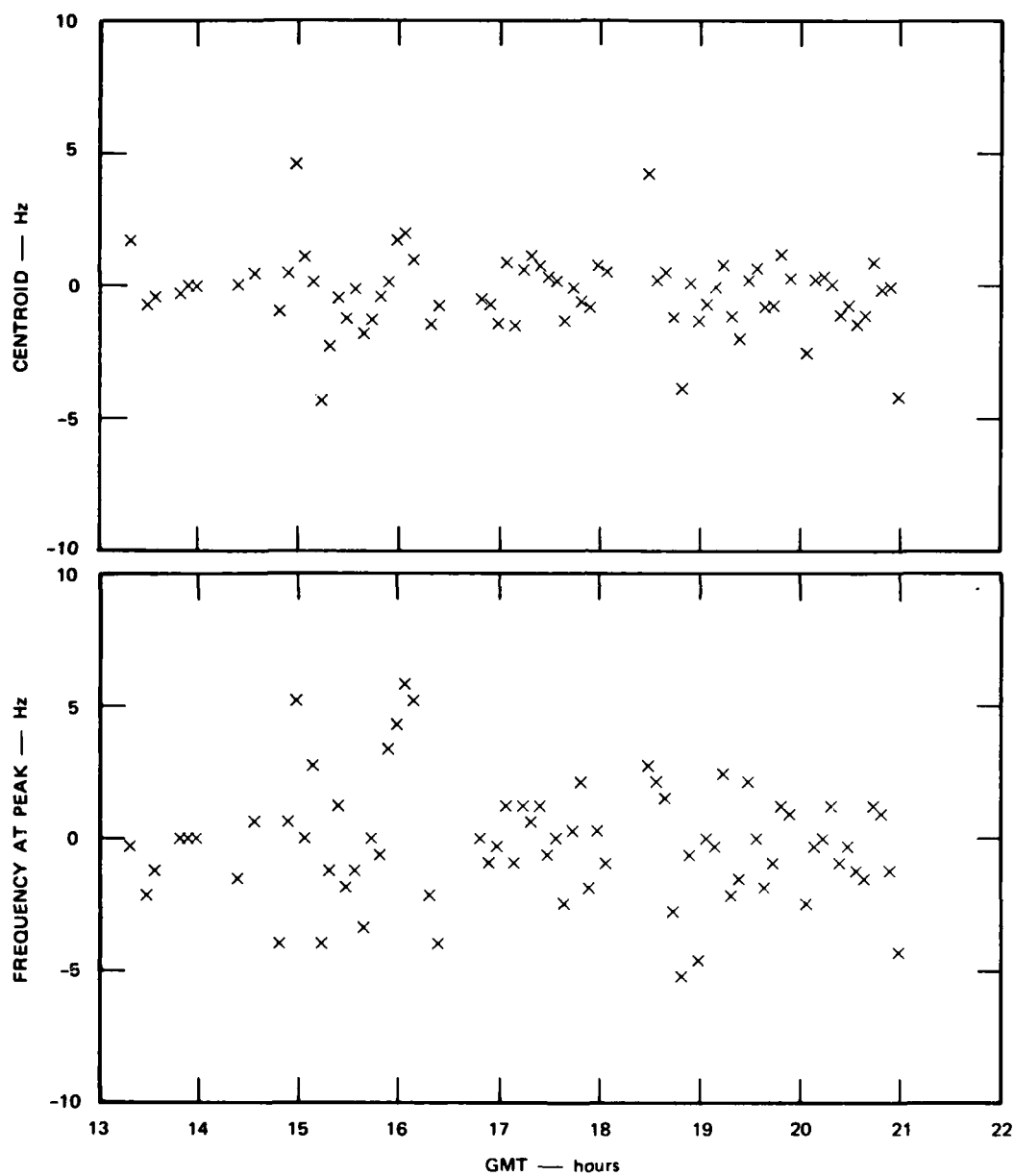


Figure 34. Doppler frequency of peak SNR and centroid (first moment) versus GMT on 3 October 1984 at 7.1-ms delay time.

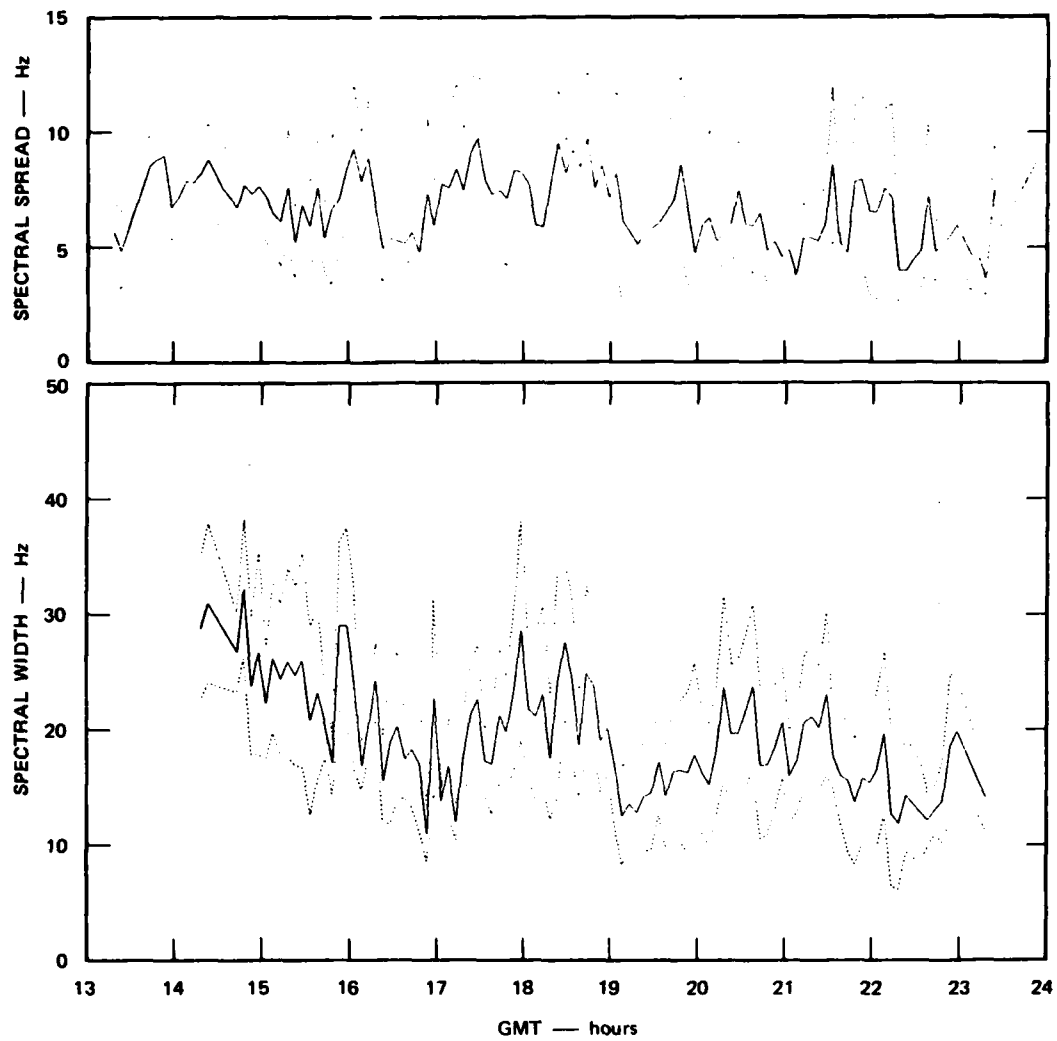


Figure 35. Mean and standard deviation of spectral width (20 dB down from peak) and spectral spread (second moment) versus GMT.

structured plasma breaking off from the dayside auroral zone. The strengths of the irregularities in these patches have been degraded by diffusion by the time they have been convected to the nightside of the polar cap [Kelley et al., 1982]. It should be noted that noon CMLT corresponds roughly to the start of the data in Figure 35 just after 1400 GMT (as shown previously in Figure 10).

To summarize the signal distortions that were observed in the Doppler domain, Figure 36 shows the spectral shape in the 7.1-ms range

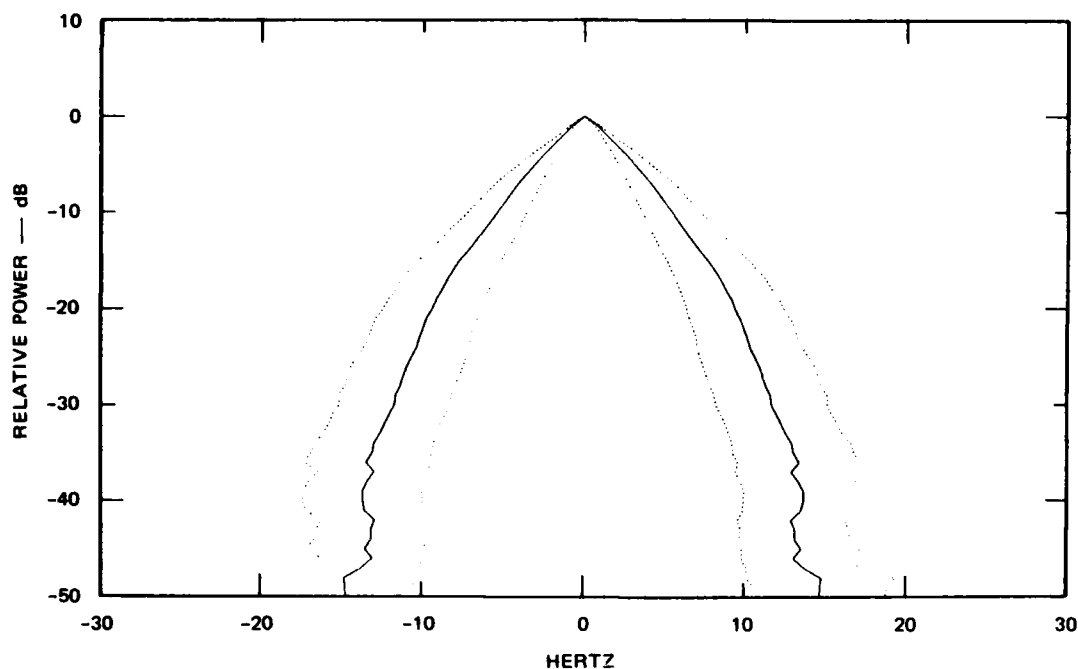


Figure 36. Average shape of the spectrum in the 7.1-ms range cell as defined by the mean and standard deviation of the spectral widths for all data.

cell as defined by all the data collected to date in this experiment that satisfied the criterion of a peak SNR >20 dB within ± 10 Hz. As before, the mean is drawn as a solid line, and the dotted lines show the standard deviation. A total of 1216 data points are averaged to define this curve down to -15 dB, but the number of points decreases sharply so that there are 1010 at -20 dB, 551 at -30 dB, 194 at -40 dB, and only 28

at -50 dB. The shape of this spectrum below about -35 dB is thus open to some question because of the small sample size, but it is also possible that the sample at large values of SNR may be inherently biased against large spectral spreads. In other words, the coherent integration needed to achieve an SNR of 40 dB or more may not be achievable with the transmitter power used under the conditions of strong scattering that lead to the large spectral spreads.

The spectral-shape data shown in Figure 36 for the 7.1-ms range cell are also available for other range cells. The significant information that has been extracted from this data base is presented in Figure 37, which shows how the width of the spectral density function

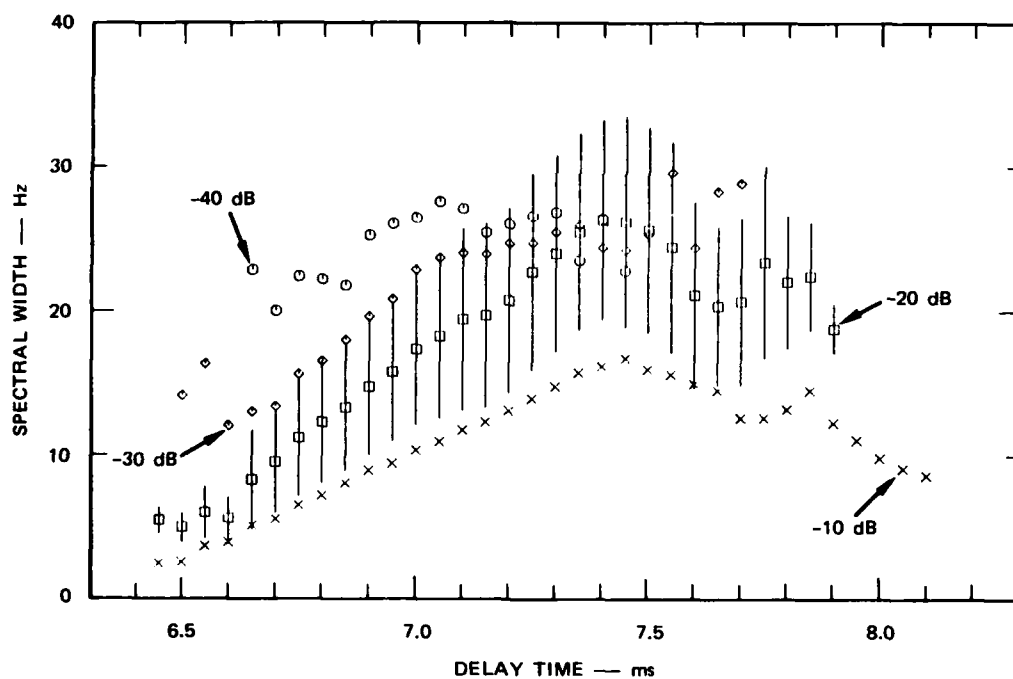


Figure 37. The dependence of spectral width on delay time.

varies as a function of delay time. To reduce the profusion of information on this graph, standard deviations are shown only for the 20-dB data points, and the points for the spectral width at -50 dB were

not plotted. The well-defined increase of spectral width with delay time from 6.45 ms (corresponding to E-layer modes for which $h' \sim 100$ km) to 7.45 ms (corresponding to high-ray F-layer modes with $h' = 507$ km) is possibly an effect of the degradation of irregularity strengths at lower altitudes below the F-layer peak. The fact that there is a break in the curve at 7.5 ms may be a result of the fact that high rays do not actually penetrate above the height of maximum ionization in the F layer. In fact, all high rays propagate for long distances at very nearly the same height near the peak of the electron density in the layer, although high rays with only infinitesimally different takeoff angles and true reflection heights have large differences in virtual height (delay time). A quantitative explanation of this variation of spectral width with delay time will need to be developed in terms of scattering theory as discussed in Section 7. The extent to which the decline of spread above 7.45 ms may be influenced by sample size is not known, but it is noted that for the -10-dB points there are 1006 samples at 7.5 ms, 542 at 7.7 ms, 126 at 7.9 ms, and only 19 at 8.1 ms.

As a final note, we point out that the spectral data presented here have been combined without any normalization with respect to operating frequency for the individual measurements. The likely frequency variation is addressed in Section 7. It is noted, however, that all PRN dwell frequencies were in the range from 6.520 MHz to 13.940 MHz, and very few dwells were below about 8.5 MHz.

6.7 Substorms

Characterizing transient ionospheric effects is important for HF communications systems, particularly for systems that use adaptive frequency management. Ionospheric substorms are the most dramatic transient auroral phenomena that effect HF propagation at high latitudes. The manifestations of auroral substorms include abrupt changes in the convection patterns and intensification of precipitating energetic particles. The response of the ionospheric F region to these

events is only beginning to be understood [Weber et al., 1984; de la Beaujardière, 1985].

Throughout the Greenland measurement campaigns, rapid changes in mean Doppler shift of the signal were observed. In Sections 6.4 and 6.5, we described moving blobs and acoustic-gravity waves as two sources of transient effects on HF signals. In this section, we describe a dramatic transient effect that we have associated with polar substorm activity.

Figure 38 shows the ionogram and subsequent CW data at 10.765 MHz for a late-afternoon measurement during the March 1985 campaign. Aside from an extension of the nose, the ionogram exhibits the form expected for a simple layer. The CW record shows a moderate level of disturbance that takes the form of pulsations of the spectral spread between about ± 10 Hz and ± 20 or 30 Hz with a period on the order of 10 s. However, near 2158 GMT, the Doppler spread shows a distinct increase up to about ± 35 or 40 Hz. This change is also reflected in the PRN-dwell data as can be seen by comparing the dwells at 2148 GMT and 2158 GMT shown in Figure 39.

As a continuation of this record, Figure 40 shows the ionogram and the subsequent CW data for the next 15-min period. It can be seen in this figure that the ionogram shows substantial range spreads, and the CW data show large spreads that persist until about 2108 GMT when the CW signal breaks up and is ultimately lost.

As a further continuation of the record, Figure 41 shows the ionogram and CW data for the next 15-min period. From the ionogram, it can be seen that the ionosphere no longer supported propagation at the previous dwell frequency of 10.765 MHz, so it was necessary to move lower in frequency to 8.960 MHz to continue the CW and PRN dwell observations.

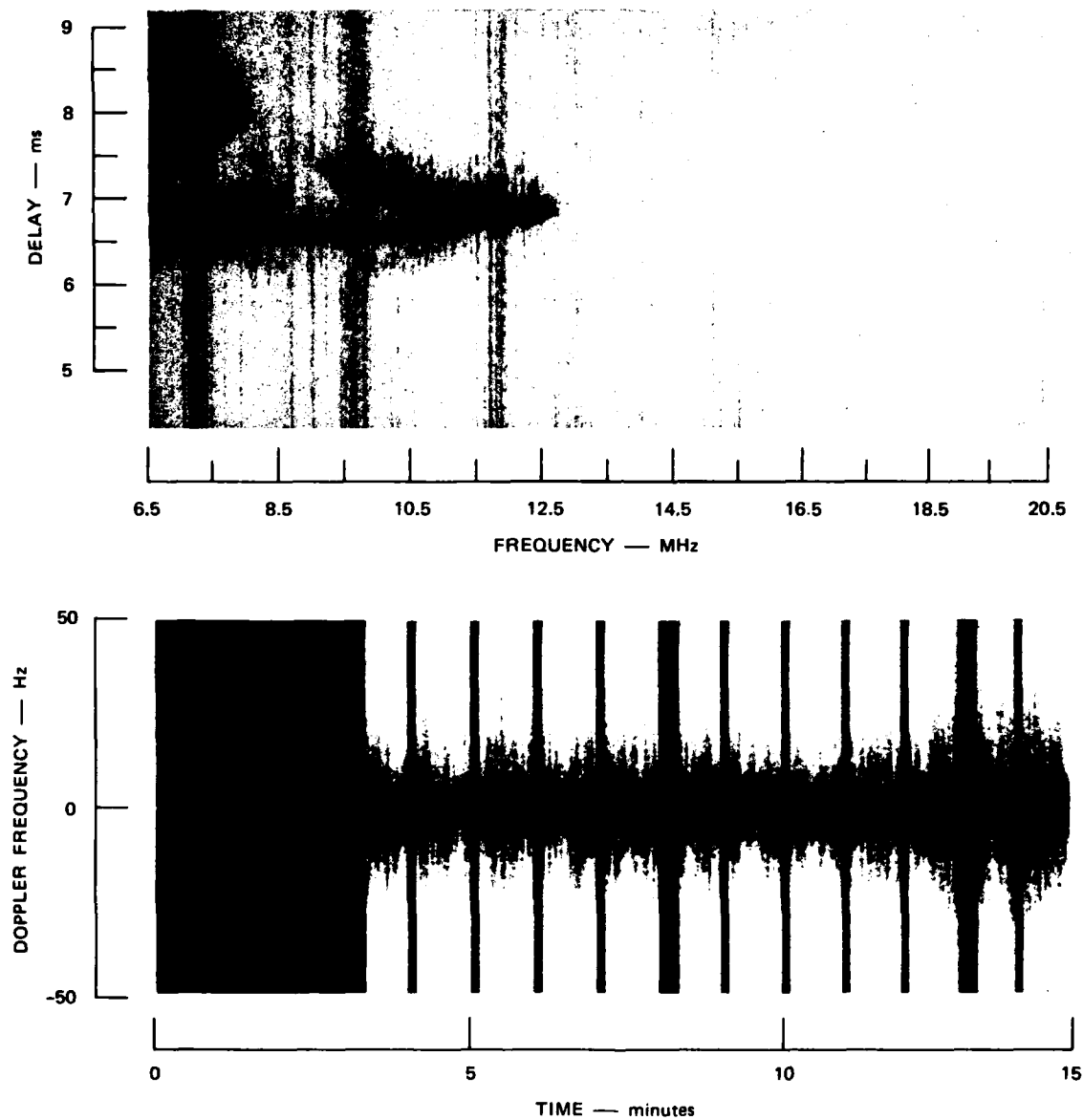


Figure 38. Ionogram and CW data recorded at 10.765 MHz in a 15-min sequence starting at 2145 GMT on 26 March 1985.

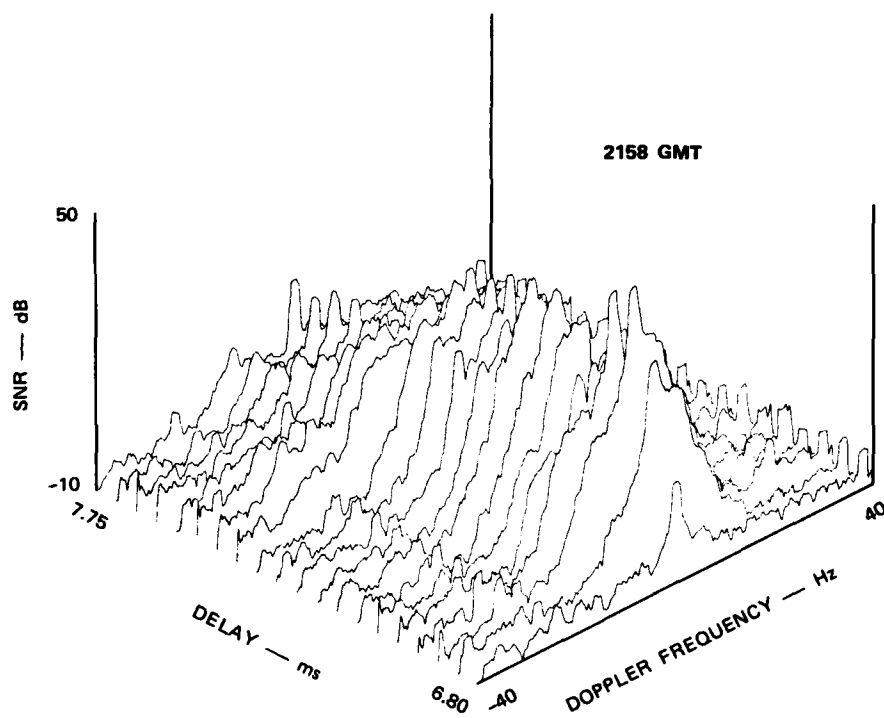
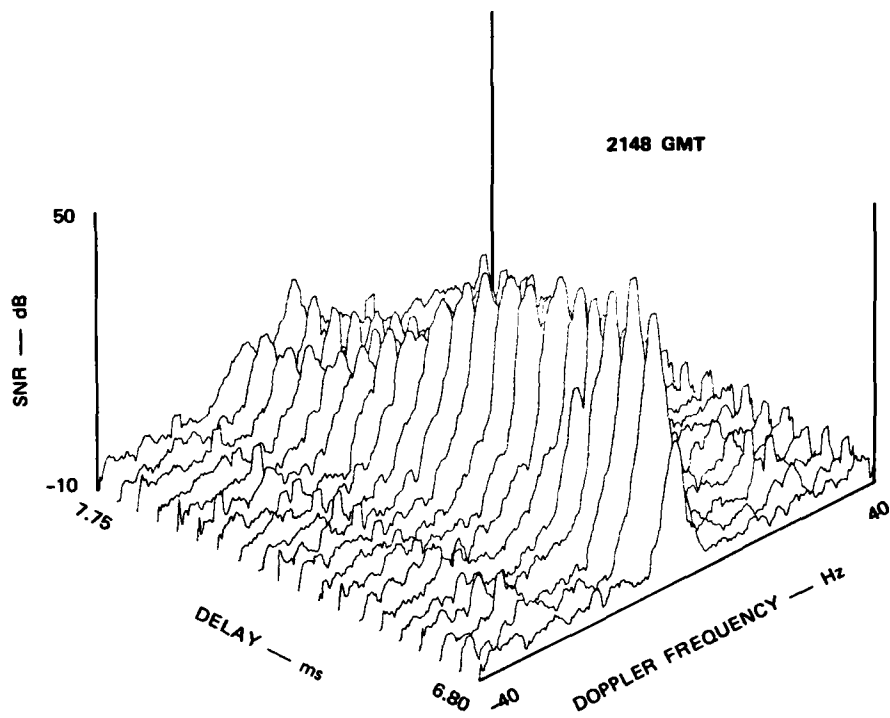


Figure 39. PRN dwell recorded at 10.765 MHz on 26 March 1985.

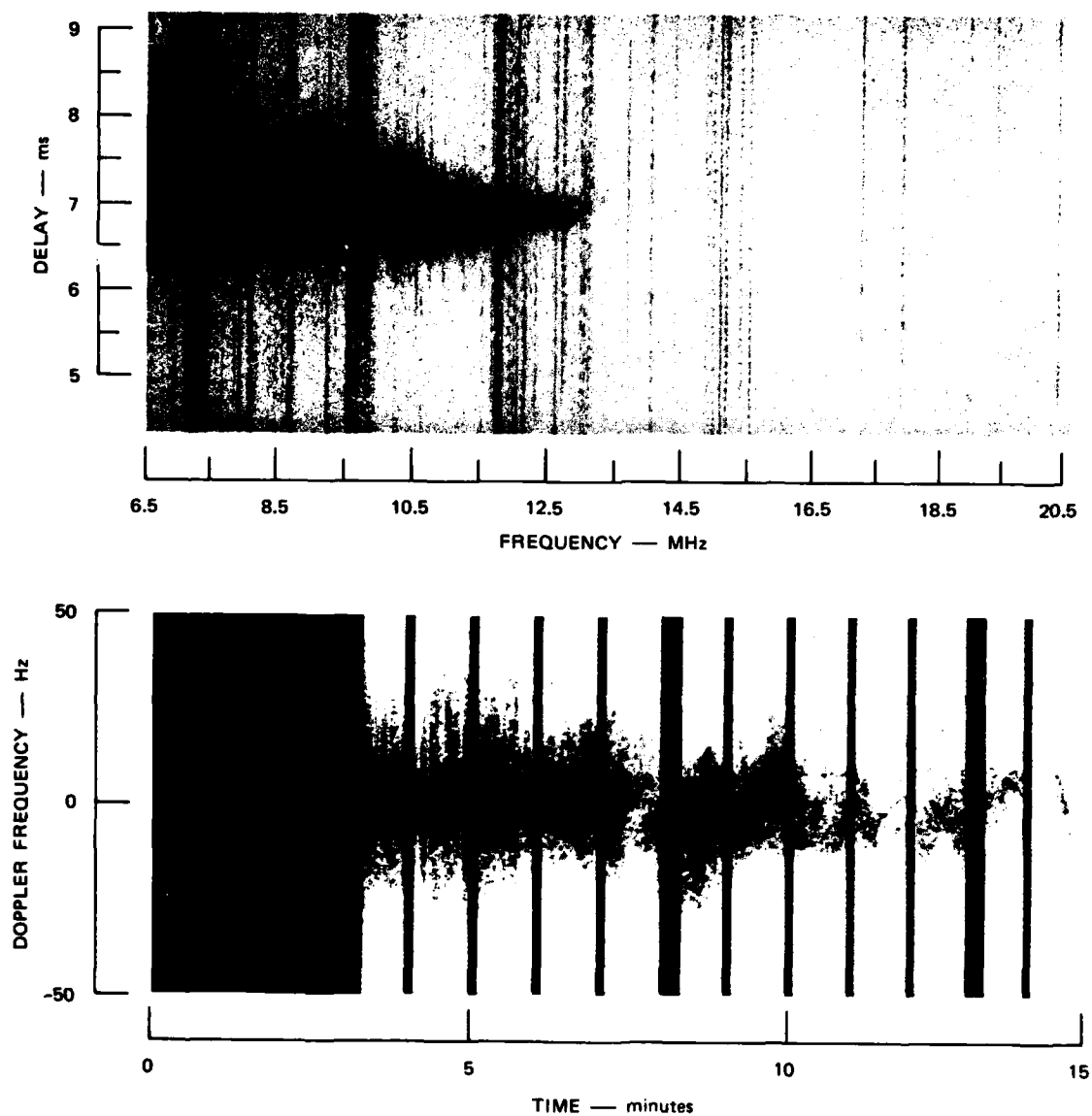


Figure 40. Ionogram and CW data recorded at 10.765 MHz in a 15-min sequence starting at 2200 GMT on 26 March 1985.

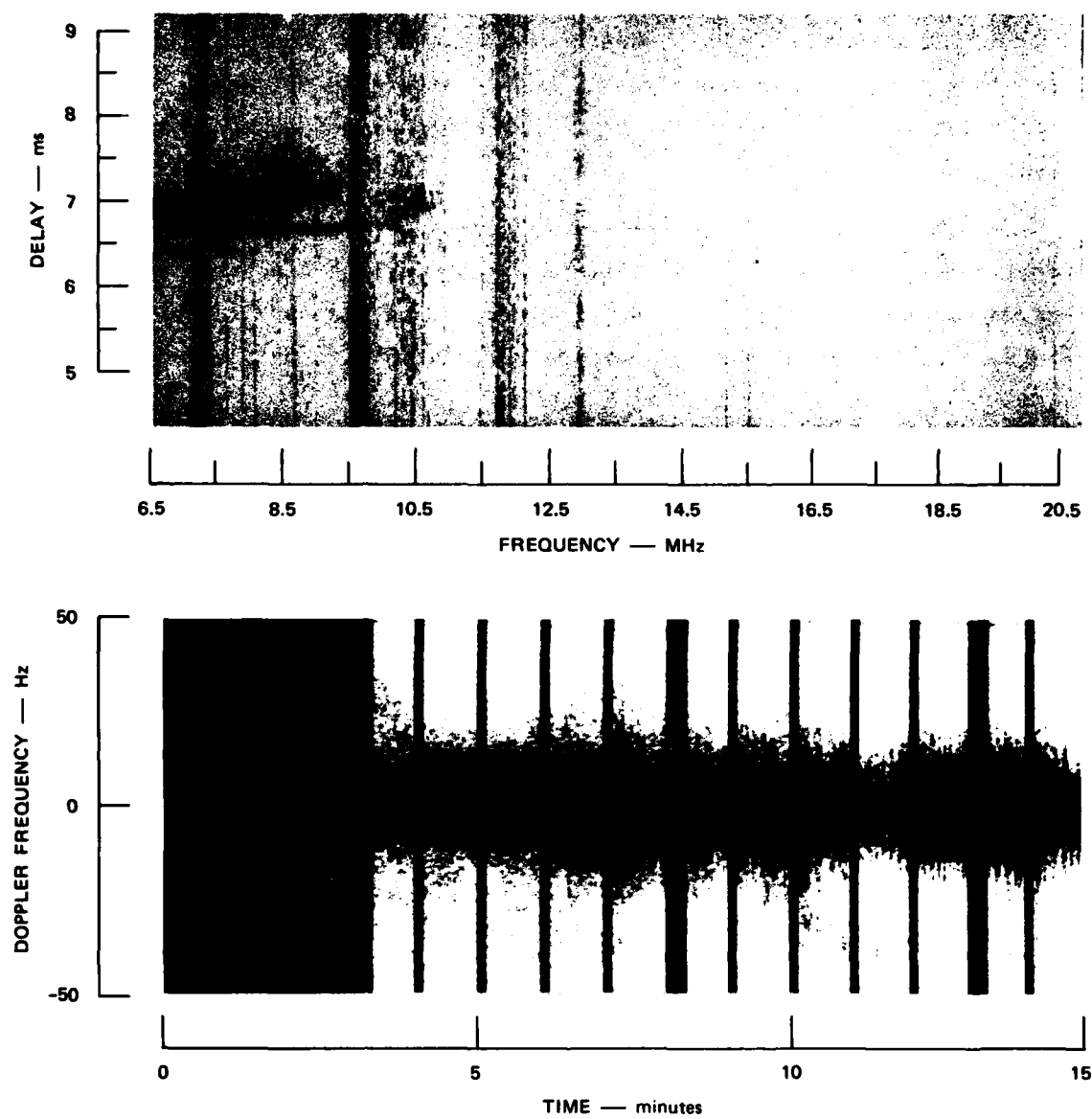
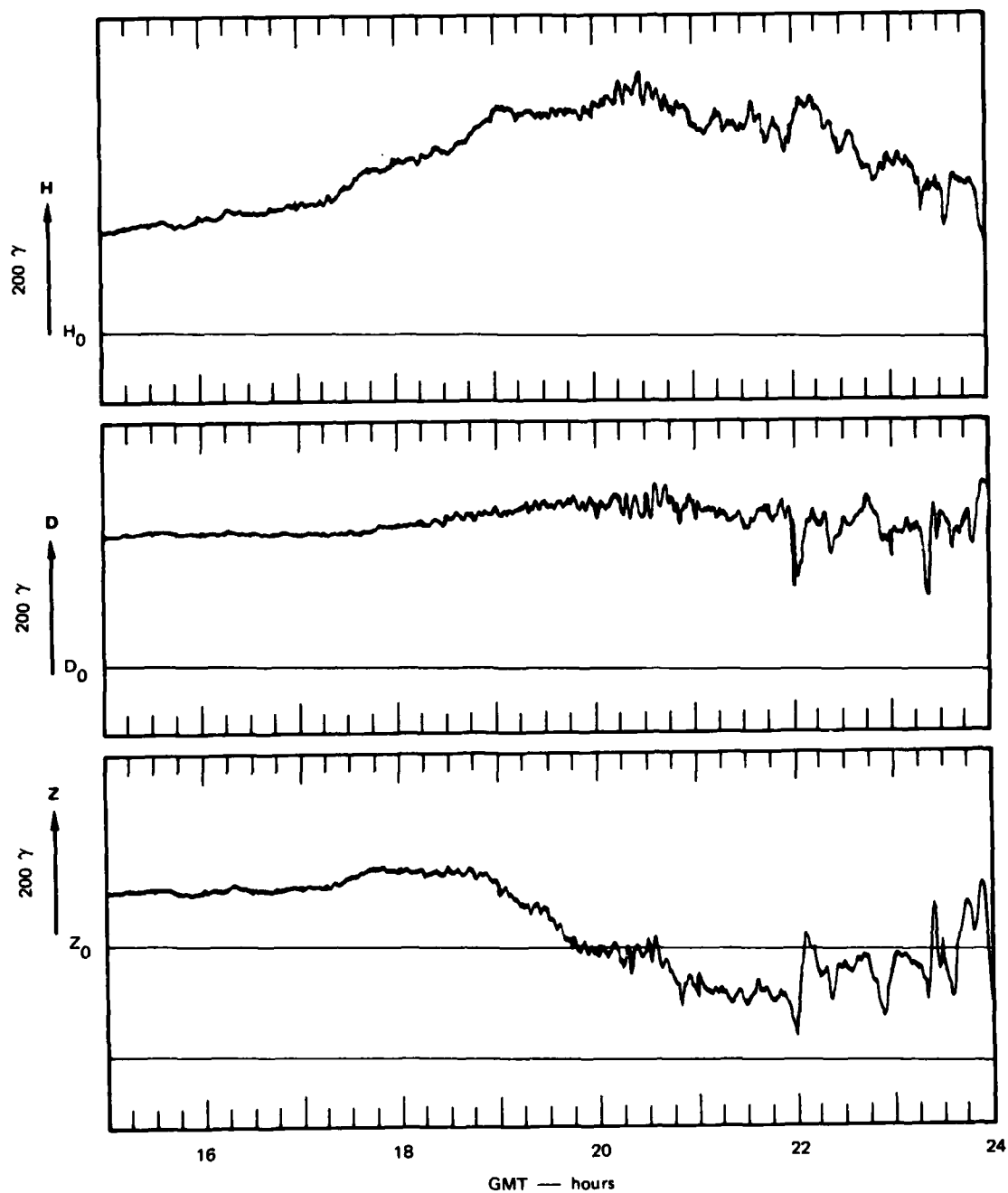


Figure 41. Ionogram and CW data recorded at 8.960 MHz in a 15-min sequence starting at 2215 GMT on 26 March 1985.

The magnetogram record for this same period obtained from the DMI Narssarssuaq observatory is shown in Figure 42. The positive bay in the H trace throughout the data taking period indicates a fairly high level of activity; however, the abrupt change in the H, D, and Z traces at 2200 GMT is possibly a small substorm onset that can be viewed as a secondary perturbation superimposed on the already disturbed ionosphere. This event is coincident with the abrupt change in the propagation conditions.

We shall pursue a more detailed analysis of this event as we receive inputs from other observatories and complete the processing of the data. We have presented the preliminary results here to show the dramatic propagation changes that are associated with auroral activity.



[Courtesy of the Danish Meteorological Institute]

Figure 42. Narssarssuaq magnetogram for 26 March 1985.

SECTION 7

INTERPRETATION IN TERMS OF SCATTER EFFECTS

7.1 Theory

Work was begun on developing a model of forward-scatter effects at HF at about the same time that preliminary planning was begun on the HF scatter experiment. The scatter model combines the work by Flatté et al., [1979], extending forward-scatter theory to refracted ray paths, with the model developed jointly under DNA sponsorship by various groups to describe forward-scatter effects on transionospheric ray paths at higher frequencies [Wittwer, 1979; 1982]. A detailed description of our HF model, essentially as used here, is also contained in Price [1985].

Relatively few quantities suffice to characterize a communications channel for most system-evaluation purposes. These include the delay and the Doppler spreads, which together characterize the extent of the standard channel scattering function, and the angular spread. Each of these quantities effectively describes the mean spread in the indicated parameter. Thus, the delay spread describes the spread in mean time delay of a transmitted pulse, while the Doppler spread describes its spread in mean frequency. The angular spread describes the mean spread in propagation direction. Our model includes procedures for calculating each of these quantities.

The Doppler, or frequency, spread is related through a Fourier transform to the decorrelation in time. This relationship is the standard one between the power spectrum of a signal and its correlation function. This aspect of the channel behavior typically is characterized by the width of the Doppler spread at some nominal power level relative to that at the peak of the Doppler spectrum; the spectrum is assumed to have a standard functional form (e.g., Gaussian) dictated

by either theoretical or experimental results. Doppler spread arises physically from changes in the characteristics of the propagation path with time.

Similarly, delay spread is closely tied to decorrelation in frequency; these two quantities again are related by a Fourier-transform pair. The coherence-bandwidth parameter typically is employed to characterize this aspect of the channel behavior. This parameter specifies the frequency separation necessary to decorrelate the signal to some nominal degree. To relate this parameter to delay spread, the frequency-correlation function again must be assumed to be of some standard form, dictated by either theoretical or experimental results. Physically, delay spread results from what can be called "micromultipath" propagation, with different propagation delays on the various propagation paths that exist between transmitter and receiver. Micromultipath is an effect of the scattering process and is different from the multipath that results from the mode structure (E-layer and F-layer, high-ray/low-ray one-hop/two-hop, and the like) that is inherently associated with HF propagation in the ionosphere.

The angular spread is related to the correlation function that describes the spatial decorrelation of the signal. The angular spread of the signal is of obvious interest for systems using very narrow-beam antennas, whereas the rate at which the signal decorrelates spatially determines the minimum spacing between antennas needed to achieve spatial diversity. That these two signal characteristics are related becomes evident if we consider that an antenna must have a large aperture to achieve a narrow beam width. The Fourier transforms relating angular spread to spatial decorrelation involve the position and wave-number vectors of the propagating field as complementary variables, rather than time and frequency, and thus are potentially multidimensional.

In our evaluation of HF scatter effects, we first calculate the phase structure function. This function, here denoted $D(2,1)$, is formally defined [Flatté et al., 1979; Esswien and Flatté, 1981] to be

the mean-square difference in the signal-phase fluctuations (due to the random medium) observed at two points. This difference can be expressed in terms of the difference between integrals of the random refractive-index fluctuations of the propagation medium along the two rays, 1 and 2, joining the signal source to the observation points:

$$D(2,1) \cong \langle [k_1 \int_1 \delta\mu(r) ds_1 - k_2 \int_2 \delta\mu(r) ds_2]^2 \rangle . \quad (7.1)$$

Note that $\delta\mu$ is the departure of the refractive index from its equilibrium, unperturbed value in the absence of irregularities. The concept of the phase-structure function can be extended, as suggested in Eq. (7.1), to include paths that differ by virtue of a difference in signal frequency rather than (or in addition to) different receiver locations. Paths can also differ simply because they are sampled at different times, although they are identical spatially.

If the decorrelation of the refractive-index fluctuations along the path is sufficiently rapid and the spatial separation between paths laterally is not too great, as we expect normally to be the case at HF, calculation of the phase structure function can be reduced to evaluation of a single integral, taken along the mean ray path [Esswein and Flatté, 1981]. The mean path is here taken to be given by that through the ionosphere in the absence of any irregularities. With this simplification, Eq. (7.1) becomes

$$D(2,1) \cong \int_{\text{path}} d[r; \Delta(r)] ds . \quad (7.2)$$

The separation between the two paths appearing in Eq. (7.1) now is carried by the $\Delta(r)$ appearing within the integrand of Eq. (7.2). The

integral can be interpreted as summing the contributions to the phase structure function from a succession of thin phase screens.

Furthermore, the factor $d[r;\Delta]$ in Eq. (7.2) that describes the incremental contribution from each (infinitesimally thin) screen is formally identical to that arising in the simpler case of straight-line propagation through a succession of such screens. This situation has been addressed in previous DNA work [Rino, 1979] on the effects of ionospheric scatter on satellite systems operating at higher frequencies. The description of the irregularity environment developed in the course of this earlier work consequently is readily incorporated into the HF model at this juncture [Price, 1985] with the result

$$d[r;\Delta(r)] \cong G(r)C_{\delta\phi}^2 |y|^{\min(2\nu-1,2)} \quad (7.3)$$

In Eq. (7.3), G expresses the effects of the anisotropy of the ionospheric irregularities on the strength of the scatter; it is given by

$$G(r) = \frac{ab}{(AC-B^2/4)^{1/2} \cos\beta(r)} \quad (7.4)$$

where a and b are parameters defining the elongation of the irregularity decorrelation ellipse along its principal axes. Parameters A , B , and C describe the orientation of the decorrelation ellipse in the coordinate system most convenient for defining the ray path, whose local angle from horizontal at each point along it is the angle $\beta(r)$.

The parameter $C_{\delta\phi}$ in Eq. (7.3), describing the strength of the irregularities, is given to a good approximation by

$$C_{\delta\phi}^2 = \frac{\lambda^2 r_e^2 C_s}{2\pi} \left(\nu^2 - \frac{9}{2} \nu + \frac{11}{2} \right) \quad (7.5)$$

where C_s is the strength parameter in the definition of the irregularity spectrum, and ν is an the index describing the power-law variation of

irregularity strength with wavelength, as defined in Eq. (6.2).

Finally, the factor y in Eq. (7.3) relates the path displacement Δ to the decorrelation ellipse. It is given by

$$y^2 = \frac{C\Delta_\phi^2 - B\Delta_\phi\Delta_r + A\Delta_r^2}{AC - B^2/4} \quad (7.6)$$

where the Δ_ϕ and Δ_r are the components of the path displacement in the r and ϕ directions, respectively.

Under certain conditions, characterized by strong phase fluctuations and large diffraction effects, the phase-structure function is simply related to the mutual coherence function. We have assumed that these conditions, denoted the fully saturated regime by Flatté et al. [1979], prevail at HF. Under such conditions,

$$\langle \psi^*(2)\psi(1) \rangle = \exp[-D(2,1)/2] \quad (7.7)$$

The mutual coherence function in turn constitutes, as indicated in Eq. (7.7), the correlation between two samples of the received-signal envelope, $\psi(1)$ and $\psi(2)$. This function thus describes the decorrelation between these samples produced by the random fluctuations of the propagation medium.

Physical interpretation of the spatial decorrelation of the signal is straightforward. In Eq. (7.7), Path Indices 1 and 2 are simply taken to represent the two points (i.e., receiver locations) at which the signal is sampled in determining the correlation function. Note that the correlation integral implicitly is defined as being taken over the ensemble of random fluctuations of the medium with the ray paths held fixed, rather than over an ensemble of different receiver locations. As the separation between the receivers is increased, the two paths through the medium generally become more separated and the correlation between the refractive-index fluctuations on them decreases. The mean-square difference between the integrated phase fluctuations on the two paths

(i.e., in the magnitude of the phase-structure function) consequently increases. This in turn amounts, as can be seen in Eq. (7.7), to a reduction in the magnitude of the mutual coherence, or correlation, function for the signals received at the two locations.

As noted in conjunction with Eq. (7.1), samples of the signal taken at two different times also can be considered to be associated with two distinct propagation paths. The signal samples decorrelate in this case because the fluctuations of the propagation medium encountered along the ray path change with time. In our model, calculation of this correlation function is simplified by the assumption (sometimes referred to as "frozen" turbulence) that these changes result from the convection, or drift, of a fixed irregularity structure across the ray path. With this assumption, the variation with time of the irregularities encountered along the path is the same as that produced at a fixed time by shifting the path laterally in the appropriate direction (given by the direction of the irregularity drift) an amount proportional to the time separation of interest. The effects of such a spatial shift can, in turn, be calculated in essentially the same manner as is employed in evaluating the spatial correlation function to determine the dependence of the phase-structure function on the spatial separation between receivers.

Decorrelation in frequency can, in principle, result from path separations that accompany frequency separations as a consequence of the dependence of refraction on frequency. Our evaluation of the frequency coherence bandwidth at present, however, is based on analogy with higher frequencies, in which refraction is small and its effect on the coherence bandwidth consequently is negligible. Under these circumstances, coherence-bandwidth limits are dictated primarily by the excess delay (i.e., time spread) resulting from the angular spread of the signal. (The delay jitter associated with the fluctuation of the integrated electron density along the nominal ray path could also be significant at HF, however.) Angular spread implies scatter from irregularities located to one side of the nominal ray path; calculation

AD-A173 088

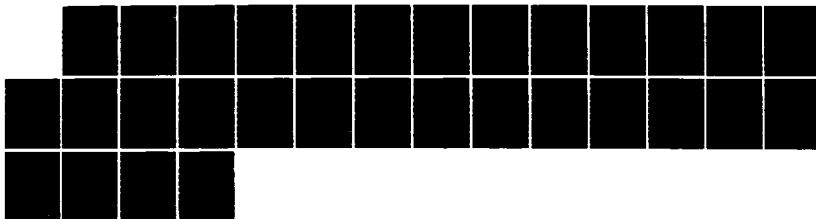
HF (HIGH-FREQUENCY) CHANNEL PROBE(U) SRI INTERNATIONAL
MENLO PARK CA R P BASLER ET AL. 31 MAY 85
DNA-TR-85-247 DNA001-83-C-0325

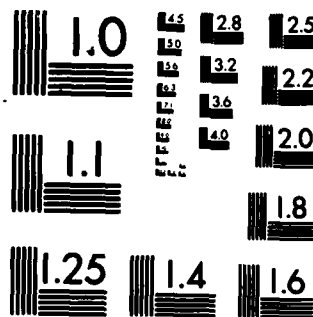
2/2

UNCLASSIFIED

F/G 20/14

NL





MICROCOPY RESOLUTION TEST CHART
NATIONAL BUREAU OF STANDARDS-1963-A

of the consequent excess delay is a matter of simple geometry. In this calculation, we have further assumed that scatter occurs predominately near the apex of the ray path. This assumption follows from our general assumption that the rms magnitude of the electron-density fluctuations in the ionosphere is everywhere proportional to the mean electron density.

For paths at mid and high latitudes, the excess-delay calculation is further simplified by the difference in magnitude between the angular spread vertically and horizontally. This difference is partially dictated by the constraints imposed on spread in the vertical plane by refraction. The anisotropy of the irregularity structures, combined with their orientation along the geomagnetic field, further enhances this disparity at high latitudes. Consequently, the vertical angular spread can to good approximation be ignored in the delay-spread calculations made here.

To calculate the phase-structure function, it is necessary to know the ray path along which the scatter-effects integration is to be made. At HF, determining the ray path can become just about as complicated as one wishes to make it. The complexity of the path calculation depends largely on that of the ionospheric model; vertically stratified ionospheres are simpler to deal with than ones that vary in two dimensions, and the latter are simpler than those that vary in three dimensions. Our preference is to keep the path determination as simple as possible within the context of the accuracy desired of the final result.

In the present work, we have assumed a vertically stratified ionospheric profile; furthermore, we have taken this profile to be one for which the ray-trace solution can be expressed analytically in closed form, namely a single spherically stratified quasi-parabolic layer with no magnetic field [Croft and Hoogasian, 1968]. The advantage of this formulation is that it allows us to find the ray path for given transmitter and receiver separation efficiently. It also gives exact analytic solutions that do not depend on the approximations necessary

for numerical ray tracing. With these solutions, we can express the lateral displacement of the path at some point along it analytically in terms of the displacement at the receiver [Price, 1985]. This displacement is needed in the calculation of the phase structure function for determining the spatial decorrelation of the signal.

The use of a single, quasi-parabolic layer is more speculative. In our application of the theory to make comparisons between calculated effects and relatively detailed measurements, a more elaborate ionospheric model may be needed to achieve the degree of agreement desired. However, the advantages provided by analytic ray-tracing need not be given up even if some elaboration should be necessary. Several quasi-parabolic layers can, for example, be superimposed to produce more general profiles; the ray path and related quantities remain analytically expressible for such profiles. In fact, multilayer profiles will be used in the follow-on analysis effort planned for this program.

7.2 Comparison of Theory and Data

The HF Channel Probe experiment was intended in part to provide a vehicle for evaluation of the HF scatter theory outlined above. To this end, the Channel Probe output is expressed largely in terms of the channel-scattering parameters. The channel-scattering function (range and Doppler spreads) is directly available online, as well as in refined form offline after further data processing. Additionally, the two spaced receiving antennas potentially could permit calculation of the signal spatial decorrelation at a lag corresponding to the antenna separation. We have not as yet, however, implemented the processing necessary to extract the spatial decorrelation from the PRN-dwell data (the CW data, for which this processing would be simpler, does not yield the mode-resolved scatter measurements that we need for comparison with the theoretical results).

The values adopted for the various parameters that define the irregularity environment are given in Table 1, they are based for the

most part on the data from the DNA HILAT satellite summarized in Section 6.3. Certain ancillary data also were collected during the course of our experiment. These data allow us to assess those features of the environment, such as the electron-density profile discussed in Section 5.2, for which the range of variation was expected to be substantial. Experimental characterization of such parameters is necessary if they are not to be given excessive free play in the comparison of theory with data. The objective generally has been to obtain the data necessary to define both the input to the scatter-effects calculations and the output expected from the calculations, given this input.

Table 1. Scatter-environment parameters.

Parameter	Value
Power-law index, ν	1.5
Outer scale, q_0	10^{-4} m^{-1}
$\langle \Delta N_e^2 \rangle / \langle N_e \rangle^2$	0.2
Field-line elongation, a	10

Also needed is a characterization of the velocity at which the irregularity structure is convected across the ray path. Electron-drift-velocity measurements made using the Sondre Stromfjord incoherent-scatter radar were employed to estimate this velocity. Examples of these measurements are shown in Figure 43 for a particular period that was chosen for purposes of making a detailed comparison of theory with data. In this figure, the component of the drift velocity in the direction of the radar beam is shown as the radar is scanned in azimuth at a constant elevation angle of 25° . The altitude probed by the radar is listed on the figure for the velocity measurements made in six different range cells. These altitudes are determined by the elevation angle of the radar beam and the range cell sampled. In fact, the drift

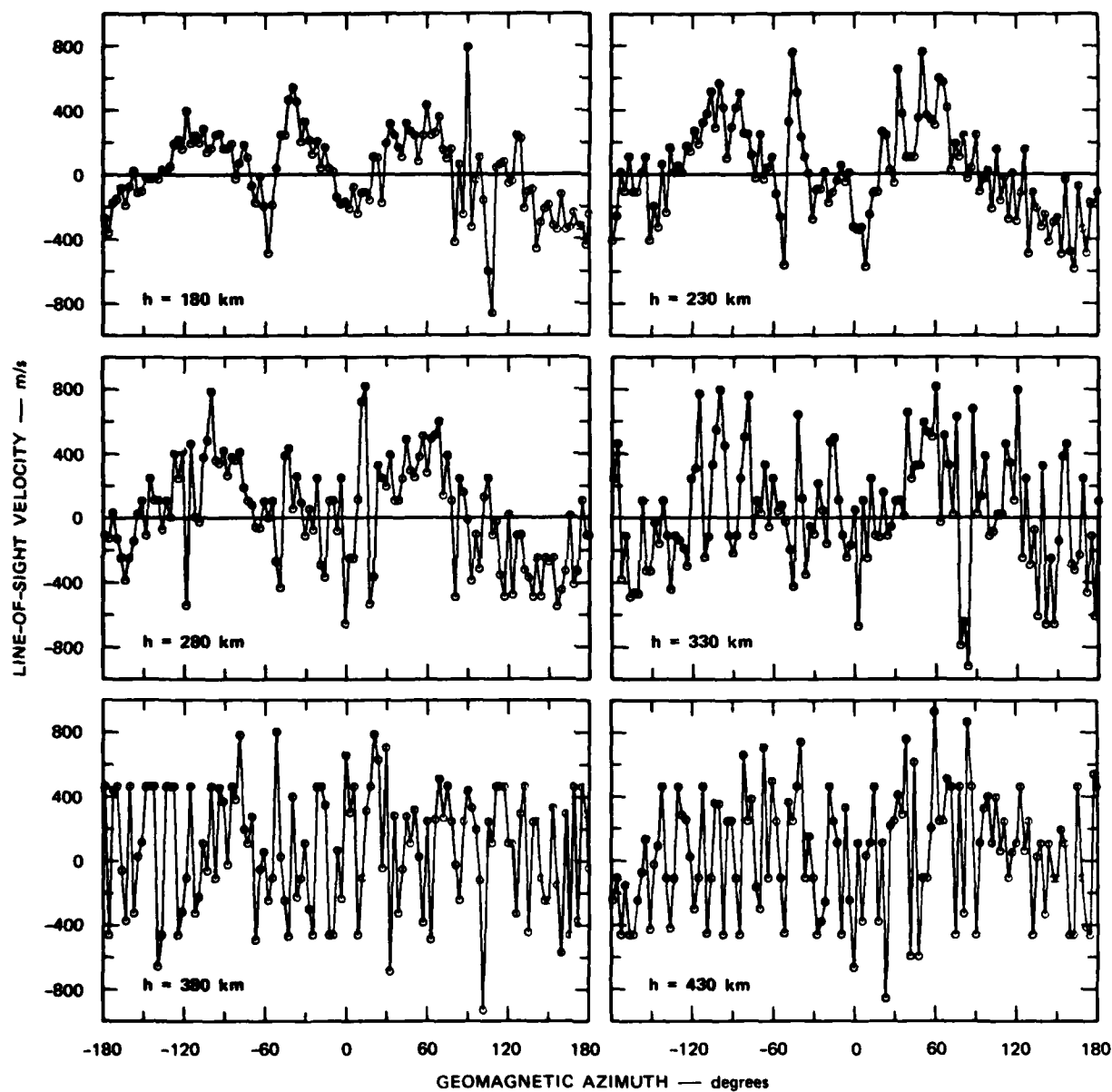


Figure 43. 360° velocity measurements in six range cells made by the incoherent-scatter radar at Sondre Stromfjord on 8 October 1984 from 1901:29 to 1911:29 GMT.

velocity generally can be assumed to map upward along the geomagnetic field lines, so these data should not be interpreted as showing the variation of velocity with altitude. Rather, they primarily show the horizontal variations in the velocity field. If the drift velocity were simply uniform over the entire region, the incoherent-scatter-radar measurements in each range cell would show a sinusoidal variation with azimuth. However, the data are not consistent with a simple uniform flow field. Nevertheless, from these data, we have concluded that a drift speed of 400 m/s, directed perpendicularly across the HF path, is a reasonable (although rough) estimate of the irregularity drift at the altitudes of interest.

Several factors were considered in selecting a set of data for purposes of comparing measurements with theory. First was the availability of diagnostic data from the incoherent-scatter radar at Sondre Stromfjord. (The radar was in operation only some of the time during the HF experiment.) Second was a clear separation in time delay between the high-ray and low-ray propagation modes. The scattering theory treats each mode independently, and we did not want in this example to deal with a case in which scattering effects cause the signal from the different modes to overlap in delay time. Third was a moderate degree of range and Doppler spreads. It was considered desirable initially to treat an intermediate case rather than one with either very narrow or very wide spreads.

The particular case chosen for comparison with theory was recorded at a frequency of 10.120 MHz at 1903 GMT on 8 October 1984. As is shown in Figure 44, a strong, well-isolated mode centered near 7.1 ms delay is evident in the PRN-dwell measurement. Both the delay and Doppler spreads exhibited by this F-layer low-ray mode are moderate when compared with the range of spreads observed during the overall course of the experiment as shown in Section 6.6. The similarity of the channel

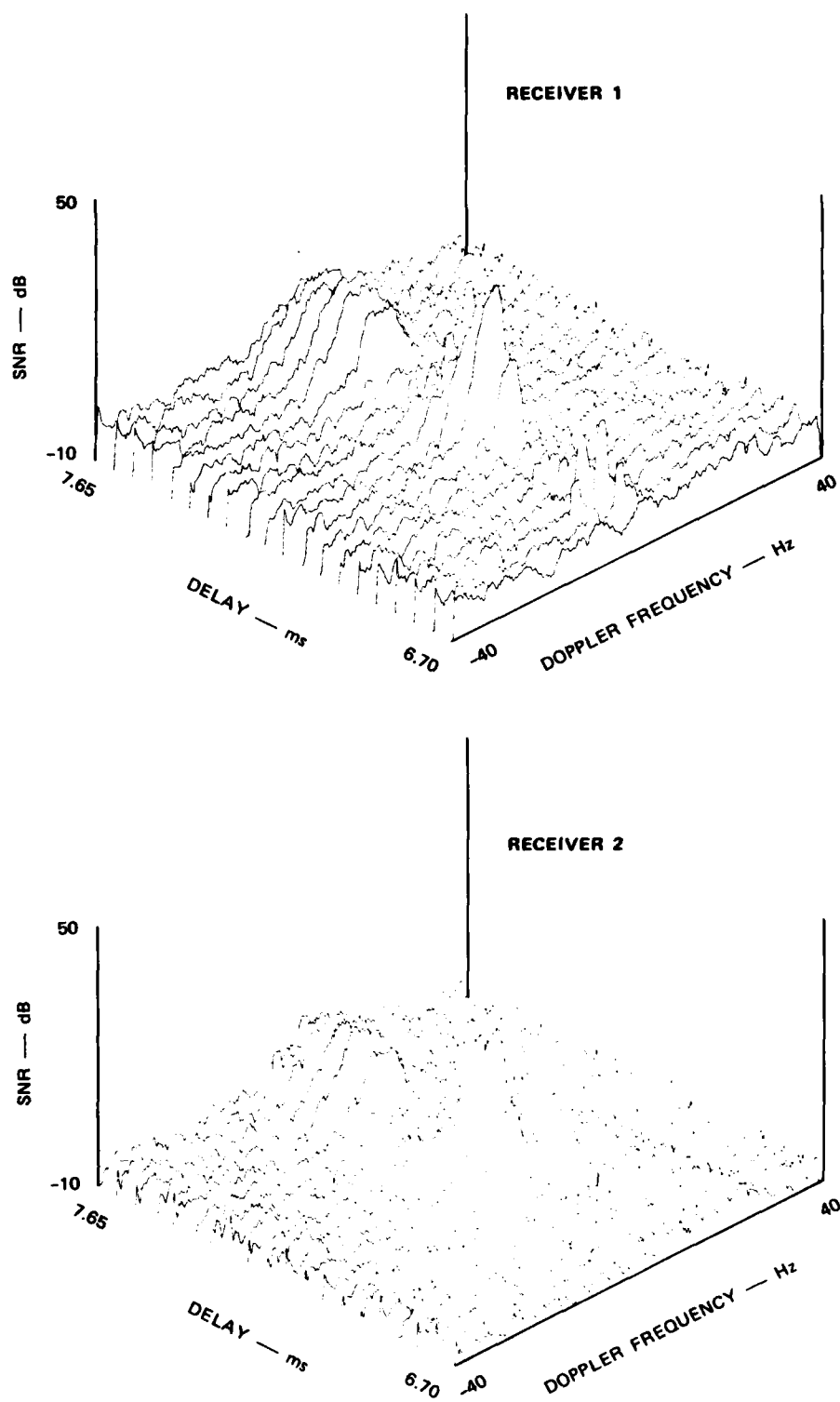


Figure 44. PRN dwell data recorded in the two HF channel probe receivers at 1903 GMT on 8 October 1984 at a frequency of 10.120 MHz.

scattering functions for the two antennas that are shown in this figure indicates that the spatial decorrelation over their separation distance of 61.3 m was small, suggesting that the angular spread was moderate as well.

The oblique ionogram taken on the path at 1901 GMT just before the PRN-dwell data shown in Figure 44 has been discussed in Section 5.2 and was shown previously in Figure 22. The ionogram confirms that the peak signal at a range of 7.1 ms is contained in the low-ray trace of the one-hop F-layer mode, and the signal centered near 7.5 ms in the PRN dwell corresponds to the high ray. The weaker, tightly confined mode centered near 6.8 ms can also be identified in the ionogram as that associated with what may be called the E-layer trace although 6.8 ms corresponds to a virtual height of 285 km.

To establish the nominal ray path to be used in the scatter-effects integrals, the vertical electron-density profile must first be determined. As has been described in Section 5.2, this profile has been obtained by analysis of the oblique ionogram, and a quasi-parabolic model has been defined to represent the electron-density profile, as discussed in Sections 5.3 and 5.4. This model profile is characterized by the height of the layer peak, the electron density at this peak, and the thickness of the layer. The values of these parameters found to give the best fit to the oblique ionogram are given in Figure 24, in which the experimental ionogram and the one synthesized using the model profile are compared.

The ray path determined by ray tracing through the model profile was assumed in the scatter-effects calculations to lie in the magnetic meridian plane, as is the case experimentally. The magnetic dip angle, taken to be constant over the entire path, was set equal to 80.43° , a value appropriate for the field at 350-km altitude above Sondre Stromfjord.

The dependence of the spatial correlation function on the direction of the path displacement can be characterized by an ellipse in the plane

perpendicular to the ray path at the receiver. For small displacements of the path, the path separation at points along the path is linearly related to that at the end of the path [Price, 1985]. In this case, our assumed value of 1.5 for the index of the irregularity spectrum (as given in Table 1), implies [according to Eqs. (7.2), (7.3), (7.6), and (7.7)] that the spatial and temporal correlation functions are Gaussian. For a Gaussian correlation function, this ellipse can most naturally be taken to give the distance at which the correlation has decreased to $1/e$. Because the path happens to lie in the magnetic meridian plane, the principle axes of the ellipse lie in (\parallel) and transverse to (\perp) the meridian plane containing the ray path. Given that the form of the spatial correlation function is known (Gaussian), its value needs be calculated for only a single, arbitrary displacement to determine its characteristic scale, i.e., the $1/e$ distance. Performing this calculation using Eqs. (7.2) and (7.7) yields the results given in Table 2 for the $1/e$ distances, Δ^e , along the two principle axes of the correlation ellipse and for the other, related quantities, discussed below.

Table 2. Spatial correlation characteristics.

Parameter	Value	
	\perp	\parallel
Δ^e	112 m	1465 m
δ^e	4.8°	0.4°
τ^e	23 μ s	-

The Gaussian form of the spatial correlation function also allows it to be Fourier transformed easily to obtain the distribution of the wave-number vector, and consequently the angular spread, δ , about the nominal ray path. If we write the correlation function, given by Eq. (7.7), along each of the principle axes as

$$R(\Delta_{\parallel, \perp}) = \exp[-(\Delta_{\parallel, \perp}/\Delta_{\parallel, \perp}^e)^2] \quad (7.8)$$

Fourier transformation yields

$$P(k_{\parallel, \perp}) = P_0 \exp[-(k_{\parallel, \perp}/k_{\parallel, \perp}^e)^2] \quad (7.9)$$

for the distribution of the transverse wave-number components k_{\parallel} and k_{\perp} in the planes containing the ray path and each of the principle axes of the correlation ellipse. The constant P_0 gives the magnitude of the distribution function for k directed along the path direction. The $1/e$ points k_{\parallel}^e and k_{\perp}^e on the distributions of k_{\parallel} and k_{\perp} are given by

$$k_{\parallel, \perp}^e = 2/\Delta_{\parallel, \perp}^e \quad (7.10)$$

The angular spread is characterized in Table 7.2 by the angles δ_{\parallel}^e and δ_{\perp}^e between the wave number vector that corresponds to each of these $1/e$ points and the nominal path direction. These angles are found using simple trigonometry, with the result

$$\delta_{\parallel, \perp}^e = \arcsin(c/\pi f \Delta_{\parallel, \perp}^e) \quad ; \quad (7.11a)$$

or,

$$\delta_{\parallel, \perp}^e \cong c/\pi f \Delta_{\parallel, \perp}^e \quad , \quad (7.11b)$$

where the magnitude of k is $2\pi f/c$, c is the speed of light, and f is the signal frequency. The approximation given by Eq. (7.11b) for angles that are not too large is expected to be adequate under most circumstances. It implies that the angular distribution in δ is approximately Gaussian as well.

As expected, given the elongation of the irregularities along the magnetic field and the orientation of this field, the angular spreads shown in Table 2 are much greater horizontally than vertically. The results also appear qualitatively to be consistent with the experimental data given in Figure 44. This figure shows a high degree of correlation between the signals recorded on the two receiving antennas, which at 61.3-m separation are about a factor of two closer together than the Δ_1^e 1/e decorrelation length for horizontal displacements given in the table. Quantitative comparison of these model results with experimental data must, however, await our extraction of correlation values from the spaced-receiver data.

The angular spreads have also been used, as is described in Section 7.1, to calculate the delay spread of the signal. This spread is shown in the last row of Table 2 as τ^e . In this calculation, we have simply determined, for a planar geometry, the excess path length and consequent excess delay implied by the lateral offset at midpath that corresponds to the horizontal 1/e angle δ^e shown in the table. This angle is given by

$$\tau^e = \frac{D}{c} \left[(1 + \tan^2 \delta^e)^{1/2} - 1 \right] ; \quad (7.12a)$$

or,

$$\tau^e \approx \frac{D}{2c} (\delta^e)^2 \quad (7.12b)$$

where D is the path length. The approximation for small angles given by Eq. (7.12b) again serves adequately in most cases.

The PRN-dwell data presented in Figure 44 appears to indicate a substantially larger delay spread for the low-ray mode centered near 7.1 ms than is given in Table 2. Closer examination of the experimental data, however, reveals the cause of this discrepancy. When the PRN-dwell data are replotted in contour form as shown in Figure 45, this mode is seen actually to be split into two components. This split is probably the result of off-path reflection from a discrete blob of ionization, as discussed in Section 6.4.

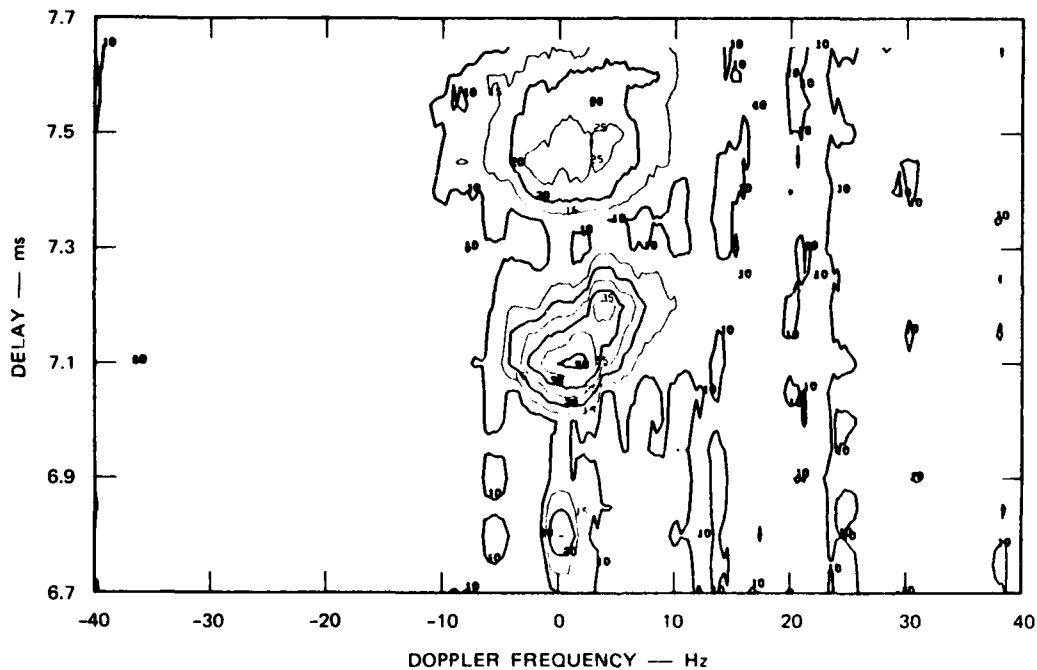


Figure 45. Contour plot of the Receiver 1 data from Figure 44.

A constant-Doppler cut at 2 Hz through the peak of the scattering function of Figure 45 yields the delay-spread curve shown in Figure 46. Also shown is the delay spread derived from our model. To determine this spread, we assume that the angular-spectrum components are uncorrelated and, as outlined in Section 7.1, add the scattered energy corresponding to each angular component with an appropriate delay. If

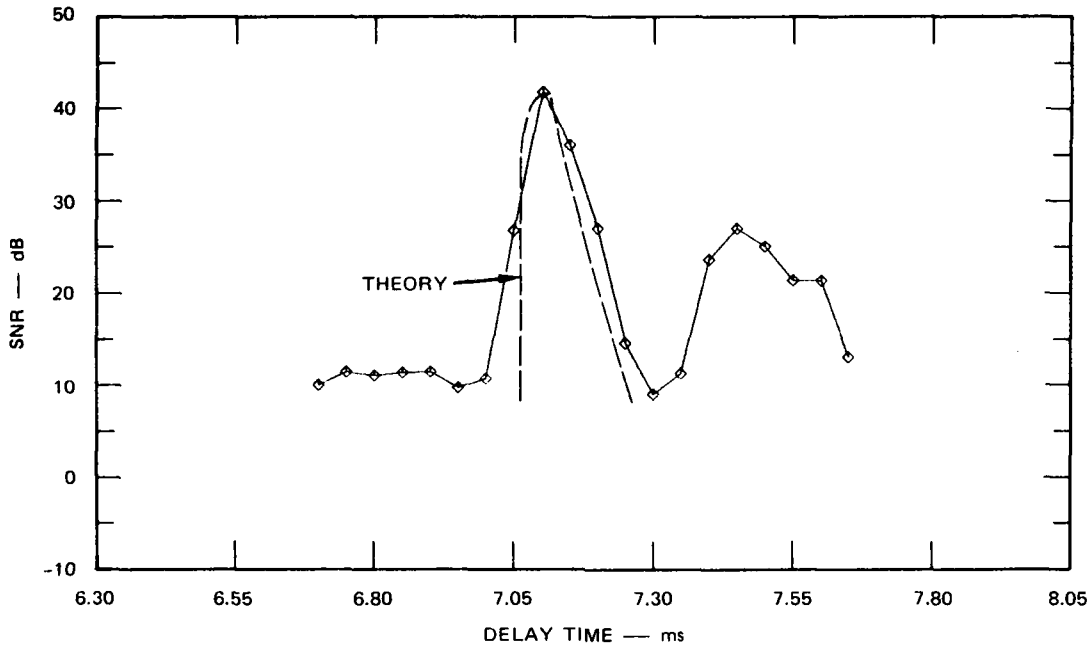


Figure 46. SNR versus delay time at a Doppler frequency of 2 Hz for the data shown in Figure 45.

we assume that the temporal form of each angular component, denoted by $\varepsilon_o(\tau)$, is the same, the resultant power, $\varepsilon(\tau)$, can be written as an integral over contributions beginning at different times; i.e.,

$$\varepsilon(\tau) = \int_{-\infty}^{\tau} d\tau' \varepsilon_o(\tau - \tau') p(\tau') \quad (7.13)$$

where $p(\tau)$ is the strength of the contribution beginning at τ . If the time origin in Eq. (7.13) is taken to be that of the earliest arrival over the unscattered ray path, then $p(\tau) = 0$ for $\tau < 0$ in order that causality not be violated. With this constraint, Eq. (7.13) becomes

$$\varepsilon(\tau) = \begin{cases} \int_0^{\tau} d\tau' \varepsilon_o(\tau - \tau') p(\tau') & , \quad 0 \leq \tau \\ 0 & , \quad \tau < 0 \end{cases} \quad (7.14a)$$

$$(7.14b)$$

If we neglect the Doppler spread, which is small compared to the 20-kHz bandwidth of the PRN signal, $\varepsilon_o(\tau)$ can be taken to have the undistorted form this signal takes on once it has been processed through the appropriate correlation filter, that is, a rectangular pulse of duration τ_o . With this simplification, Eq. (7.13) becomes

$$\varepsilon(\tau) = \begin{cases} \int_0^{\tau} d\tau' p(\tau') & , & 0 \leq \tau & ; & (7.15a) \\ \max(0, \tau - \tau_o) & & & & \\ 0 & , & \tau < 0 & . & (7.15b) \end{cases}$$

Finally, the energy distribution in τ can be replaced by its corresponding distribution in k_ϕ using

$$p(\tau)d\tau = p(k_\phi) dk_\phi , \quad (7.16)$$

yielding

$$\varepsilon(\tau) = \begin{cases} k_\phi(\tau) & , & 0 \leq \tau & ; & (7.17a) \\ \int_0^{\tau} dk_\phi p(k_\phi) & & & & \\ \max[0, k_\phi(\tau - \tau_o)] & & & & \\ 0, & , & \tau < 0 & . & (7.17b) \end{cases}$$

The form of $p(k_\phi)$ is Gaussian, Eq. (7.9), so that we finally have

$$\varepsilon(\tau) = \begin{cases} k_\phi(\tau) & , & 0 \leq \tau & ; & (7.18a) \\ \int_0^{\tau} dk_\phi \exp[-(k_\phi/k_\phi^e)^2] & & & & \\ \max[0, k_\phi(\tau - \tau_o)] & & & & \\ 0, & , & \tau < 0 & . & (7.18b) \end{cases}$$

The integral in Eq. (7.18a) can be recognized as the error function, or more precisely the difference between a pair of them. For $\tau < \tau_o$, the

error function corresponding to the lower limit in Eq. (7.18a) is zero; in terms of these functions Eq. (7.18a) becomes

$$\varepsilon(\tau) = \begin{cases} 0, & \tau \leq 0 & ; (7.19a) \\ k_{\phi}^e p_o \operatorname{erf}[k_{\phi}(\tau)/k_{\phi}^e], & 0 \leq \tau \leq \tau_o & ; (7.19b) \\ k_{\phi}^e p_o \{ \operatorname{erf}[k_{\phi}(\tau)/k_{\phi}^e] - \operatorname{erf}[k_{\phi}(\tau - \tau_o)/k_{\phi}^e] \}, & \tau_o \leq \tau & ; (7.19c) \end{cases}$$

where

$$k_{\phi}(\tau) = k[c\tau(2D + c\tau)]^{1/2}/(D + c\tau) \quad (7.20)$$

follows from Eqs. (7.11a) and (7.12a).

Eqs. (7.19) and (7.20) were used with a value for τ_o of 50 μ s, corresponding to the 20-kHz signal bandwidth, to calculate the theoretical curve shown in Figure 46. As can be seen from comparison of this curve with the experimental data, this model does a good job of reproducing the observed spread following the signal peak. The calculated onset is, however, much sharper than that observed experimentally. Thus, the angular spread appears to account well for the form of the signal decay, but not the smearing observed in the signal rise.

Cuts at constant delay through the peaks of the experimentally measured channel-scattering functions presented in Figures 44 and 45 yield the Doppler spectra shown in Figure 47 for the low-ray and high-ray modes centered respectively at 7.1 ms and 7.45 ms. Because the temporal decorrelation function produced by the theory is Gaussian for our value of the power-law index, so also is its Fourier transform, the Doppler spectrum. Calculation of this spectrum using formulas equivalent to Eqs. (7.8) and (7.10) yields the theoretical curves superimposed on the experimental data in Figure 47. The agreement

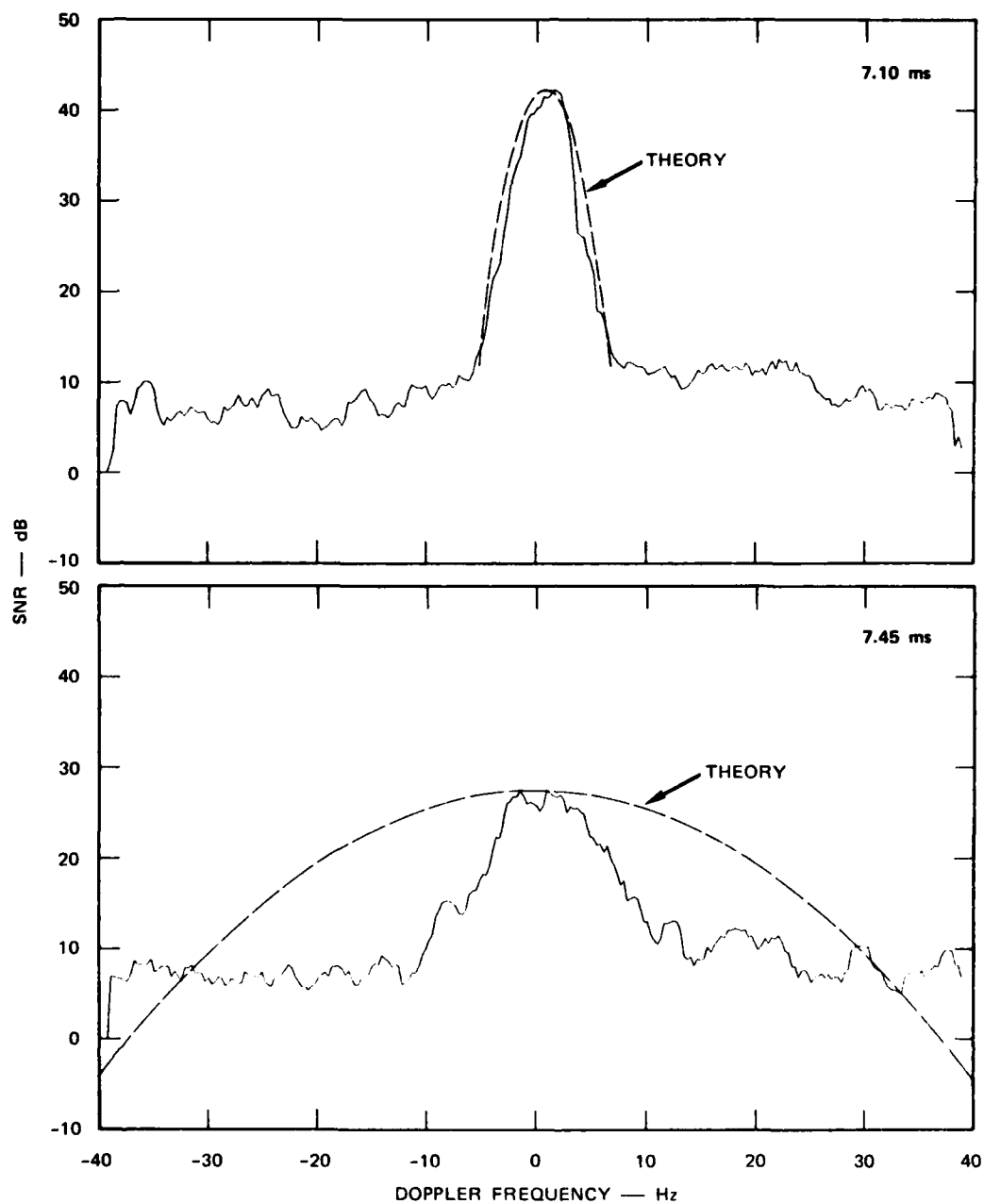


Figure 47. Comparison of theoretical and experimental SDF for two range cells from the PRN dwell data shown in Figure 44 for Receiver 1.

between experiment and theory is excellent for the low ray, but for the high ray the theoretical curve is spread much more than the experimental data, although both theory and data show that the high-ray spectrum is spread more than the low-ray spectrum.

The increase in calculated spectral spread for the high ray relative to the low ray results both from the greater penetration of the high ray into the ionosphere and from the flatter trajectory of the high ray near its apex. Although this increase of the theoretical high-ray spread relative to the low-ray spread is qualitatively consistent with the overall results of the experiment summarized previously in Figure 37, it is clear from Figure 47 that there is a quantitative discrepancy that must be resolved between theory and observation. It is possible that this discrepancy could be a result of the overspecialization of the path-integration algebra to conditions that are appropriate to the low ray but not the high ray. In particular, assumptions were made in overcoming some numerical difficulties associated with integrating the singularity that is encountered at the path apex. These assumptions may need to be generalized to apply to the high ray as well as to the low ray. This task will be part of the continuing effort on the program, as will calculating the high-ray delay spread.

The comparisons between the experimental data and the results of the model calculations presented here, although representing only one case, suggest that the theory is not hopelessly at odds with the data. Improving the theory to bring it into better agreement with the data will be a major part of the continuing program.

7.3 Sensitivity to Parameter Variations

Changes in the values of some model parameters lead simply to corresponding changes in the signal decorrelation and spread parameters. For example, the irregularity strength parameter C that appears in Eq. (7.5) is proportional to the electron-density variance [Price, 1985], which we take in turn to be proportional to the square of the mean electron density at each point along the ray path. Thus, the

linear dependence of $d[\vec{r}; \vec{\Delta}(\vec{r})]$ on C_s shown by Eqs. (7.3) and (7.5) implies that the calculated angular and Doppler spreads are proportional to the ratio of the rms electron-density fluctuation to the mean density. Similarly, the quadratic dependence of $d[\vec{r}; \vec{\Delta}(\vec{r})]$ on y for $\nu = 1.5$, Eq. (7.3), implies that the calculated Doppler spread is proportional to the electron drift speed across the path.

Changes in other parameters, such as the power-law index and outer scale of the irregularity spectrum, have effects that are less readily evident. These have not been explored in any detail in our work as yet. The effect of these parameters on scatter behavior at higher frequencies would, however, be expected to serve as a guide at HF as well, given the origins of our model. The consequences at HF of anisotropy in the irregularity structure, although made more complex in detail by the varying orientation of the ray path relative to this anisotropy, also can be anticipated from those at higher frequencies.

Experience at higher frequencies is apt to be a less reliable guide in anticipating the dependence of scatter effects on other parameters. Some parameters, such as the path length, have an entirely new significance at HF. The dependence on others, such as the signal frequency, is markedly changed from that found on transionospheric paths. These differences generally can be traced to the role played at HF by the ray path in determining the portion of the ionosphere sampled by the signal. Although a transionospheric line-of-sight path fundamentally plays the same role, it differs in practice by being insensitive to such parameter variations. At HF, changes in frequency or path length markedly affect how deeply the ray penetrates into the layer responsible for reflecting the signal, and consequently the exposure of the signal to the irregularities responsible for scatter effects.

This sensitivity to parameters affecting the location of the ray path in the ionosphere is well illustrated by the variation of width with signal frequency shown in Figure 48. The profile and parameter values employed in this calculation are those used previously in

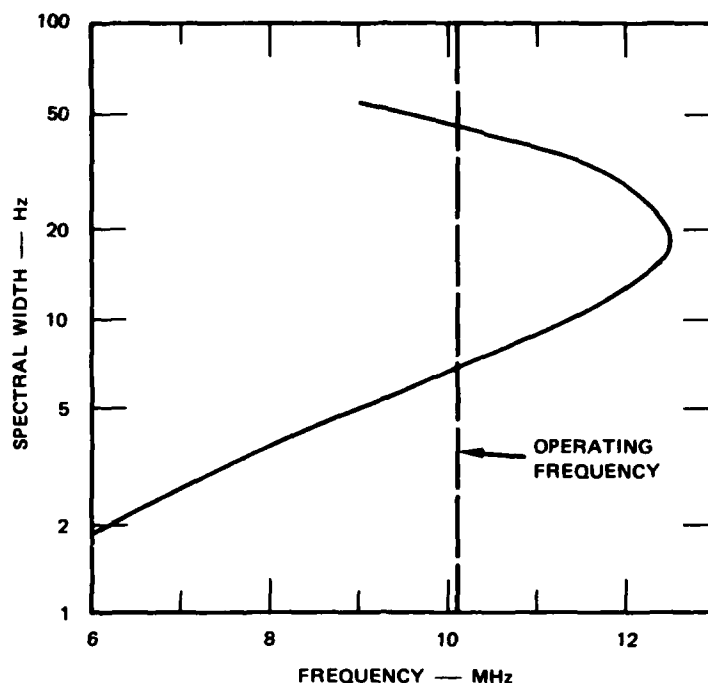


Figure 48. Frequency variation of spectral width (10 dB down from the peak)

Section 7.2, as summarized in Table 1 and Figure 24. The delay spread is seen in this example to increase with increasing frequency for the low ray and decrease with increasing frequency for the high ray.

Such behavior is typical of an HF path. Although the basic frequency dependence of scatter effects is for the effects to decrease with increasing frequency as the ratio of wavelength to irregularity scale decreases, the sense of the frequency dependence actually is reversed at HF for the low ray. To understand this behavior qualitatively, it is only necessary to examine the variation of the ray path with frequency. For a fixed path length, the takeoff angle of the low ray increases with increasing frequency. Thus, the low ray penetrates more deeply into the layer responsible for its reflection

with increasing frequency, with a consequent increase at the path apex of the fluctuations responsible for the scatter effects. This variation with frequency of the depth of penetration of the ray path into the layer is illustrated in Figure 48 for the electron-density profile used in these calculations. The ray also has a greater radius of curvature at its apex for higher frequencies, so that the path exits the region of strong fluctuations more slowly. Together, these two factors serve to increase strongly the magnitude of the scatter effects on the low ray as frequency increases.

For the high ray, on the other hand, the takeoff angle for a fixed path length decreases with increasing frequency. The consequent tendency for the apex height to decrease with increasing frequency is partially compensated by the reduction in rate of ray refraction that also accompanies increasing frequency. The net effect, however, is a slowly decreasing apex height with increasing frequency, as is shown in Figure 49. The larger ray curvature at the ray apex apparently is not sufficient to overcome the decrease in fluctuation strength that accompanies the decreasing height of the apex, and the overall effect is a decrease in the magnitude of the scatter effects as the frequency increases.

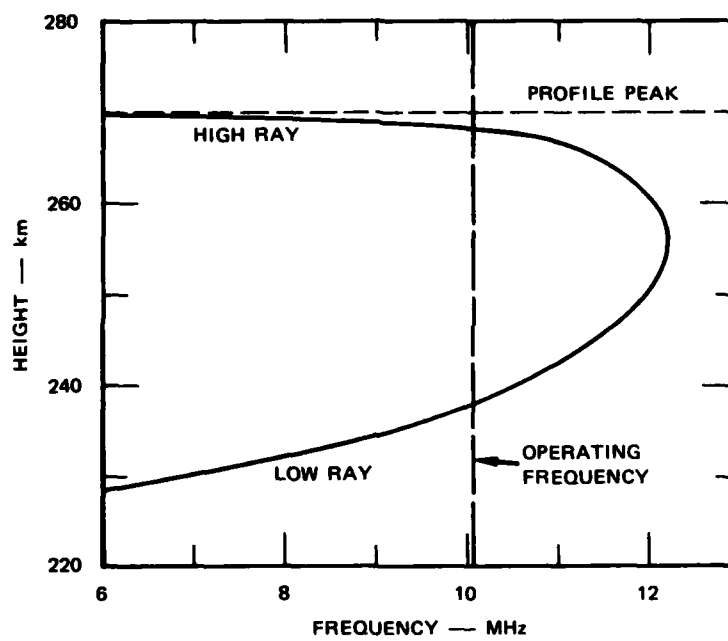


Figure 49. Variation of ray apex height with frequency.

SECTION 8

CONCLUSIONS

The HF Channel Probe has proved to be a very effective tool for measuring signal distortions in the range (delay time) and Doppler domains under conditions of severe ionospheric disturbance. Experiments that have been conducted in the polar cap have demonstrated that Channel Probe measurements also characterize the ionospheric environment in ways that are potentially quite valuable in the study of geophysical plasma dynamics. Preliminary comparison of observations and predictions based on scattering theory show promise for the eventual development of a robust theory that can be applied to HF propagation over any desired range of disturbances in the ionosphere.

The research program described in this report will be continued for two years under the support of another DNA contract. A third polar campaign is planned for the summer of 1985. The receiver site will then be moved to Maine, and a winter and spring campaign will be conducted to study signal distortions for propagation over the auroral path from Greenland to Maine. Both the transmitter and receiver sites will then be moved to the South Pacific, and an equatorial campaign will be carried out in the summer of 1986.

SECTION 9

LIST OF REFERENCES

- Aarons, J., J. P. Mullen, and H. E. Whitney, "The Scintillation Boundary," J. Geophys. Res., Vol. 74, pp. 884-889, (1969).
- Aarons, J., and R. S. Allen, "Scintillation Boundary during Quiet and Disturbed Magnetic Conditions," J. Geophys. Res., Vol. 76, No. 1, pp. 170-177, (January 1971).
- Aarons, J., and R. S. Allen, "Scintillation Boundary during Quiet and Disturbed Magnetic Conditions," J. Geophys. Res., Vol. 78, pp. 7441-7451, (1973).
- Barry, G. H., L. J. Griffiths, and J. C. Taenzer, "HF Radio Measurements of High-Altitude Acoustic Waves from a Ground-Level Explosion," J. Geophys. Res., Vol. 71, pp. 1473-1482, (1966).
- Basler, R. P. and R. N. De Witt, "The Height of Ionospheric Irregularities in the Auroral Zone," J. Geophys. Res., Vol. 67, No. 2, pp. 587-593, (February 1962).
- Basler, R. P. and T. D. Scott, "Ionospheric Structure from Oblique-Backscatter Sounding," Radio Sci., Vol. 8, pp. 425-429, (May 1973).
- Basler, R. P., T. D. Scott, and R. L. DuPuy, "Irregularity Motions in the Polar Ionosphere," Radio Sci., Vol. 8, pp. 745-751, (August-September 1973).
- Basu, S., "Universal Time Seasonal Variations of Auroral Zone Magnetic Activity and VHF Scintillation," J. Geophys. Res., Vol. 80, pp. 4725-4732, (1975).
- Basu, S., E. MacKenzie, S. Basu, H. C. Carlson, D. A. Hardy, F. J. Rich, and R. C. Livingston, "Coordinated Measurements of Low-Energy Electron Precipitation and Scintillations/TEC in the Auroral Oval," Radio Sci., Vol. 18, No. 6, pp. 1151-1165, (November-December 1983).

- Buchau, J., J. Aarons, J. P. Mullen, E. J. Weber, J. A. Whalen, H. E. Whitney, and E. E. Crampton, Jr., "Amplitude Scintillation Studies in the Polar Region on 250 MHz," Effect of the Ionosphere on Space and Terrestrial Systems, Ionosphere Effects Symposium, Crystal City, Arlington, VA (January 1978).
- de la Beaujardière, O., V. B. Wickwar, G. Caudal, J. M. Holt, J. D. Craven, L. A. Frank, L. H. Brace, D. S. Evans, J. D. Winningham, and R. A. Heelis, "Universal Time Dependence of Nighttime F Region Densities at High Latitudes," J. Geophys. Res., Vol. 90, No. A5, pp. 4319-4332, (May 1985).
- Croft, T. A. and H. Hoogasian, "Exact Ray Calculations in a Quasi-Parabolic Ionosphere with No Magnetic Field," Radio Sci., Vol. 3, pp. 69-79, (January 1968).
- Dyson, P. L., and J. D. Winningham, "Top Side Ionospheric Spread F and Particle Precipitation in the Day Side Magnetospheric Clefts," J. Geophys. Res., Vol. 79, No. 34, pp. 5219-5230, (December 1974).
- Esswein, R. and S. M. Flatté, "Calculation of the Phase-Structure Function Density from Oceanic Internal Waves," J. Acoust. Soc. Am., Vol. No. 5, pp. 1387-1396, (1981).
- Flatté, S. M., R. Dashen, W. H. Munk, K. M. Watson, and F. Zachariasen, Sound Transmission Through a Fluctuating Ocean, (Cambridge University Press, Cambridge, MA, 1979).
- Foster, J. C. and J. R. Doupnik, "Plasma Convection in the Vicinity of the Dayside Cleft," J. Geophys. Res., Vol 89, No. A10, pp. 9107-9113, (October 1984).
- Fremouw, E. J., C. L. Rino, R. C. Livingston, and M. C. Cousins, "A Persistent Subauroral Scintillation Enhancement Observed In Alaska," Geophys. Res. Let., Vol. 4, No. 11, pp. 539-542, (November 1977).
- Fremouw, E. J., J. F. Vickrey, D. A. Hardy, R. E. Huffman, F. J. Rich, C. I. Meng, K. A. Potocki, T. A. Potemra, W. B. Hanson, R. A. Heelis, and L. A. Witwer, "The HILAT Program," EOS, Vol. 64, pp. 163-170, (May 1983).
- Georges, T. M., "Short-Period Ionospheric Oscillations Associated with Severe Weather," Proc. Symp. Acoustic-Gravity Waves in the Atmosphere, Boulder, CO (July 1968).

- Hunsucker, R. D. and H. F. Bates, "Survey of Polar and Auroral Region Effects on HF Propagation," Radio Science, Vol. 4, No. 4, pp. 347-365, (April 1969).
- Kelley, M. C., J. F. Vickrey, C. W. Carlson, and R. Torbert, "On the Origin and Spatial Extent of High-Latitude F Region Irregularities," J. Geophys. Res., Vol. 87, No. A6, pp. 4469-4475, (June 1982).
- Livingston, R. C., C. L. Rino, J. Owen, and R. T. Tsunoda, "The Anisotropy of High-Latitude Nighttime F-Region Irregularities," J. Geophys. Res., Vol. 87, No. A12, pp. 10,519-10,526, (December 1982).
- Marcos, F. A., "Aircraft-Induced Ionospheric Disturbances," Air Force Cambridge Research Laboratories, AFCRL-66-229, (April 1966).
- Moshupi, M. C., C. D. Anger, J. S. Murphree, D. D. Wallis, J. H. Whitteker, and L. H. Brace, "Characteristics of Trough Region Auroral Patches and Detached Arcs Observed by ISIS 2," J. Geophys. Res., Vol. 84, No. A4, pp. 1333-1346, (April 1979).
- Ossakow, S. L. and P. K. Chaturvedi, "Current Convective Instability in the Diffuse Aurora," Geophys. Res. Lett., Vol. 6, pp. 332-339, (1979).
- Ossakow, S. L., "Reviews of Geophysics and Space Physics Ionospheric Irregularities," JGR, Vol. 17, No. 4, pp. 2691-2698, (June 1979).
- Pike, C. P., "A Latitudinal Survey of the Daytime Polar F Layer," J. Geophys. Res., Vol. 76, No. 31, pp. 7745-7753, (November 1971).
- Price, G. H., "Striation Effect on HF Signals," Final Technical Report, Contract DNA-001-83-C-0413, SRI Project 6381, SRI International, Menlo Park, CA (in review, June 1985).
- Reilly, M. H., "Ionospheric True Height Profiles from Oblique Ionograms," Radio Science, Vol. 20, No. 3, pp. 280-286, (May-June 1985).
- Rino, C. L., R. C. Livingston, and S. J. Matthews, "Evidence for Sheetlike Auroral Ionospheric Irregularities," Geophys. Res. Lett., Vol. 5, pp. 1039-1047, (1978).
- Rino, C. L., "A Power Law Phase Model for Ionospheric Scintillation. 2. Strong Scatter," Radio Sci., Vol. No. 6, pp. 1147-1155, (1979).
- Rino, C. L., and S. J. Matthews, "On the Morphology of Auroral Zone Radio Wave Scintillation," J. Geophys. Res., Vol. 85, No. A8, pp. 4139-4151, (August 1980).

- Rino, C. L., "On the Application of Phase Screen Models to the Interpretation of Ionospheric Scintillation Data," Radio Sci., Vol. 17, No. 4, pp. 855-867, (July-August 1982).
- Robinson, R. M., D. S. Evans, T. A. Potemra, and J. D. Kelly, "Radar and Satellite Measurements of an F-Region Ionization Enhancement in the Post-Noon Sector," Geophys. Res. Letts., Volume 11, No. 9, pp. 2734-2741, (September 1984).
- Robinson, R. M., R. T. Tsunoda, and C. I. Meng, "A Source of F-Region Ionization Enhancements at the Equatorward Edge of the Auroral Oval," J. Geophys. Res., (submitted 1985).
- Secan, J. A. and E. J. Fremouw, "Improvement of the Scintillation-Irregularity Model in WBMOD," Final Report, Contract No. DNA 001-81-C-0092, prepared for Defense Nuclear Agency, Washington, DC (February 1983).
- Shepherd, R. A. and J. B. Lomax, "Frequency Spread in Ionospheric Radio Propagation," IEEE Transactions on Communication Technology, Vol. Com-15, No. 2, pp. 268-275, (April 1967).
- Snyder, A. L., S. I. Akasofu, and C. P. Pike, "The Day-Sector Polar F-Layer during a Magnetospheric Substorm," Planet. Space Sci., Vol. 21, pp. 399-407, (1973).
- Thomas, J. O., "The Distribution of Electrons in the Ionosphere," Proc. IRE, Vol. 47, pp. 162, (1959).
- Titheridge, J. E., "The Overlapping-Polynomial Analysis of Ionograms," Radio Sci., Vol. 2, pp. 1169-1175, (October 1967).
- Tsunoda, R. T., R. M. Robinson, and C. Senior, "Two Possible Sources of Plasma-Density Enhancements in the Auroral F Layer," J. Geophys. Res., (submitted 1985).
- Vickrey, J. F., C. L. Rino, and T. A. Potemra, "Chatanika/Triad Observations of Unstable Ionization Enhancements in the Auroral F-Region," Geophys. Res. Lett., Vol. 7, No. 10, pp. 789-792, (October 1980).
- Vickrey, J. F., and M. C. Kelley, "Irregularities and Instabilities in the Auroral F Region," in High-Latitude Space Plasma Physics (Plenum Press, New York, NY 1982).
- Weber, E. J., J. Buchau, R. H. Eather, and S. B. Mende, "Northsouth Aligned Equatorial Airglow Depletions," J. Geophys. Res., Vol. 83, pp. 712-719, (1978).

Weber, E. J., J. Buchau, J. G. Moore, J. R. Sharber, R. C. Livingston, J. D. Winningham, and B. W. Reinisch, "F Layer Ionization Patches in the Polar Cap," J. Geophys. Res., Vol. 89, No. A3, pp. 1683-1694, (March 1984).

Wittwer, L. A., "Radio Wave Propagation in Structured Ionization for Satellite Applications," DNA 5304D, Defense Nuclear Agency, Washington, DC (1979).

Wittwer, L. A., "A Trans-Ionospheric Signal Specification for Satellite C Applications," DNA In-House Report DNA 5662D, Atmospheric Effects Division, Defense Nuclear Agency, Washington, DC (December 1980).

Wittwer, L. A., "Radio Wave Propagation in Structured Ionization for Satellite Applications II," DNA-IR-82-02, Defense Nuclear Agency, Washington, DC (1982).

Wolcott, J. H., D. J. Simons, D. D. Lee, and R. A. Nelson, "Observations of an Ionospheric Perturbation Arising from the Coalinga Earthquake on May 2, 1983," J. Geophys. Res., Vol. 89, pp. 6835-6839, (1984).

DISTRIBUTION LIST

DEPARTMENT OF DEFENSE

ASST TO THE SECY OF DEFENSE ATOMIC ENERGY
ATTN: EXECUTIVE ASSISTANT

BOSTON COLLEGE, THE TRUSTEES OF
2 CYS ATTN: CHAIRMAN DEPT OF CHEMISTRY
2 CYS ATTN: CHAIRMAN DEPT OF PHYSICS

DEFENSE INTELLIGENCE AGENCY
ATTN: RTS-2B

DEFENSE NUCLEAR AGENCY
ATTN: RAAE K SCHWARTZ
ATTN: RAAE P CROWLEY
ATTN: RAAE P LUNN
4 CYS ATTN: STTI-CA

DEFENSE TECHNICAL INFORMATION CENTER
12 CYS ATTN: DD

FIELD COMMAND DNA DET 2
LAWRENCE LIVERMORE NATIONAL LAB
ATTN: FC-1

FIELD COMMAND DEFENSE NUCLEAR AGENCY
ATTN: FCTT
ATTN: FCTT W SUMMA

JOINT STRAT TGT PLANNING STAFF
ATTN: JLKS

UNDER SECY OF DEF FOR RSCH & ENGRG
ATTN: DEFENSIVE SYSTEMS
ATTN: STRAT & SPACE SYS (OS)
ATTN: STRAT & THEATER NUC FOR F VAJDA

DEPARTMENT OF THE ARMY

HARRY DIAMOND LABORATORIES
2 CYS ATTN: SCHLD-NW-P

U S ARMY ATMOSPHERIC SCIENCES LAB
3 CYS ATTN: SLCAS-AE-E

U S ARMY BALLISTIC RESEARCH LAB
ATTN: SLCBR-SS-T TECH LIB

U S ARMY FOREIGN SCIENCE & TECH CTR
ATTN: DRXST-SD

U S ARMY NUCLEAR & CHEMICAL AGENCY
ATTN: LIBRARY

U S ARMY RESEARCH OFFICE
ATTN: R MACE

U S ARMY STRATEGIC DEFENSE COMMAND
ATTN: ATC-O W DAVIES

USA ELECT WARFARE/SEC,SURV & TARGET ACQ CTR
ATTN: AMSEL-EW-SS S KRONENBERG

DEPARTMENT OF THE NAVY

NAVAL POSTGRADUATE SCHOOL
ATTN: CODE 1424 LIBRARY

NAVAL RESEARCH LABORATORY
ATTN: CODE 2000 J BROWN
ATTN: CODE 2627 TECH LIB
ATTN: CODE 4128.2 J JOHNSON
ATTN: CODE 4139 D MCNUTT
ATTN: CODE 4700 W ALI
ATTN: CODE 4700 S OSSAKOW
ATTN: CODE 4720 J DAVIS
ATTN: CODE 4780 D STROBEL

NAVAL SURFACE WEAPONS CENTER
ATTN: CODE X211 TECH LIB

NAVAL WEAPONS SUPPORT CENTER
ATTN: CODE 6054 T ELLIS

SPACE & NAVAL WARFARE SYSTEMS CMD
ATTN: PD 50TD

DEPARTMENT OF THE AIR FORCE

AIR FORCE GEOPHYSICS LABORATORY
4 CYS ATTN: CA A STAIR
2 CYS ATTN: LID W SWIDER
2 CYS ATTN: LIU R HUFFMAN
2 CYS ATTN: LS R MURPHY
2 CYS ATTN: LSI R SHARMA
2 CYS ATTN: LSP D PAULSON
ATTN: LSP D SMITH
2 CYS ATTN: LSP R NADILE
2 CYS ATTN: LYD K CHAMPION

AIR FORCE OFFICE OF SCIENTIFIC RSCH
ATTN: AFOSR/NC
ATTN: ASOSR/NP MAJ JOHN PRINCE

AIR FORCE WEAPONS LABORATORY, AFSC
ATTN: SUL

PREVIOUS PAGE
IS BLANK

DEPARTMENT OF THE AIR FORCE (CONTINUED)

AIR FORCE SYSTEMS COMMAND

ATTN: DLAE
ATTN: DLTW
ATTN: DLXP
ATTN: SDR

AIR UNIVERSITY LIBRARY

ATTN: AUL-LSE

DEPUTY CHIEF OF STAFF/AFRDS

3 CYS ATTN: AFRDS SPACE SYS & C3 DIR

ROME AIR DEVELOPMENT CENTER, AFSC

ATTN: OCD J SIMONS

STRATEGIC AIR COMMAND/INCR

ATTN: INCR

STRATEGIC AIR COMMAND/NRI-STINFO

ATTN: NRI/STINFO

DEPARTMENT OF ENERGY

DEPARTMENT OF ENERGY

ATTN: OMA DP-22

UNIVERSITY OF CALIFORNIA

LAWRENCE LIVERMORE NATIONAL LAB

ATTN: L-10 A GROSSMAN
ATTN: L-262 D WUEBBLES
ATTN: L-325 G HAUGAN
ATTN: L-48 E WOODWARD
ATTN: L-71 J CHANG
ATTN: L-84 H KRUGER

LOS ALAMOS NATIONAL LABORATORY

ATTN: D SAPPENFIELD
ATTN: G M SMITH
ATTN: M PONGRATZ
ATTN: M SANDFORD
ATTN: P364 REPORT LIBRARY
ATTN: R JEFFRIES
ATTN: REPORT LIBRARY
ATTN: T BIENIEWSKI

SANDIA NATIONAL LABORATORIES

ATTN: L ANDERSON
ATTN: M KRAMM
ATTN: ORG 314 W D BROWN
ATTN: TECH LIB 3141 RPTS RECVG CLRK

OTHER GOVERNMENT

CENTRAL INTELLIGENCE AGENCY

ATTN: OSWR/NED

DEPARTMENT OF COMMERCE

ATTN: SEC OFC FOR J DEVOE

ATTN: SEC OFC FOR M KRAUSS

ATTN: SEC OFC FOR R LEVINE

ATTN: SEC OFC FOR S ABRAMOWITZ

NATIONAL OCEANIC & ATMOSPHERIC ADMIN

3 CYS ATTN: E FERGUSON

3 CYS ATTN: F FEHSENFELD

U S DEPARTMENT OF COMMERCE

ATTN: G FALCON

ATTN: W UTLAUT

DEPARTMENT OF DEFENSE CONTRACTORS

AERODYNE RESEARCH, INC

ATTN: C KOLB
ATTN: J WORMHOUDT
ATTN: M CAMAC
ATTN: M ZAHNISER

COMPUTER SCIENCES CORP

ATTN: F EISENBARTH

CONCORD SCIENCES CORP

ATTN: E SUTTON

CORNELL UNIVERSITY

ATTN: M KELLY

EOS TECHNOLOGIES, INC

ATTN: B GABBARD

GENERAL ELECTRIC CO

ATTN: R EDSALL

GEO CENTERS, INC

ATTN: E MARRAM

KAMAN SCIENCES CORP

ATTN: E CONRAD

KAMAN TEMPO

ATTN: B GAMBILL

5 CYS ATTN: DASIAC

KAMAN TEMPO

ATTN: DASIAC

MISSION RESEARCH CORP

ATTN: D ARCHER
ATTN: D SOWLE
ATTN: F GUIGLIANO
ATTN: M SCHEIBE
ATTN: R HENDRICK
ATTN: R KILB
2 CYS ATTN: TECH LIBRARY

PACIFIC-SIERRA RESEARCH CORP

ATTN: H BRODE, CHAIRMAN SAGE

DEPT OF DEFENSE CONTRACTORS (CONTINUED)

R & D ASSOCIATES

ATTN: F GILMORE
ATTN: H ORY
ATTN: R TURCO

RAND CORP

ATTN: C CRAIN
ATTN: P DAVIS

SCIENCE APPLICATIONS INTL CORP

ATTN: R LEADABRAND

SCIENCE APPLICATIONS INTL CORP

ATTN: E HYMAN

SRI INTERNATIONAL

2 CYS ATTN: C RINO
ATTN: D MCDANIEL
2 CYS ATTN: D RUST
2 CYS ATTN: G PRICE
2 CYS ATTN: P BENTLEY
2 CYS ATTN: R BASLER
ATTN: W CHESNUT

END

12-86

DTIC